University of Twente

CEM MSc Thesis Report

Aggregate roughness modelling

.

An idealized model study into the effects of patchy vegetation on mean river flow

Author:
Joost Noordermeer

Supervisors:
Dr. Ir. J.S. Ribberink
Dr. Ir. P.C. Roos
Dr. F. Huthoff
Dr. R.M.J. Schielen

October 12, 2012

Aggregated roughness modelling

An idealized model study into the effects of patchy vegetation on mean river flow

Student	:	Joost Noordermeer
Institute	:	University of Twente
Advisors	:	Dr. Ir. J.S. Ribberink
		Dr. Ir. P.C. Roos
		Dr. F. Huthoff
		Dr. R.M.J. Schielen
Date	:	October 12, 2012
Typeset	:	LaTeX

Summary

Rivers have been a lifeline for civilization throughout human history. It is therefore not surprising that so many cities and villages can be found around these locations. Dikes have been used in the past to protect these cities from floodrisk, however the combination of climate change and land subsidence have created a technological lock-in; dikes can no longer be heightened but it is also impossible to migrate entire cities. As a result the Room for the River policy plan was developed in the Netherlands which aims to increase protection against floods by allowing rivers to reclaim their natural course.

A direct result of this is that floodplains will see more frequent inundations as they will be used to temporarily store and transport water. Since floodplains are not inundated at all times, plants and trees can grow, which will alter the transportation capacity of these floodplains because these forms of vegetation induce resistance to the flow. Hydraulic model computations are used to assess the impact of hydraulic measures and use the resistance to flow as an input parameter. These calculations are typically performed for large spatial scales due to computational limitations, which therefore requires an aggregated roughness value for the entire region as small scale processes are not accounted for. There is however little known about the aspects of floodplains and vegetation that influence this aggregated roughness parameter. Several methods, based on fitting WAQUA simulation results, have been developed for this purpose.

A new method, based on an analytical rather than a numerical approach, was developed to investigate how spatial scales and various system parameters affect aggregate roughness as induced by vegetation patches. It is based on steady nonlinear depth-averaged shallow water equations while closing turbulence using a spatially constant horizontal eddy viscosity and allowing spatial variations in bed resistance. A weakly non-linear analysis was performed where small changes in resistance and the corresponding response in the flow were approximated up to the second order in a small parameter quantifying these variations. At second order, a spatially invariant contribution to the downstream flow velocity is obtained. This second order spatially invariant contribution is used to calculate the aggregate resistance over a floodplain. Model application is restricted to large spatial scales or small differences in roughness due to the solution method used.

The flow response to a variety of roughness patch characteristics was investigated and an increase in flow resistance was always found. Dominant mechanisms were identified in case of parallel roughness variations only (lateral shear), serial variations only (backwater effects) and combined variations (lateral shear, backwater effects and lateral redistribution of longitudinal momentum). Results show that larger spatial scales lead to a reduction in aggregate roughness. Ad-

ditionally, the influence of the eddy viscosity on model results is significant but it is difficult to recommend a certain input value as sources disagree. However, higher values of eddy viscosity lead to a greater energy loss to turbulent eddies, resulting in a greater aggregate resistance. Furthermore, it is found that near-diagonally oriented patches minimize the overall flow resistance.

The idealized approach allows a quick assessment of the influence of various system parameters on the mean river flow velocity as caused by spatially varying resistance. It also provides insight into the physical mechanisms that lead to a difference between the aggregate resistance and the average resistance of a river section. No explanation has been found yet regarding the unexpected influence of patch orientation on aggregate resistance and this will require further investigation.

Foreword

This thesis research is the final part of my masters, and my life as a student but also signifies a new beginning. The research discussed in this report describes how an idealized model was used to investigate the aggregated roughness of a river segment while allowing vegetation resistance to vary spatially.

The findings presented in this report would not have been possible without the tremendous help I received from my supervising committee. The long distance advice I received from Freek was useful in placing this research within its context. The feedback I received during the milestone meetings also helped me see the analysis from a different perspective. I would like to thank Jan and Ralph for their sincere interest in this research project. I would also like to thank Pieter whose enthusiasm is difficult to trump and who always found time for continued support during the entire research process.

Next I would like to thank the other residents of the WEM graduation room. Koen, Wouter, Gerben and Pedro livened up dull days at the office, while also discussing developments regarding each of our research projects.

Last but definately not least, I would like to thank my friends and family for their support during my entire education at the University of Twente.

Joost Noordermeer
Enschede, October 2012

Contents

1 Introduction **2**
- 1.1 Background . . . 2
- 1.2 Goal . . . 7
- 1.3 Research plan . . . 8
- 1.4 Outline . . . 9

2 Model **10**
- 2.1 Theoretical Background . . . 10
- 2.2 Model Formulation . . . 11
- 2.3 Scaling . . . 14
- 2.4 Typical Parameter Values . . . 15
- 2.5 Determining the spatially averaged resistance . . . 16

3 Weakly Non-Linear Analysis **18**
- 3.1 Linearization . . . 18
- 3.2 The first order solution . . . 19
- 3.3 Second order solution . . . 21
- 3.4 Summary . . . 25

4 Model applicability restrictions **26**
- 4.1 Perturbation model limitations . . . 27
- 4.2 Linearization limitations . . . 29
- 4.3 Range of applicability . . . 30
- 4.4 Summary . . . 31

5 Results: Simple roughness patch patterns **34**
- 5.1 Parallel roughness patches . . . 36
- 5.2 Serial roughness patches . . . 38
- 5.3 Checkerboard roughness patches . . . 42

6 Results: Complex patch patterns **46**
- 6.1 Obtaining roughness patch coefficients . . . 46
- 6.2 Input parameter values . . . 49
- 6.3 Influence of patch rotation . . . 49
- 6.4 Random roughness patches . . . 53
- 6.5 Summary . . . 55

7 Discussion **58**
7.1 Regarding the model 58
7.2 Regarding the patch characteristics analysis 59
7.3 Compared to current parameterizations 59

8 Conclusion **62**
8.1 Research questions 62
8.2 Recommendations 63

Bibliography **66**

A Notation **68**

B Hydrodynamic modelling approaches **70**

C Scaling operations **74**
C.1 Mass balance 74
C.2 Momentum balance 75

D Determining the linear problem **78**
D.1 Mass Balance 78
D.2 Momentum in the streamwise direction 79
D.3 Momentum in the transverse direction 81

E Fourier series representation **82**
E.1 Mass Balance 82
E.2 Momentum in the streamwise direction 83
E.3 Momentum in the transverse direction 83

F Matrix Inverse **86**
F.1 Matrix of Minors 86
F.2 Matrix of Cofactors 86
F.3 Determinant 87
F.4 The resulting inverse of the matrix 87

G Forcing in the second order **88**
G.1 Defining the second order problem 88
G.2 Eigenfunction projections of the second order forcing 89

H Spatial averaging contributing terms **92**

I Restrictive minimum value tables **96**

Chapter 1

Introduction

River management in the Netherlands has undergone rapid change in the past two decades. Where originally rivers were controlled and regulated using civil structures, current approaches emphasize the importance of providing a river with the necessary room for natural processes to occur. This paradigm shift was initiated by a combination of changing European Union environmental policy and the realization that Dutch water management was subjected to a technological lock-in (Wesselink, 2007).

The changes in river management have led to larger floodplain dimensions and more frequent inundations. Floodplains have become an integral part of a river's discharge capacity, leading to more research regarding the flow processes over these floodplains (Werner et al., 2005). Herein the modelling of hydraulic roughness, specifically as caused by vegetation rather than bedforms, is of key importance for changing water levels due to resistance (Forzieri et al., 2011). Recent research has shown that a parameter value change of 50% in roughness can lead to a 40% change in peak water level (Ballesteros et al., 2011).

This chapter will briefly introduce the current state of water management in conjunction with hydraulic roughness modelling, specifically oriented towards the Netherlands. From there the research aim is presented followed by the research questions. Finally the methodology is discussed briefly. Then an overview will be given of the contents of this report.

1.1 Background

In this section a brief background is provided concerning the causes of changing water management in the Netherlands, specifically surrounding floodplains, and the significance of this change concerning roughness modelling.

1.1.1 Water management practice in the Netherlands

Recent studies have shown that the water regulation measures taken in the past may not have sustainably prepared the Netherlands for the future (Makaske et al., 2011). The continued pumping of water for the creation of polders, and the construction of increasingly high levees has amplified the risks associated with a potential flooding event. Figure 1.1 shows how the history of

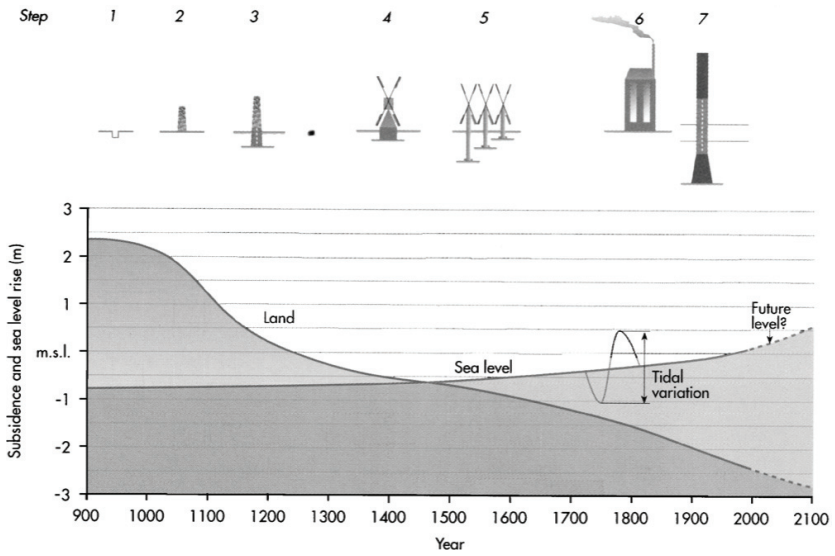

Figure 1.1: *Influence of water management throughout history in the Netherlands on land level compared to sea level rise.* Source: Huisman et al. (1998)

water management in the Netherlands has led to an increased risk due to the increasing difference between ground datum and mean sea level.

While the urban landscape subsides, peak water levels in the rivers potentially increase due to the effects of climate change. Additionally the continued urbanization of lower reaches of the Netherlands due to economical prospects in urban areas has led to zones where societal risk is extremely high[1]. There is a large gap between perceived safety and real safety in the Netherlands where water regulation is concerned (Wesselink, 2007).

This technological lock-in[2] is a vicious cycle that the Dutch government is trying to break as the height of levees cannot be increased indefinitely and the possible consequences of flooding in certain regions are becoming insurmountable. A paradigm shift occurred in the 1970s in the water management sector; water should not be controlled, but it should be accommodated (RWS, 2006). Two primary goals were set by the government that read as follows:

1. *"To bring flood protection for the riverine area to the required level;*

2. *To contribute to improving the spatial quality of the riverine area."*

- RWS (2006)

[1] Ichem (1985) defines societal risk as "*the relationship between frequency and the number of people suffering from a specified level of harm in a given population from the realization of specified hazards*"

[2] Urbanization, caused by good economic prospects, requires higher safety levels to reduce consequences of a potential disaster. This leads to a higher perception of safety causing more people to migrate to the urban areas. The current system is stuck in this cycle, also termed a technological lock-in (Wesselink, 2007)

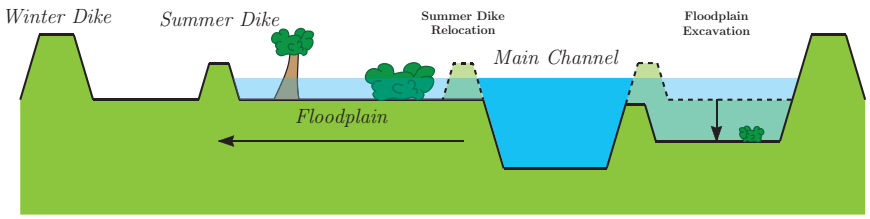

Figure 1.2: *Simplified cross section of a river illustrating the main channel, floodplain with vegetation and summer- & winter dikes. Additionally the two most frequently applied measures from the Room for the River project are illustrated: (i)Floodplain excavation and (ii) summer dike relocation.*

Improving spatial quality is described by RWS (2006) as the enhancement of economical, ecological and scenic values of the riverine area, which leads to the emphasis on the protection of nature values and other spatial functions. In combination with the flood protection measures this has led to various (at the time) unconventional measures such as the excavation of floodplains and the relocation of summer dikes (RVR, 2010); these measures are illustrated in Figure 1.2. Specifically the natural characteristics of river branches are to be preserved.

The main reasons for this approach are the previously mentioned technological lock-in complemented by the European Union Natura 2000 directive. Herein an underlying European network of nature is described (EU, 2010). The vast coverage of the river system in the Netherlands makes floodplains an ideal choice for this nature network. Therefore this leads to the restoration of natural functions of floodplains and river branches. By extending the width of the floodplains and by removing the summer dikes, a more natural water system is allowed to develop.

1.1.2 Floodplains

Floodplains are the strip of land bordering the main channel of a river that usually undergoes inundation during high discharges. They are formed and altered through sediment transport overland by water during high water levels, which then settles when the discharge lowers to a state where flow only occurs through the main channel (Bridge, 2003). This dynamic environment defines a special ecological regime wherein a large biodiversity can exist, which is precisely what the EU Natura 2000 plans aim to stimulate.

Floodplains house a large variety of plant and animal species, but also humans and man-made artefacts can be discovered throughout. The functions of floodplains are numerous, but lately an emphasis is placed on the natural functions of floodplains. These are the discharge of water and development of nature. This is made possible by increased recreational functionality of floodplains. These policy plans are outlined in the Room for the River policy document (RWS, 2006).

The characteristics of floodplains have been captured extensively using aerial photography in order to allow the continued investigation of biological functions of floodplains (RWS, 2007). Figure 1.3 shows how these photographs are trans-

(a) (b)

Figure 1.3: *Illustration of the conversion of* (a) *aerial imagery to* (b) *ecotope maps. This specific case is taken from the maps concerning the eastern tributaries of the Rhine in the Netherlands.* Source: RWS (2007)

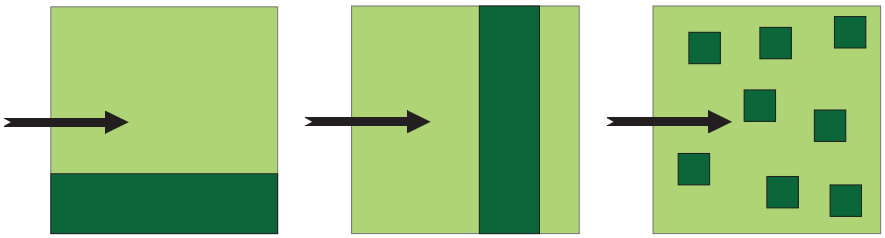

(a) (b) (c)

Figure 1.4: *The three types of vegetation as modelled in WAQUA by van Velzen and Klaassen (1999):* (a) *vegetation parallel to the flow,* (b) *vegetation perpendicular to the flow (serial) and* (c) *randomly placed vegetation in the area.*

formed to land-use characteristics. This practice has the added benefit that the land-use values can be used to investigate the discharge capacity of a river as land-use can be an important indicator to determine the resistance to flow. Many different coverings coincide with different intensities of hydraulic roughness which may reduce or increase the floodplain discharge capacity.

1.1.3 Modelling vegetation resistance

Hydraulic models are used in the Netherlands to evaluate and design measures that are aimed at increasing safety against flooding. Vegetation resistance is a very important parameter in hydraulic modelling, although not much is understood about how vegetation resistance should be incorporated. Two methods of vegetation resistance calculations are briefly discussed here.

Aggregate values of roughness combinations

The method currently used by the Dutch Ministry of Infrastructure and the Environment to determine aggregate roughness values of areas with roughness combinations is based on the study by van Velzen and Klaassen (1999). The roughness values are represented in terms of a Chézy value, C, with dimensions $\mathrm{m}^{1/2}\ \mathrm{s}^{-1}$. It was found analytically that the roughness values of completely serial, parallel and randomly placed vegetation can be determined by:

$$C_{\text{parallel}} = \sum_i x_i C_{ri}, \qquad C_{\text{serial}} = \frac{1}{\sqrt{\sum_i \frac{x_i}{C_{ri}^2}}}, \qquad C_{\text{rand}} = \frac{1}{\sqrt{\frac{c_D A_r h x_i}{2g} + \frac{1}{C_b^2}}},$$

where C_{parallel} is the aggregate roughness of patterns parallel to the flow, x_i shows a coverage fraction of vegetation type i, C_{ri} is the aggregate roughness of vegetation type i, C_{serial} is the roughness of serially placed vegetation and C_{rand} is the aggregate roughness of randomly placed vegetation. WAQUA simulations were used to determine the effect of combinations of serial, parallel and randomly placed vegetation patches (Figure 1.4). A weighted average model that combines the formulas of serial and parallel vegetation patterns was found and calibrated for general use. The total hydraulic roughness in terms of Chézy can then be defined as:

$$C_{rc} = \phi C_{\text{serial}} - (1-\phi) C_{\text{parallel}},$$

where C_{rc} is the aggregated Chézy value for combined patterns and ϕ is a weighing parameter ($0 < \phi < 1$). It was found that a weighing parameter value $\phi = 0.6$ gave the most accurate WAQUA results in general (van Velzen et al., 2003b), and therefore this value is the norm.

Extension by ter Haar (2010)

Ter Haar (2010) extended the method of van Velzen and Klaassen (1999) to account for various shortcomings of the weighted average method. The model did not account for the influence of flow depth, and also only a limited number of vegetation patterns were modelled. The influence of patterns was subsequently also over- or underestimated, most likely due to the fixed weighing parameter ϕ. The study of ter Haar (2010) has lead to a new aggregate roughness equation, which was found by fitting model results obtained from WAQUA. The resistance formulation as found by ter Haar (2010) is given by:

$$C_r = C_{\text{smooth}} - x_{\text{rough}} C_{\text{smooth}} \left[1+\gamma\right] + x_{\text{rough}} C_{\text{rough}} \left[1-\gamma\right],$$

where C_{smooth} and C_{rough} are the Chézy values of the smooth and rough zones respectively, x_{rough} is the fraction of the area covered by rough vegetation, and where γ is given by:

$$\gamma = 0.19 \frac{\delta \cdot N_\delta}{\overline{W_p} \cdot N_p} + 1.31 \frac{\lambda_{\text{adap}} \cdot \min\left(1, \frac{\overline{L_f}}{\lambda_{\text{adap}}}\right)}{L_p},$$

where δ is the width of a mixing layer, N_δ is the total number of mixing layers, $\overline{W_p}$ is average width of the vegetation patches, N_p is the total number of patches, λ_{adap} is the adaptation length of the flow, $\overline{L_f}$ is the average free length behind the patches and L_p is the length of a patch.

The model by ter Haar (2010) was applied to many more patch situations in WAQUA than the weighted average method as proposed by van Velzen et al. (2003b). It was found that the new model predicted the roughness of the patterns as simulate in WAQUA better than the model currently used to determine aggregate resistance that is based on the original study by van Velzen and Klaassen (1999).

1.1.4 Limitations

The two methods described have both used WAQUA as a basis for the aggregate roughness parameterization. Numerical calculations were performed and the results were fitted to obtain the most reliable and accurate roughness parameterization. Model calculations show mixing layers and flow adaptation, but these processes are not isolated easily. It is thus difficult to distinguish which flow processes affect what type of patch most. Furthermore, due to the fact that WAQUA is a grid based numerical model several limitations arise. The shape and layout of roughness patches are dictated by this model property.

An idealized model, based on the same flow equations that WAQUA uses, may provide additional insight concerning the flow processes and how these affect aggregate roughness. Idealized models generally require extremely simplified spatial geometries, but this will not differ from the numerical approaches previously discussed. Furthermore, a more flexible roughness pattern description can be used to investigate more complex patch shapes and properties (i.e. orientation). An additional benefit is the fact that calculation time is generally much faster for analytical solutions.

A fully analytical solution may not be obtainable due to the complexity of the nonlinearities in the flow equations. It is therefore suggested to attempt a weakly nonlinear analysis where the dynamics of the flow in response to a roughness disturbance are approximated using an expansion series. Although the solution will always be an approximation, it may be suggested that higher orders of the solution are negligible. This approach may provide additional insight into the dynamics leading to different aggregate roughnesses while allowing a greater freedom in describing roughness patch configurations.

1.2 Goal

The aim of this research is to improve aggregate roughness parameterization through investigating how physical processes around roughness patches are influenced by different vegetative roughness patch characteristics. An idealized model will be used that allows quick assessment of flow disturbance and aggregate roughness as caused by different patch characteristics. In order to achieve this goal the following central question needs to be answered:

What characteristics of roughness patches influence what flow processes as caused by spatially varying roughness in a river section?

The following questions serve to answer this research question:

1. How can aggregated roughness for a floodplain section be determined using an idealized model?
   (a) What flow equations should be used to determine the flow over floodplains with spatially varying roughness?
   (b) How can spatially varying roughness be incorporated in an idealized model?
   (c) How does the idealized model lead to a single aggregated roughness value for an entire floodplain section?
2. What is the influence of various patch characteristics on the mean flow over the floodplain section?
   (a) What characteristics can be attributed to vegetation patches?
   (b) What characteristics of vegetation patches have the largest influence on aggregate roughness?
3. How can the new insights regarding the characteristics of vegetation patches be incorporated into an aggregated roughness parameterization method?

1.3 Research plan

In order to accomplish the above goal and to answer the questions stated, the following research plan is followed:

- An idealized steady non-linear depth-averaged hydrodynamic model is formulated, which allows for the spatial variation in roughness. The equations of flow are scaled so that different processes can be compared on a similar general scale.
- A weakly non-linear steady state depth-averaged flow model is developed that allows for spatial variation in roughness. It will be assumed that spatial roughness variations are a small perturbation of a spatially uniform background roughness. An analytical solution of the flow response is found up to the second order in the small parameter that quantifies the roughness variations. The main goal of this model is to investigate the spatially averaged, or aggregated resistance for a river section as caused by smaller scale roughness variations. A flat river bed is considered where roughness may vary spatially.
- The limits of the models applicability is investigated. The weakly non-linear analysis imposes limitations on model applicability. The limitations of the size of the perturbation is found in this analysis.
- Next the influence of the model input variables is analysed. The relative importance of input parameters is investigated to find what influences aggregated roughness the most utilizing this approach. Simple patch descriptions are used to keep the analysis transparent.

- The influence of patch orientation on the flow retardation is investigated using more complex patches. A Fast Fourier Transform algorithm is used to extract the patch description from an input image, for which the aggregate roughness is then determined.

1.4 Outline

In chapter 2 the foundation of the model and the solution technique is outlined. The spatial geometry of the system analysed is explained and the flow equations relevant to this investigation are scaled. Chapter 3 describes the solution method used and provides an equation that can be used to calculate the aggregated flow retardation as caused by the spatially varying roughness. Chapter 4 describes the possible input variables used in the analysis and investigates the limitations of the weakly non-linear flow model derived. In chapter 5, simple patch descriptions are used to analyse the influence of the input variables on the aggregated flow velocity. More complex patches are then discussed in chapter 6. After this the discussion and conclusions are presented in chapters 7 and 8 respectively.

Chapter 2

Model

In this chapter the formulation of the model is described. The theoretical basis for the model is briefly outlined, thereafter some assumptions are stated that allow the application of the flow equations on the problem as described in the previous chapter. Once the model equations have been formulated a scaling operation is performed, which enables the identification of the more important processes.

2.1 Theoretical Background

Modelling river flow is generally done using some adaptation of the Navier-Stokes equations. These equations describe the conservation of mass and the conservation of momentum in a viscous fluid. The mass balance or continuity equation for water can be given by (Fox et al., 2004):

$$\nabla^* \cdot \vec{u}^* = 0, \tag{2.1}$$

where ∇^* is the nabla operator used to determine the gradient of a quantity in all three directions $(\frac{\partial}{\partial x^*}, \frac{\partial}{\partial y^*}, \frac{\partial}{\partial z^*})$ and $\vec{u}^*$ is the velocity vector in three directions (u^*, v^*, w^*) in the x^*, y^* and z^* directions respectively in m s^{-1}. Please note that the * denotes that a value is dimensional.

The Navier-Stokes equations for incompressible flow of Newtonian fluids are given by (Acheson, 1990):

$$\overbrace{\rho^*\Big(\underbrace{\frac{\partial \vec{u}^*}{\partial t^*}}_{\text{Inertia}} + \underbrace{\vec{u}^* \cdot \nabla^* \vec{u}^*}_{\text{Advection}}\Big)}^{\text{Substantial Derivative}} = \overbrace{\underbrace{-\nabla^* p^*}_{\substack{\text{Pressure}\\ \text{gradient}}} + \underbrace{\mu^* \nabla^{*2} \vec{u}^*}_{\text{Viscosity}}}^{\text{Divergence of stress}} + \underbrace{\mathcal{N}^*}_{\substack{\text{Additional}\\ \text{forces}}}, \tag{2.2}$$

where ρ^* is the density of water in kg/m^3, t^* is time in s, p^* is the total pressure in the system, μ^* is the molecular viscosity and $\mathcal{N}^*$ is any additional forcing to the system.

Equation (2.2) can be adapted to model various forms of fluid flow. The required level of detail plays a crucial role in determining how this general function should be applied. Different hydraulic models are based on different

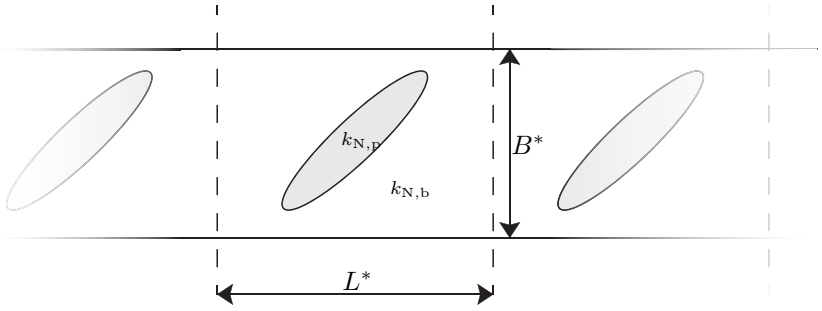

Figure 2.1: *Illustration of the geometry of the system considered for this analysis; a straight channel with constant slope i_0, width B^* and recurrent roughness patches after a certain length scale L^* with no slip boundaries at both banks. Additionally the Nikuradse roughness of the background vegetation is described by $k_{N,b}$ and the roughness of the patch is given as $k_{N,p}$*

assumptions. Especially the required level of detail of turbulence calculations is a primary decision when determining what method to apply. Full scale turbulence calculations are the most accurate, but have incredible computational costs whereas simplifications of the turbulent effects leads to faster but less accurate results. Appendix B gives an overview of different adaptations of the Navier-Stokes equations.

2.2 Model Formulation

In this section the model formulation is discussed. First the considered geometry is described and it is explained how this geometry may lead to an aggregate roughness calculation that accounts for spatially varying roughness patches. From there the flow equations are presented. The basis for this model was formulated by Roos (2011) in the research outline.

2.2.1 Geometry

The goal of this research is to determine an aggregated friction value for a river segment, which accounts for spatially varying roughness within that river segment. For this research a straight channel is considered with a constant width and energy slope. The patch patterns recur periodically in space but should provide the same aggregate value per segment, allowing the analysis of a single river segment.

Figure 2.1 shows the geometry of the system described where B^* is the width of the channel and L^* is the length of a singular patch pattern that repeats infinitely. Additionally the Nikuradse roughness of both the patch and the background vegetation are given as $k_{\mathrm{N,p}}$ and $k_{\mathrm{N,b}}$ respectively.

2.2.2 Equations of Flow

The Navier-Stokes equations (momentum) and the continuity equation are the starting points for the model formulation. Several assumptions are made in the formulation of this model. These are:

- Turbulence can be accounted for using a spatially constant horizontal eddy viscosity ν_{h}^* to close the turbulence problem as described in appendix B.
- Flow in the system is steady and non-linear.
- The vertical component of the flow velocity is much smaller than the horizontal components allowing for the simplification where depth-averaged flow is considered eliminating the vertical component of flow while significantly simplifying the analysis.

The steady-state momentum equations in a generalized form can then be written as (Acheson, 1990):

$$\vec{u}^* \cdot \nabla \vec{u}^* = -\frac{1}{\rho^*} \nabla p^* + \nu_{\mathrm{h}}^* \nabla^{*2} \vec{u}^* + \mathcal{N}^*, \tag{2.3}$$

where $\vec{u}^* = (u^*, v^*)$ is the depth averaged flow velocity in the downstream x^* and transverse y^* directions, ∇^* is the horizontal nabla operator $\nabla^* = (\partial/\partial x^*, \partial/\partial y^*)$, ρ^* is the density of water, p^* is the pressure in the system, ν_{h}^* is the spatially and temporally constant eddy viscosity and $\mathcal{N}^*$ is any additional forcing on the system. The pressure in the system consists of an energy slope and the pressure as caused hydrostatically by free surface elevations.

The only additional force acting on the system will be the spatially varying resistance, which is accounted for in $\mathcal{N}^*$, all other forms of resistance are ignored[1]. The friction at the bed is formulated as:

$$\mathcal{N}^* = -\frac{\tau_b^*}{\rho^* h^*},$$

where h^* is the water depth in meters and τ_b^* is the bed shear stress in $\mathrm{N/m^2}$. τ_b^* is defined using the quadratic bottom friction formulation, which defines shear stress as:

$$\tau_b^* = \rho g^* \frac{|\vec{u}^*| \vec{u}^*}{C^{*2}},$$

where g^* is the gravitation constant and C^* is the Chézy coefficient in $\mathrm{m^{1/2}\ s^{-1}}$. It is important to note here that this formulation of friction requires variations in flow to be gradual. The Chézy coefficient can be translated to a dimensionless drag coefficient through:

$$c_{\mathrm{D}} = \frac{g^*}{C^{*2}},$$

and thus friction is incorporated as:

$$\mathcal{N}^* = -c_{\mathrm{D}} \frac{|\vec{u}^*| \vec{u}^*}{h^*}.$$

[1]There are many other forms of friction that normally influence flow through a channel. Some examples of this are wind friction at the surface, bank friction, friction caused by the curvature of a river etc.

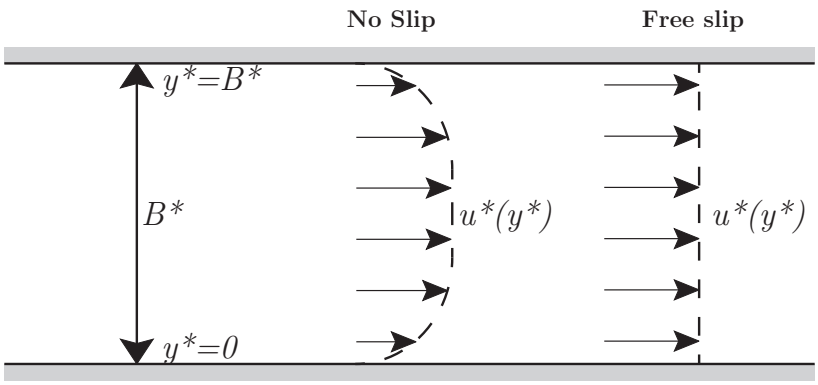

Figure 2.2: *Schematization of the difference between free slip and non free slip boundary conditions with regards to the flow velocity in the downstream direction. A transverse flow velocity profile u(y) is shown for both cases.*

A last step is to define the water depth as $h^* = H^* + \zeta^*$ where H^* is the mean water depth and ζ^* is the free surface elevation. The nonlinear depth-averaged shallow water equations are then formulated as:

$$(\vec{u}^* \cdot \nabla^*)\vec{u}^* + c_D \frac{|\vec{u}^*|\vec{u}^*}{H^* + \zeta^*} = -g^*(\nabla^* \zeta^* - i_0 \boldsymbol{e}_x) + \nu_{\mathrm{h}}^* \nabla^{*2} \vec{u}^*, \tag{2.4}$$

$$\nabla^* \cdot ([H^* + \zeta^*]\vec{u}^*) = 0, \tag{2.5}$$

where i_0 is the energy slope and $\boldsymbol{e}_x$ is the unit vector in the streamwise direction. Here equation (2.5) describes the conservation of mass and the following terms can be identified in the momentum equations:

$$\begin{aligned}
(\vec{u}^* \cdot \nabla^*)\vec{u}^* &= \text{ advection;} \\
c_D \frac{|\vec{u}^*|\vec{u}^*}{H^* + \zeta^*} &= \text{ the spatially varying bed resistance;} \\
-g^* \nabla^* \zeta^* &= \text{ the free surface elevation pressure gradient;} \\
g^* i_0 \boldsymbol{e}_x &= \text{ the energy slope;} \\
\nu_{\mathrm{h}}^* \nabla^{*2} \vec{u}^* &= \text{ the viscous effects including turbulence.}
\end{aligned}$$

It is important to note that c_{D} in this formulation is space dependent, i.e. $c_{\mathrm{D}} = c_{\mathrm{D}}(x^*, y^*)$. To complete the model formulation boundary conditions must be set.

Figure 2.2 shows a schematized difference between a free slip condition and a no slip condition. In the latter case the boundaries influence the flow velocity in the downstream direction, which leads to a lower average flow velocity. This resistance is not of interest in this analysis and therefore a free slip condition is imposed. By imposing free slip, boundary layers will be ignored that are the result of the system boundaries. Consequently only the the spatially varying bed roughness will affect the flow velocity, which is what is of interest in this research. The boundary conditions are formulated as:

$$v^* = \frac{\partial u^*}{\partial y^*} = 0 \qquad \text{at} \qquad y^* = 0 \text{ and } B^*. \tag{2.6}$$

These boundary conditions state that water cannot enter or exit through the river banks, nor can boundary layers form near the side-walls.

2.3 Scaling

Now that the model has been formulated a scaling operation will be performed to expose the relative importance of different flow processes in the system. Typical scales for this system are identified and substituted into the flow equations given by (2.4) and (2.5).

A typical length scale for the system can be identified in the geometric definition of the problem. The length of a single patch (pattern) before recurrence L^* is used to scale all distances in the problem. Secondly a velocity scale for the system can be determined by balancing the energy slope and the resistance in the undisturbed case (i.e. without roughness patches). This gives (analogous to equation (2.15)):

$$c_{\mathrm{D},0}\frac{U^{*2}}{H^*} = g^* i_0 \qquad \rightarrow \qquad U^* = \sqrt{\frac{g^* i_0 H^*}{c_{\mathrm{D},0}}}, \tag{2.7}$$

where U^* is the newly found velocity scale and $c_{\mathrm{D},0}$ is the drag coefficient of the undisturbed or mean vegetation. Finally an elevation scale can also be determined using this equation where:

$$Z^* = \frac{U^{*2}}{g^*} = \frac{i_0 H^*}{c_{\mathrm{D},0}}, \tag{2.8}$$

where Z^* is the elevation scale. These three scales are used to determine dimensionless quantities relevant to this analysis, which are given by:

$$\vec{x} = \frac{\vec{x}^*}{L^*}, \qquad \vec{u} = \frac{\vec{u}^*}{U^*}, \qquad \zeta = \frac{\zeta^*}{Z^*}. \tag{2.9}$$

These dimensionless quantities and the scales can be used to scale the problem. This leads to the following scaled equations of flow:

$$(\vec{u}\cdot\nabla)\,\vec{u} + \nabla\zeta - \nu\nabla^2\vec{u} = \mu_{\mathrm{b}}\boldsymbol{e}_x - \frac{\mu|\vec{u}|\vec{u}}{1+F^2\zeta}, \tag{2.10}$$

$$\nabla\cdot\left[\left(1+F^2\zeta\right)\vec{u}\right] = 0, \tag{2.11}$$

with the following dimensionless quantities:

$$F = \frac{U^*}{\sqrt{g^* H^*}}, \qquad \nu = \frac{\nu_{\mathrm{h}}^*}{U^* L^*}, \qquad \mu = \frac{c_{\mathrm{D}} L^*}{H^*}, \qquad \text{and} \qquad \mu_0 = \frac{c_{\mathrm{D},0} L^*}{H^*}. \tag{2.12}$$

The full derivation of these equations can be found in Appendix C. Note that the Froude number F becomes an important scale in both the momentum and the mass balance. Finally also the boundary conditions must be scaled, giving

$$v = \frac{\partial u}{\partial y} = 0 \qquad \text{at} \qquad y = 0, B$$

where $B = B^*/L^*$, which is the last dimensionless quantity found for the scaling of the system. Note that B refers to an aspect ratio of the river section analyzed.

2.4 Typical Parameter Values

In this section the input variables for the model are briefly discussed. Some reference values that will be used throughout the calculations are provided below.

Mean water depth H^*: The mean water depth in this model is of a significant influence on model output. It influences all model scales (equations (2.7), (2.9)), and thus influences all results greatly depending on the value chosen. For all calculations reasonable water levels over floodplains will be used ranging between 0.1 meters to a maximum of 7 meters, based on the results of ter Haar (2010). This range will not be applicable in all cases due to the nature of the analysis. In chapter 4 the limitations regarding the input values is discussed in more detail.

Patch pattern length L^*: The length scale of the vegetation patches influences the scales defined in equation (2.9) and also the width scale B. Due to the fact that this research aims to investigate small scale disturbances on aggregated roughness, small values will be used for L^* where possible. In the research performed by ter Haar (2010) it is stated that typical model calculation resolutions of several hundreds of square meters are used. It is therefore especially interesting to investigate the flow response to patches that are smaller than these dimensions, i.e. shorter than 100 meters.

Similarly to H^*, the patch length is required to meet certain requirements, which are also discussed in chapter 4.

Channel width B^*: Throughout model calculations realistic floodplain widths will be used while bearing in mind that specifically small spatial scales are of interest to the analysis. The floodplain width is allowed to vary from 50 meters to 250 meters based on a quickscan using Google Earth of the Rhine river in the Netherlands. It is found that the width of the river varies greatly over short distances. An example of this can be found around the city Arnhem, where the Rhine is restricted to 50 meter wide floodplains inside the city and 300 meter wide floodplains just after the city.

Horizontal eddy viscosity ν_{h}^*: Determining what values to use for the horizontal eddy viscosity in this analysis was difficult as values range greatly in literature. A range for ν_{h}^* between 0 and 10 $\mathrm{m}^2\ \mathrm{s}^{-1}$ has been chosen based on the research performed by ter Haar (2010).

Energy slope i_0: The energy slope drives the flow in the model and will be set to a value representing a typical energy slope in the Netherlands of 1×10^{-4} m/m.

Roughness $k_{\mathrm{N,b}}$ and $k_{\mathrm{N,p}}$: Two roughness values are required as input for this model. These are the roughness of the background vegetation and the roughness of the vegetation patch. It has been chosen to implement roughness in the form of a Nikuradse roughness height as this form of roughness is independent of water depth. Table 2.1 shows a range of roughness values as found in van Velzen et al. (2003a)

Table 2.1: *Roughness values in terms of Nikuradse roughness height k_N and corresponding Chézy values for water with a depth of 3 meters.* Source: van Velzen et al. (2003a)

Vegetation	k_N [m]	C^* at $H^* = 3$m [$m^{1/2}$ / s]
Sand	0.10	46.0
Ditch	0.15	42.8
Field	0.20	40.6
Pioneer vegetation	0.28	38.0
Natural grasslands	0.39	35.4
Wet brushwood	0.47	33.9
Sedge marsch	0.73	30.5
Dry brushwood	1.45	25.1
Dewberry brushwood	1.58	24.4
Reed Grass	2.23	21.7
Reed brushwood	11.4	9.0
Reed	12.4	8.3
Softwood alluvial forest	12.9	8.0

2.4.1 Roughness input transformation

The roughness input of the model calculations is in terms of the Nikuradse roughness height k_N due to the availability of specific roughness input values for different types of vegetation. Table 2.1 shows some typical roughness values as found by in van Velzen et al. (2003a). However, the model formulation and scaling require the roughness to be tranformed to a dimensionless drag coefficient. This is done in two steps. First, the k_N is tranformed to a Chézy equivalent, based on the water depth used for a particular calculation. The equation used will be:

$$C^* = 18 \log\left(\frac{12H^*}{k_\mathrm{N}}\right), \tag{2.13}$$

where C^* is the Chézy value in $\mathrm{m}^{1/2}\ \mathrm{s}^{-1}$, H^* is the water depth in m and k_N is the Nikuradse roughness height in m as found in van Velzen et al. (2003a). This value is then transformed to a dimensionless drag coefficient using:

$$c_\mathrm{D} = \frac{g}{C^{*2}}. \tag{2.14}$$

2.5 Determining the spatially averaged resistance

The scaled problem will be solved for $\vec{u}$ and ζ in the following chapter using a weakly non-linear analysis. The solution can then be used to determine the spatially averaged change in the downstream flow velocity. The roughness of a river segment in general can be calculated by balancing the stream wise component of the gravitational acceleration and the force of friction. In this model, this is represented by:

$$\frac{c_{\mathrm{D,eff}}\langle u^*\rangle^2}{H^*} = g^* i_0 \boldsymbol{e}_x, \tag{2.15}$$

where $\langle u^* \rangle$ is the spatially averaged flow velocity and $c_{\mathrm{D,eff}}$ is an effective drag coefficient for a river section. The flow velocity can be determined by averaging over the length of a channel segment L^*, which is typical for the roughness patch (pattern) length, and the width of the channel B^*.

$$\langle u^* \rangle = \frac{1}{L^* B^*} \int_0^{L^*} \int_0^{B^*} u^* \left(x^*, y^*\right) \, \mathrm{d}y^* \mathrm{d}x^*.$$

This allows the calculations of an effective (or aggregate) drag coefficient for a river section when the average flow velocity is determined. This average downstream flow velocity $\langle u^* \rangle$ can be determined analytically for this simplified geometry using the scaled problem as outlined in the previous section. The next chapter discusses the analytical solution up to the second order. A weakly nonlinear analysis is performed, and it is found that a spatially invariant contribution to the flow velocity arises in the second order as caused by interactions of the first order solution.

Chapter 3

Weakly Non-Linear Analysis

In this chapter the problem is analysed using a weakly non-linear analysis. First the linear problem is defined. From there an eigenfunction representation of the problem is formulated which is subsequently solved in the first and second order. Specifically the second order is of interest as it reveals a spatially independent contribution to the downstream velocity as a result of spatially varying roughness. The formula for this contribution is provided, which will form the basis for the analysis in the following chapters.

3.1 Linearization

In order to find a spatially averaged downstream velocity, which is required in equation (2.15), the model is solved analytically. The method used in this investigation is a weakly-non linear analysis. This approach assumes that the non-linear terms can be linearized, as long as the changes are gradual. This is therefore in effect a small perturbation model where the changes, in this case in bed roughness, are small compared to the mean. This deviation from the mean will be quantified using a small parameter ϵ, which can be found in the roughness formulation (3.1) and the expansion series (3.2).

The resistance term found in equation (2.10) is redefined in order to describe the spatially varying roughness as small variations with respect to a mean roughness. This reformulation is given by:

$$\mu(x, y) = \mu_0 + \epsilon\mu_1(x, y), \tag{3.1}$$

where μ_0 is a spatially constant mean resistance for the disturbed case (i.e. with roughness patches), $\mu_1(x, y)$ is the spatially varying roughness and ϵ is a small parameter that describes the magnitude of the disturbance. Figure 3.1 illustrates this situation. μ_1 will be defined so that $|\mu_1| = 1$.

The solution of this problem will be symbolically represented by $\phi = (u, v, \zeta)$. Due to the fact that $|\mu_1| = 1$, and if we require $\epsilon \ll \mu_0$, a power series expansion in ϵ may be performed where the contributions to flow velocity and free surface elevation in the n^{th} order are given by ϕ_n.

$$\phi = \sum_{n=0}^{\infty} \epsilon^n \phi_n = \phi_0 + \epsilon\phi_1 + \epsilon^2\phi_2 + \dots \tag{3.2}$$

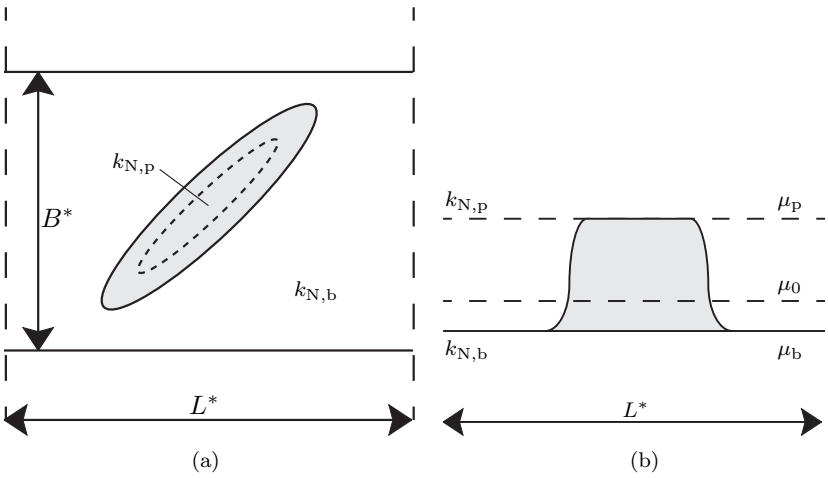

Figure 3.1: *This figure illustrates how each patch is described after the scaling procedure.* (a) *shows a random roughness patch from the top view.* (b) *shows the same patch from the side with the different roughnesses (scaled and unscaled) displayed. Specifically* μ_0 *is of interest, which is the mean roughness of the disturbed system.*

In the lowest order, where no vegetation patches are present ($\epsilon = 0$) the solution is given by:

$$\phi_0 = (u_0, v_0, \zeta_0) = (1, 0, 0),$$

which describes only basic flow in the x-direction.

3.2 The first order solution

In this section the first order solution will be found to the system using the weakly nonlinear analysis. First the linear problem is found. Then the spatially varying roughness and the problem are represented using a Fourier series projection. This representation allows the problem to be solved using linear algebra, leading to the first order solution.

3.2.1 The First Order Linear Problem

In the first order the following linear problem is formulated:

$$\mathcal{L}\phi_1 = \boldsymbol{b}_1, \tag{3.3}$$

where $\mathcal{L}$ is a linear operator describing the effects on the flow properties ϕ_1 as caused by the forcing $\boldsymbol{b}_1$, which in the first order is known to be the spatially varying roughness. The first order solution is given by the coefficients ϕ_1, which alter the flow properties as given by equation (3.2).

In order to calculate ϕ_1 it is important to determine what $\mathcal{L}$ and $\boldsymbol{b}_1$ represent in equation (3.3). This is done by substituting the expansion series as given by equation (3.2) and the reformulated spatially varying roughness as given by equation (3.1) into the scaled model defined by equations (2.10) and (2.11).

After this substitution the function is differentiated with respect to ϵ and subsequently evaluated for $\epsilon = 0$ to find only the operators acting on the quantities in the first order (i.e. the first order effects). The full derivation of the linear problem can be found in Appendix D. The following momentum equations:

$$\frac{\partial}{\partial x}u_1 + \frac{\partial}{\partial x}\zeta_1 - \nu\nabla^2 u_1 + 2\mu_0 u_1 - \mu_0 F^2 \zeta_1 = -\mu_1(x,y),$$
$$\frac{\partial}{\partial x}v_1 + \frac{\partial}{\partial y}\zeta_1 - \nu\nabla^2 v_1 + \mu_0 v_1 = 0,$$

x and y respectively, and mass balance:

$$\frac{\partial}{\partial x}\left(u_1 + F^2\zeta_1\right) + \frac{\partial}{\partial y}\left(v_1\right) = 0,$$

are found int he first order. $\mathcal{L}$ and $\boldsymbol{b}_1$ are thus given by:

$$\mathcal{L} = \begin{pmatrix} \frac{\partial}{\partial x} - \nu\nabla^2 + 2\mu_0 & 0 & \frac{\partial}{\partial x} - \mu_0 F^2 \\ 0 & \frac{\partial}{\partial x} - \nu\nabla^2 + \mu_0 & \frac{\partial}{\partial y} \\ \frac{\partial}{\partial x} & \frac{\partial}{\partial y} & F^2\frac{\partial}{\partial x} \end{pmatrix}, \qquad \boldsymbol{b}_1 = \begin{pmatrix} -\mu_1 \\ 0 \\ 0 \end{pmatrix}. \tag{3.4}$$

3.2.2 Fourier series representation

In this section the spatially varying roughness as well as the first order linear problem are rewritten using a Fourier series representation. A result of this is that finding the first order solution as given by ϕ_1 becomes much simpler as the solution can be found using matrix multiplication in the frequency domain. It will be assumed that the spatially varying roughness can be represented using a Fourier series as follows:

$$\mu_1(x,y) = \sum_{m,n} C_{mn} \exp(i\alpha_m x)\cos\beta_n y + \text{c.c.}, \tag{3.5}$$

where C_{mn} are the dimensionless complex amplitudes of the m and n^{th} mode, $\alpha_m = m$, $\beta_n = n\pi/B$ and c.c. is the complex conjugate. The amplitudes can be obtained analytically or using a Fast Fourier Transform in MATLAB.

It will be assumed that the solution holds a similar structure as seen in equation (3.5), introducing complex amplitudes $\Phi_{1mn} = (U_{1mn}, V_{1mn}, Z_{1mn})$ where the first order solution can be written as:

$$\phi_1 = \begin{pmatrix} u_1 \\ v_1 \\ \zeta_1 \end{pmatrix} = \sum_{m,n} \begin{pmatrix} U_{1mn}\cos\beta_n y \\ V_{1mn}\sin\beta_n y \\ Z_{1mn}\cos\beta_n y \end{pmatrix} \exp(i\alpha_m x) + \text{c.c.}. \tag{3.6}$$

This transverse structure stems from the boundary conditions of the system that must be met. By choosing U_{1mn} as a cosine function of y and V_{1mn} as a sine function of y the boundary conditions can be met for all values of x along both boundaries of the floodplain. Equation (3.6) can be used to rewrite equation (3.3) into a linear problem for the m, n^{th} mode. This will be done

by substituting equation (3.6) into the original linear problem. The full derivation can be found in Appendix E. The first order linear problem as posed by equation (3.3) for the m and n^{th} mode in the frequency domain is given by:

$$\mathbf{A}_{mn}\Phi_{1mn} = \mathcal{S}_{1mn}, \tag{3.7}$$

where $\mathbf{A}_{mn}$ is the Fourier series representation of the linear operator $\mathcal{L}$ and $\mathcal{S}_{1mn}$ is the Fourier series representation of the forcing $\boldsymbol{b}_1$. These two terms are given by:

$$\mathbf{A}_{mn} = \begin{pmatrix} X_2 & 0 & i\alpha_m - \mu_0 F^2 \\ 0 & X_1 & -\beta_n \\ i\alpha_m & \beta_n & i\alpha_m F^2 \end{pmatrix} \qquad \text{and} \qquad \mathcal{S}_{1mn} = \begin{pmatrix} -C_{mn} \\ 0 \\ 0 \end{pmatrix}, \tag{3.8}$$

where $X_p = i\alpha_m + \nu(\alpha_m^2 + \beta_n^2) + p\mu_0$ for $p = 1, 2$ has been introduced for shorter notation.

3.2.3 First order solution

The next step is to find the first order solution. Now that the problem has been posed in the Fourier space, solving it has become a matter of matrix algebra. The system as defined by equation (3.7) can be solved by multiplying both sides by the inverse of $\mathbf{A}_{mn}$:

$$\Phi_{1mn} = \mathbf{A}_{mn}^{-1}\mathcal{S}_{1mn}. \tag{3.9}$$

This leads to complex amplitudes that, when substituted into equation (3.6), provide the first order influence on the flow properties. The derivation of the inverse of matrix $\mathbf{A}_{mn}$ can be found in Appendix F. Utilizing equation (3.9) it can be stated that the complex amplitudes of the m, n^{th} mode are given by:

$$\Phi_{1mn} = \begin{pmatrix} U_{1mn} \\ V_{1mn} \\ Z_{1mn} \end{pmatrix} = \frac{-C_{mn}}{D_{mn}} \begin{pmatrix} X_1 i\alpha_m F^2 + \beta_n^2 \\ -\beta_n i\alpha_m \\ -X_1 i\alpha_m \end{pmatrix}, \tag{3.10}$$

with determinant:

$$D_{m,n} = X_1\alpha_m^2 + X_2\beta_n^2 + X_1 X_3 i\alpha_m F^2, \tag{3.11}$$

where $X_p = i\alpha_m + \nu(\alpha_m^2 + \beta_n^2) + p\mu_0$ for $p = 1, 2, 3$. The first order solution is then given by substituting these amplitudes into equation (3.6).

3.3 Second order solution

In this section the second order solution is found. First the linear problem is defined for the second order. It is found that the forcing of the second order linear problem consists of convolutions of the first order solution. The forcing of the system is used to identify terms that lead to a spatially invariant contribution to the flow velocity. Finally, spatial averaging is performed, which leads to a spatially invariant contribution to the flow velocity in the second order. This contribution can be used to determine the aggregate roughness.

3.3.1 The second order linear problem

In the second order a similar problem is found as in the first order. By taking the second order derivative (instead of the first order) of ϵ after substitution and then evaluating for $\epsilon = 0$ only the contribution of the second order remains. This leads to the following linear problem:

$$\mathcal{L} \cdot \phi_2 = \boldsymbol{b}_2, \tag{3.12}$$

where $\mathcal{L}$ is the same linear operator as found in the first order, $\phi_2 = (u_2, v_2, \zeta_2)$ contains the second order effects and $\boldsymbol{b}_2$ contains the forcing of the second order solution. This last part also contains the most significant difference between the first and the second order solution. Specifically the non-linear terms in the momentum equations and the continuity equation leave contributions of the first order as forcing for the second order. Appendix G shows how the following forcing terms have been derived for the second order problem:

$$\mathcal{L}\phi_2 = \boldsymbol{b}_2 \qquad \text{where} \qquad \boldsymbol{b}_2 = -\begin{pmatrix} \mathcal{A}_x + \mathcal{R}_x \\ \mathcal{A}_y + \mathcal{R}_y \\ \mathcal{M} \end{pmatrix}, \tag{3.13}$$

and:

$$\begin{aligned}
\mathcal{A}_x &= u_1 \frac{\partial u_1}{\partial x} + v_1 \frac{\partial u_1}{\partial y}, \\
\mathcal{A}_y &= u_1 \frac{\partial v_1}{\partial x} + v_1 \frac{\partial v_1}{\partial y}, \\
\mathcal{R}_x &= \mu_0 \left(u_1 - F^2 \zeta_1\right)^2 + \mu_0 \frac{1}{2} v_1^2 + \mu_1 \left(2u_1 - F^2 \zeta_1\right), \\
\mathcal{R}_y &= \mu_0 v_1 \left(u_1 - F^2 \zeta_1\right) + \mu_1 v_1, \\
\mathcal{M} &= F^2 \nabla \cdot \left(\zeta_1 \vec{u}_1\right).
\end{aligned}$$

In the previous definition $\mathcal{A}$ refers to source terms arising from the non-linearity of the advective processes in both the x and y direction, $\mathcal{R}$ refers to the source terms arising from the non-linearities in the resistance term and $\mathcal{M}$ refers to the combined variations in free surface and flow velocity as found in the mass balance.

By rewriting the forcing in the second order using similar Fourier series as in the first order, individual contributions can be calculated. These rewritten forcing terms can also be found in appendix G. However, this still leads to a spatially dependent solution while the goal of this research is to find an aggregate roughness value for a region based on the smaller disturbances within. To this end, a spatially invariant contribution to the flow velocity can be determined in the second order, which is derived in the following section.

3.3.2 Spatially invariant contribution

In Fourier space, the second order forcing terms, as derived in the previous section, are found to be convolutions of the solutions of the first order problem. As a result the forcing in the second order can be projected onto the same set of eigenfunctions given by equation (3.6). This allows the evaluation of a spatially invariant part of the solution denoted by $\Phi_{2,00}$.

For the spatially invariant part $\Phi_{2,00} = (U_{2,00}, V_{2,00}, Z_{2,00})$, the problem as given by equation (3.13) after projection onto the eigenfunctions is given by:

$$\begin{pmatrix} 2\mu_0 & 0 & -\mu_0 F^2 \\ 0 & \mu_0 & 0 \\ 0 & 0 & 0 \end{pmatrix} \begin{pmatrix} U_{200} \\ V_{200} \\ Z_{200} \end{pmatrix} = - \begin{pmatrix} \langle \mathcal{A}_x + \mathcal{R}_x \rangle \\ \langle \mathcal{A}_y + \mathcal{R}_y \rangle \\ \langle \mathcal{M} \rangle \end{pmatrix}.$$

Please note that this simplification is caused solely by substituting in $\alpha_0 = \beta_0 = 0$ as $\partial/\partial x = 0$ and $\partial/\partial y = 0$ for the spatially invariant part.

From a more physical perspective, it can be stated that due to the conservation of mass that there may be no spatially invariant rise or lowering of the water level meaning that $Z_{2,00} = 0$[1]. Furthermore, the boundary conditions state that the transverse flow at the boundaries must be zero. This leads to the result that $V_{2,00} = 0$. The spatially independent flow velocity contributions as caused by a roughness patch can then be found by taking the spatial average of $U_{2,00}$, which is found to be:

$$U_{2,00} = -\frac{\langle \mathcal{A}_x + \mathcal{R}_x \rangle}{2\mu_0}, \qquad V_{2,00} = 0, \qquad Z_{2,00} = 0. \tag{3.14}$$

This spatially invariant contribution to the mean flow in the second order is a particularly interesting mode, as it offers a means to use convolutions of the flow properties in the first order to determine an aggregated flow resistance. The terms describing these convolutions have been found both in real values and as their projections onto the proposed eigenfunctions. By spatially averaging these terms a base contribution can be found that affects the mean flow in the flow channel. A quick scan of the projections can show whether a spatially invariant contribution of that terms exists. The spatial average is defined as:

$$\langle u^* \rangle = \frac{1}{B^* L^*} \int_0^{L^*} \int_0^{B^*} u^*(x^*, y^*) \mathrm{d}y^* \mathrm{d}x^*.$$

Due to the fact that α_m is chosen so that the patches recur after a length of 2π, it can be stated that $\langle \exp 2i\alpha_m x \rangle = 0$. Similarly, any term where a double angle is found in the real part of the solution, spatially averaging this would lead to a trivial result: $\langle \sin(2\beta_n y) \rangle = \langle \cos(2\beta_n y) \rangle = 0$. These two conclusions allow a quick assessment of all eigenfunction projection (as found in appendix G) and allow the conclusion that only the following terms contribute to the mean flow after the spatial averaging:

$$\underbrace{v_1 \frac{\partial u_1}{\partial y}}_{\mathcal{A}_x}, \qquad \underbrace{\mu_0 \left(u_1 - F^2 \zeta_1\right)^2, \qquad \frac{1}{2}\mu_0 v_1^2, \qquad \mu_1 \left(2u_1 - F^2 \zeta_1\right)}_{\mathcal{R}_x}. \tag{3.15}$$

This corresponds to the conclusion made earlier where it was stated that the spatially invariant contribution is only found in the downstream direction. The contributions to the flow in the transverse direction and the free surface elevation are trivial after spatial averaging.

The spatial average of each of these terms is subsequently evaluated to find the base contribution to $U_{2,00}$ as described in equation (3.14). Note that these

[1] Note that the mean water level H^* remains constant in this analysis and not the discharge.

contributing terms are all in the downstream direction. Two important trigonometric identities will be used in all four cases, which are:

$$\cos^2 \beta_n y = \frac{1}{2} + \frac{1}{2}\cos(2\beta_n y) \qquad \text{and} \qquad \sin^2 \beta_n y = \frac{1}{2} - \frac{1}{2}\cos(2\beta_n y).$$

Through spatially averaging these terms only the $\frac{1}{2}$ will remain as the double angle terms equal zero as stated previously.

3.3.3 Spatial average of contributing terms

This final section of the weakly non-linear analysis discusses the spatial average of the four contributing terms as found in the previous chapter. Together these four terms describe the change of the flow in the second order. The derivation of the spatial invariant contribution in the second order can be found in appendix H. The following relationship is found, which can be used to calculate an aggregated flow velocity for a river section based on smaller patch disturbances:

$$\begin{aligned} U_{2,00} = \sum_{mn} -\frac{|C_{mn}|^2}{4\mu_0|D_{mn}|^2}[&\alpha_m^2\beta_n^2F^2\left(X_{1,mn} + \overline{X_{1,mn}}\right) + \dots \\ &2\mu_0\left(4\alpha_m^2F^4|X_{1,mn}|^2 - 3\alpha_m^2\beta_n^2F^2 + \beta_n^4\right) + \dots \\ &\mu_0\alpha_m^2\beta_n^2 + \dots \\ &\left(3\alpha_m^2F^2 - 2\beta_n^2\right)\left(D_{mn} + \overline{D_{mn}}\right)], \end{aligned} \tag{3.16}$$

where an overline such as found in $\overline{D_{mn}}$ denotes the complex conjugate of that variable.

Equation (3.16) shows how the four contributions in the downstream direction influence the spatially invariant flow velocity in the second order. The four terms share a common factor, which depends on the redistributed average roughness μ_0, and the spatially varying roughness in the Fourier space C_{mn}. In chapter 5 a simple patch description[2] is used, in order to understand how each of the terms in this equation influences the downstream flow velocity. The following relationship describes, in general terms, the spatially invariant flow velocity change in the second order when such a patch is considered:

$$\begin{aligned} U_{2,00} = -\frac{|C|^2}{4\mu_0|D|^2}[\ &\overbrace{\alpha^2\beta^2F^2\left(X_1 + \overline{X_1}\right)}^{v_1\frac{\partial u_1}{\partial y}} + \overbrace{2\mu_0\left(4\alpha^2F^4|X_1|^2 - 3\alpha^2\beta^2F^2 + \beta^4\right)}^{\mu_0(u_1 - F^2\zeta_1)^2}\dots \\ &+ \underbrace{\mu_0\alpha^2\beta^2}_{\frac{1}{2}\mu_0 v_1^2} + \underbrace{\left(3\alpha^2F^2 - 2\beta^2\right)\left(D + \overline{D}\right)}_{\mu_1(2u_1 - F^2\zeta_1)}\ ]. \end{aligned} \tag{3.17}$$

Several processes can be identified in the equation above. Each of the term can be related to one or more physical processes. They are briefly outlined here:

- $v_1\frac{\partial u_1}{\partial y}$ is identified as the lateral redistribution of longitudinal momentum.

[2] A simple patch description is considered to be a roughness patch that can be described using only one complex amplitude C_{mn}

- $0.5\mu_0 v_1^2$ is identified as the transverse component of the resistance to flow of the first order solution as caused by the background roughness.
- $\mu_0 \left(u_1 - F^2\zeta_1\right)^2$ consists of three distinguishable terms, which are: i) the streamwise component of the resistance ot flow of the first order solution as caused by the background roughness $mu_0u_1^2$, ii) the backwater effects with respect to the background roughness $\mu_0 F^4\zeta_1^2$ and iii) ???
- $\mu_1 \left(2u_1 - F^2\zeta_1\right)$ consists of two terms, which are: i) the backwater effects with respect to the spatially varying roughness and ii) ???

It is of interest to note that the solution for $U_{2,00}$ consists entirely of real contributions. Using equation (3.6) it can be concluded that $\langle u_2 \rangle = U_{2,00} \cos 0 \exp 0 = U_{2,00}$. As a result, the spatially independent influence of a vegetation patch up to the second order in ϵ can be represented as:

$$\langle u^* \rangle = U^* \left(1 + \epsilon^2 \langle u_2 \rangle\right) \tag{3.18}$$

where $\langle u^* \rangle$ is the spatially averaged dimensional flow velocity, U^* is the velocity scale as found in equation (2.7) before the roughness disturbance and ϵ is the linearization parameter. This result can be used to estimate the aggregated roughness induced by the roughness patch(es) through:

$$c_{\mathrm{D,eff}} = \frac{g^* H^* i_0}{\langle u^* \rangle^2} \tag{3.19}$$

3.4 Summary

In this chapter the weakly nonlinear analysis was performed. It was assumed that the spatially varying roughness and the solution can be seen as small disturbances with respect to some background or base value. In the second order a spatially invariant contribution to the downstream flow velocity is found that consists of terms which are interactions of the first order solution. This contribution can be used to determine a new aggregate resistance for the entire section as induced by the spatially varying roughness.

Before continuing on to the model results, an analysis will be performed to identify the limitations of the proposed methods. The linearization allows only small difference is roughness and the advection term in the momentum balance should not have a greater influence than the resistance terms for the model to be applicable. These limitations are explored in the next chapter before the solution to the problem is presented.

Chapter 4

Model applicability restrictions

In this chapter the restrictions of model application caused by the linearization approach are discussed. It is of importance to understand what input variables influence model output and for what regions of these input values the analysis may be used. The restrictions of the method used for this analysis will be analyzed to identify where the model is valid, and where it is not. Recalling that the linearization occurs in:

$$\mu(x, y) = \mu_0 + \epsilon\mu_1(x, y),$$

and that an expansion of the solution is performed in ϵ for

$$\sum_{n=0}^{\infty} \epsilon^n \phi_n = \phi_0 + \epsilon\phi_1 + \epsilon^2\phi_2 + \dots$$

The method used leads to two main restrictions that need to be kept in mind when analysing certain combinations of input values. These restrictions are caused by two conditions:

1. The linearization parameter ϵ must be sufficiently small in order to allow truncation of the solution after the second order.
2. When expanded the nonlinear terms in the momentum equations and the continuity equations must be of the same order or smaller than the resistance term in order to guarantee weakly nonlinear behaviour for the entire system of equations.

In order to understand the origin of these input restrictions, the scales of the system are reiterated here briefly. The scales used to perform the scaling operation were a typical velocity scale and an elevation scale, which are give by:

$$U^* = \sqrt{\frac{g^* i_0 H^*}{c_{\mathrm{D},0}}} \qquad \text{and} \qquad Z^* = \frac{U^{*2}}{g^*} = \frac{i_0 H^*}{c_{\mathrm{D,b}}} \tag{4.1}$$

respectively. The scaling procedure then leads to four dimensionless scales:

$$F = \frac{U^*}{\sqrt{g^* H^*}}, \qquad \nu = \frac{\nu_{\mathrm{h}}^*}{U^* L^*}, \qquad \mu = \frac{c_{\mathrm{D}} L^*}{H^*}, \qquad \text{and} \qquad \mu_0 = \frac{c_{\mathrm{D},0} L^*}{H^*}, \tag{4.2}$$

which are the Froude number, the scaled spatially constant horizontal eddy viscosity, the scaled spatially varying resistance and the scaled resistance when no patches are present, respectively. These scales allow the identification of the input parameters relevant to this system. These are a total of seven system parameters that influence the calculations, which are: the water depth H^*, patch pattern recurrence length L^*, channel width B^*, eddy viscosity ν_{h}^*, energy slope i_0, the background roughness $k_{\mathrm{N,b}}$ and the vegetation patch roughness $k_{\mathrm{N,p}}$[1]. The scaled mean roughness μ_0 is calculated using these two roughness inputs.

4.1 Perturbation model limitations

The small perturbation model leads to two limitations that will be discussed in this section. The first restriction is caused by the truncation of the solution after the second order and the second restriction is found in the reformulation of the roughness; here it is assumed that the roughness variations are small perturbations from some mean roughness. It is found that the first restriction is limiting for the model application and that the second restriction can be used to determine a minimum value for H^* and L^*.

4.1.1 Truncation of the solution

The expansion series used in this analysis uses higher orders of the solution (i.e. $\epsilon^2\phi_2$, $\epsilon^3\phi_3$ etc.) to 'correct' the approximation of the cumulative result of the lower orders. As the order number increases, the adjustments needs to become smaller in order to allow truncation of the expansion series. As a result it can be stated that ϵ needs to be a small parameter (i.e. $\epsilon \ll 1$). If this condition is not met, higher orders of the solution will significantly influence the solution. This would require their consideration for the analysis.

Figure 4.1(b) shows a contour line for different values of H^* and L^* where $\epsilon = 0.25$. The combinations of H^* and L^* above this line are acceptable with respect to this restriction. Note that this line in combination with the line in figure 4.1(a) leads to a field of applicability for the model. In retrospect it appears that the linearization parameter ϵ may have been an unfortunate choice. The reason for this can be found in the reformulated roughness. The expansion used requires ϵ to be small in an absolute sense, while the reformulation of the roughness assumes that the roughness variations are small *compared to the mean*. If the roughness formulation were divided by μ_0 this latter condition would be represented also in the expansion series:

$$\frac{\mu(x,y)}{\mu_0} = \frac{\mu_0}{\mu_0} + \frac{\epsilon}{\mu_0}\mu_1(x,y) = 1 + \tilde{\epsilon}\mu_1(x,y),$$

where $\tilde{\epsilon}$ could be used in the expansion series so that the relative difference between μ_0 and μ_1 is used in the expansion and not the absolute difference. This would require all of the model equations (momentum and continuity) to be divided by μ_0.

[1] Recalling that the roughness is translated to a dimensionless drag coefficient by first calculating the Chézy value corresponding to the water level using $C^* = 18\log(12H^*/k_{\mathrm{N}})$, which can subsequently be translated using $c_{\mathrm{D}} = g^*/C^{*2}$

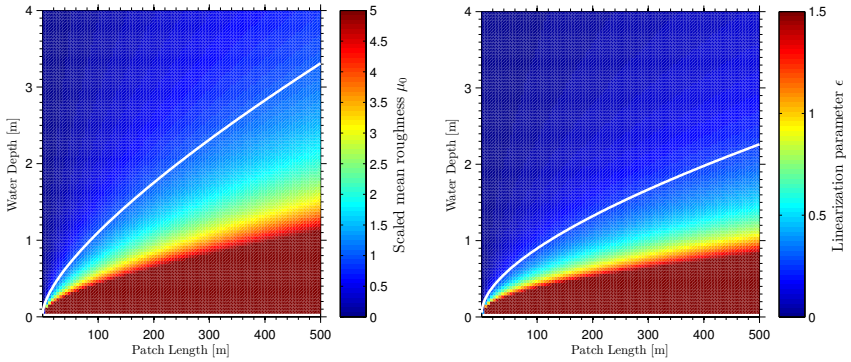

(a) (b)

Figure 4.1: *Restrictions as caused by the analysis.* (a) *shows the contour line at the value* $\mu_0 = 1$ *and* (b) *shows the contour line where* $\epsilon = 0.25$. *These two conditions lead to a field of application for which the model may be used.*

4.1.2 Small perturbation

A second condition imposed by the linearization can found in the definition of the spatially varying roughness as given by equation (3.1). This requires the variations to be approximately an order of magnitude smaller than the base case. This can be symbolically represented as:

$$\epsilon\mu_1(x, y) \ll \mu_0$$

The small parameter ϵ is defined such that the scaled spatially varying roughness $|\mu_1(x, y)|$ is of order 1. This leads to the fact that there is a maximum value for ϵ that this analysis permits. This maximum value for epsilon will be symbolically represented by $\epsilon_{\max}$ and the following statement must then always be true in the case of small perturbations:

$$\epsilon \leq \epsilon_{\max}\mu_0$$

This limitation can be used to find the water depth required for a certain patch length[2]. As a result, a minimum water depth $H^*_{\min}$ for a particular combination of background and patch roughness can be found. The following two equations are used to determine ϵ and μ_0 and can be used to find $H^*_{\min}$ analytically.

$$\epsilon = \frac{\mu_p - \mu_b}{2} \qquad \text{and} \qquad \mu_0 = \mu_\text{b} + \epsilon C_{00}$$

There are two cases that are be considered based on the methodology of this study; these are the simple patches and the complex patches. The simple patches are constructed using only one Fourier mode and in those cases μ_0 lies exactly between μ_b and μ_p. In those cases $H^*_{\min}$ can be found using the following

[2]This restriction results in limiting conditions for H^* and L^* due to the fact that μ is determined using the ratio L^*/H^*.

relationship:

$$H^*_{\min} = \frac{1}{12}\left(\frac{k_{\mathrm{N,p}}}{k_{\mathrm{N,b}}}\right)^{\frac{1}{2}\frac{1-\epsilon_{\max}+\sqrt{1-\epsilon^2_{\max}}}{\epsilon_{\max}}} k_{\mathrm{N,p}}. \tag{4.3}$$

The complex patterns can have any number of modes and thus adhere to a more general formula. The Fourier transformation of complex patches will return a base mode C_{00} that can be used to correct the offset caused by the Fourier transformation. This minimum water depth is then defined as:

$$H^*_{\min} = \frac{1}{12}\left(\frac{k_{\mathrm{N,p}}}{k_{\mathrm{N,b}}}\right)^{-\frac{1}{2}\frac{C_{00}-2+C_{00}\epsilon_{\max}-\sqrt{(1+\epsilon_{\max})(C^2_{00}\epsilon_{\max}-2C_{00}\epsilon_{\max}+C^2_{00}-4C_{00}+4)}}{\epsilon_{\max}}} k_{\mathrm{N,p}}. \tag{4.4}$$

Therefore it can be stated that $H^*_{\min}$ depends solely on $k_{\mathrm{N,b}}$, $k_{\mathrm{N,p}}$ E, and C_{00}. The first three are input parameters and the C_{00} depends on the coverage fraction of the vegetation types in the complex patch patterns. The minimum water depth can be used to find a minimum patch length. This allows the identification of the smallest spatial scales for which certain roughness combinations can be modelled.

4.2 Linearization limitations

The weakly nonlinear analysis requires the roughness term in the momentum equation to be of equal magnitude or larger than the other nonlinear terms in the equations. This is a restriction caused by the assumption that individual orders of the solution are not severely influenced by other orders of the solution, which would be deemed strong nonlinear behaviour. The expansion as seen in equation (3.2) would not be valid if any of the nonlinear terms in the scaled equations do not behave linearly enough. In other words, in order to allow the superposition of individual orders, it is required that each of the terms behaves in a linear fashion. This can be accomplished by setting a minimum requirement for the magnitude of the scaled roughness so that it is larger than all other nonlinear terms in the equations.

Due to the fact that the advective term is the only other nonlinear term in the flow equations it will be stated that the magnitude of the advective term needs to be smaller or of the same order as the resistance formulation.

$$\frac{U^{*2}}{L^*} \leq c_{\mathrm{D0}}\frac{U^{*2}}{H^*}$$

where c_{D0} is the mean drag coefficient of the disturbed state. The velocity scale may be elimated from this equation as it contributes both terms equally leaving:

$$\frac{1}{L^*} \leq \frac{c_{\mathrm{D0}}}{H^*}$$

Simplifying this further leads to an equation for one of the typical scales of the system as defined in the previous section:

$$c_{\mathrm{D0}}\frac{L^*}{H^*} = \mu_0 \qquad \therefore \qquad \mu_0 \geq 1 \tag{4.5}$$

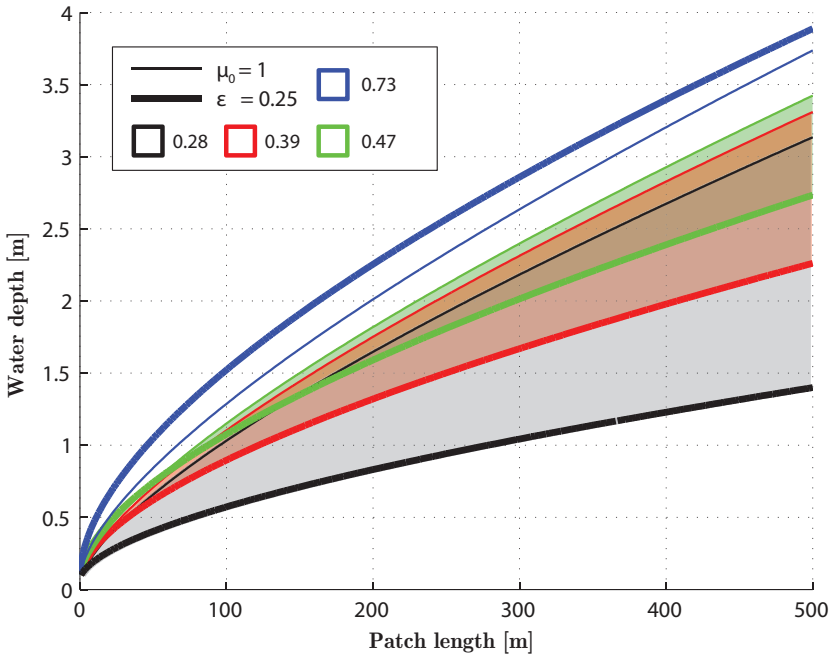

Figure 4.2: *Illustration of the combinations of L^* and H^* allowed with $k_{N,b} = 0.20$ and $k_{N,p} = 0.28, 0.39, 0.47$ and 0.73 and $\epsilon_{max} = 0.25$. The thin line shows the restriction imposed by the relative importance of advection and friction; the thick line shows the lower boundary as a result of the small perturbation model. The colored fields illustrate what region of this figure is usable for analysis. Note the point where $k_{N,p} = 0.73$ can be analyzed lies outside of the axis of this figure. The two lines intersect outside of this image.*

There are many input variables that have an effect on the magnitude of the scaled dimensionless friction. These are the water depth H^* and the length of the patch pattern L^* as can be seen from its definition, but also the Nikuradse roughness of the patch $k_{\mathrm{N,p}}$ and the background $k_{\mathrm{N,b}}$ vegetation influences this value as can be seen in Figure 3.1.

Figure 4.1(a) shows the contour line where $\mu_0 = 1$ for the specific case where $k_{\mathrm{N,b}} = 0.20$ m and $k_{\mathrm{N,p}} = 0.39$ m. All combinations of L^* and H^* underneath this curve are feasible options (i.e. $\mu_0 > 1$) with regards to this constraint.

4.3 Range of applicability

These restrictions can be combined in a single figure to illustrate for what combinations of H^* and L^* the model can be applied. Figure 4.2 shows a range of values where the model is applicable. In this figure the base roughness is that of a field with patches in the form of pioneer vegetation, natural grasslands and wet brushwood. A maximum value for epsilon of 0.25 is set, which leads to the ranges displayed. Note that small values of H^* and L^* are only acceptable for very small differences in roughness and only for very small variations.

Table 4.1: *This table shows for what combinations of roughness types the model is applicable while also showing the minimum required values for L^* and H^* at $\epsilon_{max} = 0.25$*

E = 0.25	Back-ground	Sand		Ditch		Field		Pioneer Vegeta-tion		Natural grass-lands		Wet brush-wood		Sedge Marsch		Dry brush-wood		Dewberry brush-wood		Reed grass		Reed brush-wood		Reed		Softwood Alluvial Forest	
	k	0.10		0.15		0.20		0.28		0.39		0.47		0.73		1.45		1.58		2.23		11.4		12.4		12.9	
Patch	k	H	L	H	L	H	L	H	L	H	L	H	L	H	L	H	L	H	L	H	L	H	L	H	L	H	L
Sand	0.10	0	0																								
Nevengeul	0.15	0.1	0.8	0	0																						
Field	0.20	0.2	8	0	0.4	0	0																				
Pioneer Vegetation	0.28	0.8	77	0.2	7.2	0.1	0.8	0	0																		
Natural grasslands	0.39	3.5	575	0.9	72	0.3	13	0.1	1.1	0	0																
Wet brushwood	0.47	8	####	2	233	0.7	49	0.2	5.8	0.1	0.2	0	0														
Sedge Marsch	0.73	56	####	14	####	5.2	779	1.6	137	0.5	19	0.3	5	0.1	0												
Dry brushwood	1.45			294	####	109	####	34	####	11	####	5.8	663	1.3	56	0.1	####										
Dewberry brushwood	1.58			430	####	160	####	50	####	16	####	8.5	####	1.9	103	0.2	0.1	0.1	####								
Reed grass	2.23					738	####	232	####	74	####	39	####	8.6	969	0.8	14	0.6	6.8	0.2	0						
Reed brushwood	11.4																	845	####	259	####	1	####				
Reed	12.4																			376	####	1.4	0.9	1	####		
Softwood Alluvial Forest	12.9																			448	####	1.6	2.4	1.2	0.2	1.1	####

The minimum values for H^* and L^* that may be used in an analysis, shown in the bottom left corner of any range in Figure 4.2, can be found analytically. Table 4.1 shows the minimum values for all combinations of roughness types found in Table 2.1 at $\epsilon_{\max} = 0.20$. Colour coding has been used to identify ranges that are useful, less useful and useless based on the aim of this research. Green represents that a combination is useful ($0 \leq H^* \leq 5$ and $0 \leq L^* \leq 250$), yellow shows that the usefulness is marginal as patch lengths and water depths are already too high for the analysis of roughness patches on a small scales while the values are still realistic ($5 < H^* \leq 10$ and $250 < L^* \leq 500$) and red marks all values outside of these two ranges, which thus carry no significance for the analysis.

Additional tables can be found in appendix I for different values of $\epsilon_{\max}$. In these tables it becomes evident that smaller values of epsilon further restrict the applicability of the model.

4.4 Summary

In this chapter the ranges of application of the model have been discussed as caused by the solution method. It has been shown that certain ranges of H^* and L^* may be modelled for specific combinations of background and patch vegetation. Additionally minimum values $H^*_{\min}$ and $L^*_{\min}$ were found for which the model applies.

Some modelling choices will be made as a result of this analysis. It is suggested that $\epsilon_{\max} = 0.25$ is used for the analysis as it still allows relatively short patch lengths and shallow water depths for a base roughness value of $k_{N,b} = 0.20$ m (field). This allows the use of up to 3 other roughness types for the vegetation patches. It is important to investigate patches specifically at small spatial scales as this is the region for which aggregated roughness values are sought.

Finally, it is important to note that relatively large patch length and water depths are required, even at very small differences in roughness. At $L^* = 100$ for $k_{N,b} = 0.20$ and $k_{N,b} = 0.28$ the water depth is only allowed to vary between $0.55 \leq H^* \leq 1$ meter. Similarly, in order to model a water depth of 5 meters,

as done by ter Haar (2010), a patch lengths L^* of approximately 1200 meters is required. These lengths are beyond the usefulness of this modelling approach and therefore no modelling will be done at larger water depths.

Chapter 5

Results: Simple roughness patch patterns

In this chapter a relatively simple single mode roughness patch decription is used to identify principal physical processes and phenomenon that may be more difficult to distinguish using more complex patch shapes or patterns. Three individual roughness patterns will be modelled through defining a fixed value to the complex coefficient C_{mn}, which is used to describe the spatially varying roughness while setting all remaining modes in $C_{mn} = 0$. The three cases that will be considered are $C_{10} = \frac{1}{2}$, $C_{01} = \frac{1}{2}$ and $C_{11} = \frac{1}{2}$ which describe serial, parallel and alternating roughness respectively. Roughness changes are gradual due to the fact that only one mode is considered.

For the analysis in this chapter, five variables were used as input to investigate how they each affect the model output. These variable were $H^*, L^*, B^*, \nu_{\mathrm{h}}^*$ and i_0. For each calculation all variables were kept at a constant value with the exception of the variable to be investigated. The input values of the variables can be seen in table 5.1.

The ranges are based on the allowable ranges found in the chapter 4 and ter Haar (2010). Finally $k_{\mathrm{N,b}} = 0.20$ m during model calculations and the vegetation patch roughness was set to $k_{\mathrm{N,p}} = 0.28$ m in order to allow a the largest range of input values for H^* and L^* while retaining relatively short spatial scales.

Table 5.1: *Input variable values for the model calculations for the simple patch descriptions.*

		Constant	Range
H^*	[m]	1	$0.5 - 1.2$
L^*	[m]	100	$90 - 250$
B^*	[m]	100	$10 - 250$
ν_{h}^*	[$\mathrm{m^2\ s^{-1}}$]	5	$0 - 10$
i_0	[m]	1×10^{-4}	$1 \times 10^{-5} - 1 \times 10^{-3}$

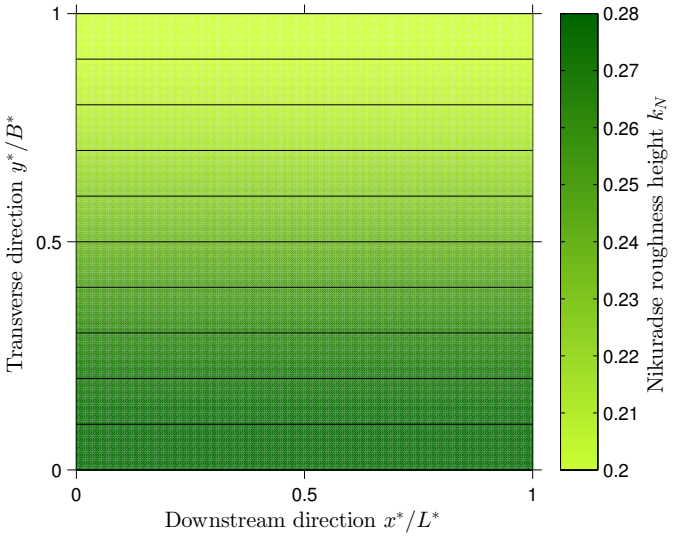

(a)

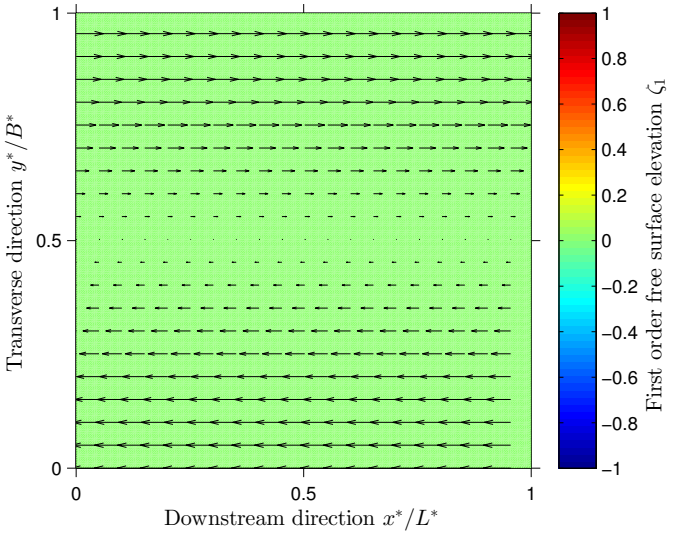

(b)

Figure 5.1: *Surface plot of the vegetation pattern* (a) *and the first order free surface elevation* (b)*. The roughness pattern is described by the mode* $C_{01} = 1/2$*.* $k_{N,b} = 0.20$ *and* $k_{N,p} = 0.28$*. The axes show a scaled length scale as the patch stretches in the streamwise and transverse direction depending on the input for* L^* *and* B^**. The lines in the top figure are the streamlines of the flow up to the first order, the vectors in the bottom plot show the first order velocities* (u_1, v_1)*. The arrows clearly show that the flow velocity reduces over the roughness patch and accelerates over the base roughness.*

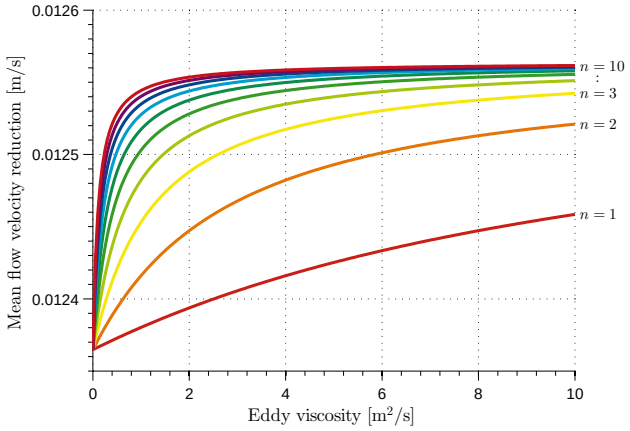

Figure 5.2: *Influence of the eddy viscosity on the flow velocity for different mode number n describing the layout of the parallel roughness patches. A higher mode number n corresponds with a greater number parallel patches in the river segment. There are two interesting results that may be observed in this figure: i) a maximum change in velocity can be found as a result of shear effects irrespective of the eddy viscosity value and ii) this maximum is reached sooner when the number of parallel patches in a river segment of equal dimensions increases.*

5.1 Parallel roughness patches

Parallel (or transverse) roughness can be described by setting the complex coefficient $C_{01} = \frac{1}{2}$ while setting all other values for $C_{mn} = 0$. Utilizing equation (3.5) it can be stated that the spatially varying roughness is defined using:

$$\mu_1(x, y) = \frac{1}{2}\exp(0)\cos(\beta y) + \text{c.c.} = \cos(\beta y).$$

In this case the wave number $\alpha = 0$ and the wave number $\beta = \pi/B$. The system shows a patch pattern (see figure 5.1(a)) where the roughness is high at one side of the channel and low at the opposing side. The spatially averaged flow contribution in the second order can be found utilizing equation (3.17). Substitution, expansion and subsequent simplification allows the solution for $\langle u_2 \rangle$ to be simplified to:

$$\langle u_2 \rangle = -\frac{1}{8}\frac{(3\mu_0 + 2\nu\beta^2)}{\mu_0(2\mu_0 + \nu\beta^2)^2}. \tag{5.1}$$

What becomes clear is that the terms $v_1\frac{\partial u_1}{\partial y}$ and $\frac{1}{2}\mu_0 v_1$ are reduced to zero and do not contribute to the flow velocity in the second order for such a patch description. The cause of this is that there is no transverse velocity contribution v_1 in the first order. This only arises, as can be seen in equation (3.10), when the roughness patch description has both a streamwise and transverse structure, i.e. $\alpha_m \neq 0$ and $\beta_n \neq 0$.

Equation (3.10) also shows that no free surface elevation arises when $\alpha = 0$, which can also be seen in figure 5.1(b). As a result no backwater effects occur,

which therefore allows the conclusion that the only influence found in the second order originates from interactions in the resistance terms $2\mu_1 u_1$ and $\mu_0 u_1^2$. These terms describe the resistance in the downstream direction of the disturbed flow for both the background roughness and the spatially varying roughness.

A final simplification to the solution can be made for the case where the eddy viscosity is ignored. This leads to the following relationship for the second order spatially invariant contribution:

$$\langle u_2 \rangle = -\frac{3}{32\mu_0^2} = -\frac{3}{8}\frac{|C|^2}{\mu_0^2}, \tag{5.2}$$

where the last term has been added to provide a more general formulation of the roughness based on the patch description. It is particularly of interest to note that this final formulation is independent of wave numbers in the streamwise and transverse direction. As a result it can be concluded that some base roughness increase always arises for spatially varying roughness irrespective of the layout of these patches. This base roughness increase depends solely on the mean roughness μ_0 and the amplitude (or magnitude) of the independent components of the spatially varying roughness C_{mn}.

Consequently, it means that additional roughness (on top of this background roughness) of roughness patches oriented parallel to the principal flow direction can be attributed solely to viscous effects. The influence of the shearing effects, as encompassed in the eddy viscosity, can be seen in figure 5.2. There are two interesting conclusions that can be drawn from this figure. The first is that there appears to be a maximum influence of the shearing effects on the flow velocity reduction.

Secondly, this maximum influence of shearing effects is reached at a lower eddy viscosity when the wave number n increases, i.e. when more parallel patches occur within the same channel section. This can be explained by the fact that a high ν_{h}^* represents a more turbulent flow, which results in larger shear layers. A slow transitions from smooth to rough allows the flow to adapt fully, but more rapid transitions (higher values of n) will lead to overlapping shear layers preventing full flow adaptation. This overlapping occurs sooner when the eddy viscosity is higher as the shear layers increase in width. This interaction, where turbulent flow cannot fully adapt, is observed as the maximum flow velocity influence.

Model calculations have been performed in order to find what input variables affect the mean flow velocity in the channel. Figure 5.3 and Figure 5.4 show how the average velocity over the roughness patch changes with respect to various input variables. From these figures it can be seen that the pattern length L^*, the channel width B^* and the eddy viscosity ν_{h}^* appear to have very little effect on the mean flow velocity in the channel in comparison to the water depth H^* and the energy slope i_0. This influence of H^* and i_0 is easily explained using the Chézy relationship, which directly relates water depth and energy slope to roughness. This relationship shows that as H and i_0 increase so will the smoothness, which is what the model shows.

Figure 5.4 shows how the change in the spatially averaged flow velocity is influenced by L^*, B^* and ν_{h}^*. The patch length has no influence on the model outcome as expected; there is no change in roughness in the downstream direction, i.e. $\alpha = 0$. The influence of the eddy viscosity has been described extensively but the influence of the width is also of interest.

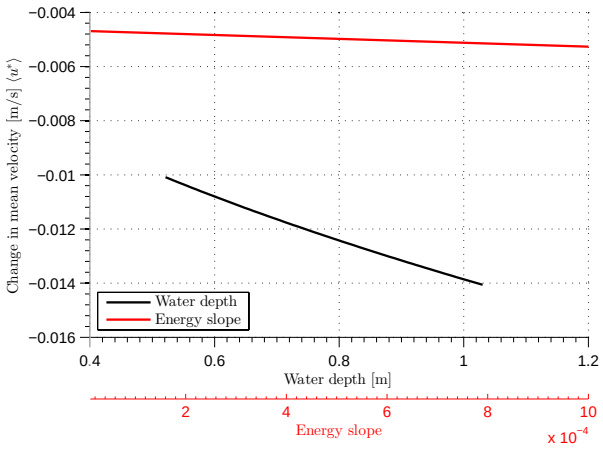

Figure 5.3: *Change in the mean velocity as caused by a change in H^* and i_0 for parallel roughness patches. Both parameters directly influence the velocity scale and it can be concluded that when the velocity scale of the system increases, so does the aggregated resistance.*

As B^* increases, the gradient $\partial u_1/\partial y$ decreases allowing flow to adapt to the roughness variation more gradually. Effectively, when the width is changed, similar processes occur as previously described for the influence of n on the flow velocity regarding the eddy viscosity. Increasing n, reduces B and vice versa. Therefore the width of the channel will have an influence on the relationship between n and ν_{h}^* as seen in figure 5.2. A higher width of the channel will lead to a lower resistance when n and ν_{h}^* are kept constant.

5.1.1 Summary

In summary this section has pointed out some interesting results regarding a transverse structure of roughness patches. The following points have been identified:

- When concerning parallel roughness a resistance increase is always found independent of the roughness layout in comparison to the mean roughness.
- Shear effects are found to cause an increased flow resistance up to a certain maximum. This maximum occurs when different shear layers overlap.
- The influence of the shear effects depends on the eddy viscosity and how gradual the roughness change is. A smooth transition, n is large or B^* is small, or a low eddy viscosity reduce the shear effects and thus the overall roughness increase.

5.2 Serial roughness patches

Serial roughness can be described by setting the complex coefficient $C_{10} = \frac{1}{2}$ while setting all other values for $C_{mn} = 0$. Utilizing equation (3.5) it can be

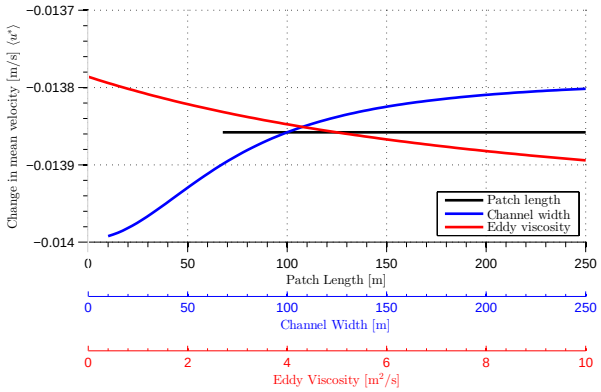

Figure 5.4: *Change in the mean velocity as caused by a change in L^*, B^* and ν_h^* for parallel roughness patches. The ranges of the values are shown in the legend of the figure. The patch length has no influence on the mean velocity in the channel as expected; there is no variation in roughness along x.*

concluded that the spatially varying roughness is defined using:

$$\mu_1(x, y) = \frac{1}{2}\exp(i\alpha x)\cos(0) + \text{c.c.} = \cos(\alpha x).$$

Figure 5.5(a) visualizes the roughness pattern that this function describes. Note that the roughness transition in the downstream direction is very gradual using this roughness description. Utilizing equation (3.17) the solution can easily be found for the spatially averaged contribution in the second order. This function then reduces to:

$$\langle u_2 \rangle = \frac{\alpha^2 F^2}{8\mu_0 |D|^2}(\overbrace{4\mu_0 F^2 |X_1|^2}^{\mu_0(u_1 - F^2\zeta_1)^2} + \overbrace{3\Re\{D\}}^{\mu_1(2u_1 - F^2\zeta_1)}), \tag{5.3}$$

where D is the complex determinant defined in equation (3.11) and $X_1 = i\alpha + \nu\alpha^2 + \mu_0$. Similarly to the parallel patterns it can be seen that the transverse velocity $v_1 = 0$ as found in equation (3.10) remains zero as the patches do not have a transverse and streamline structure. This again leads to the fact that the contributions arising from this velocity are trivial, i.e. $v_1 \frac{\partial u_1}{\partial y} = 0$ and $0.5\mu_0 v_1^2 = 0$.

However, the free surface elevation does not remain trivial for serial roughness patches. This causes backwater effects to occur. Momentum and mass are only driven by the change in free surface elevation and the downstream velocity gradient determined in the first order. The eddy viscosity is set to zero analogous to the parallel roughness pattern. This leads to the following solution for the spatially averaged flow velocity contribution in the second order:

$$\langle u_2 \rangle = -\frac{F^2}{4|D|^2}\left[2F^2\mu_0^2 + 10\alpha^2 F^2 + 3\alpha^2\right], \tag{5.4}$$

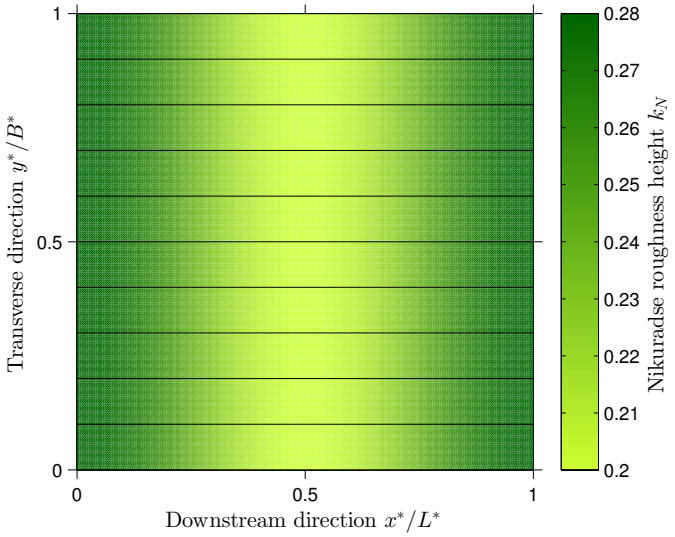

(a)

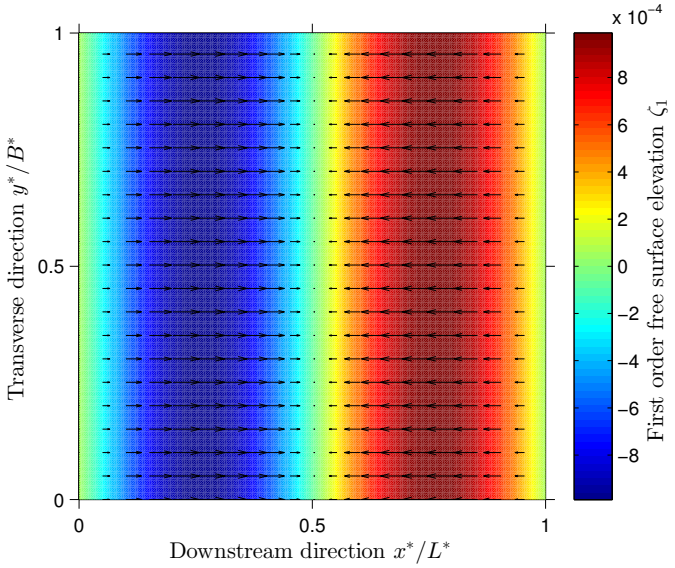

(b)

Figure 5.5: *Surface plot of the vegetation pattern* (a) *and the first order free surface elevation* (b)*. The roughness pattern is described by the mode* $C_{10} = 1/2$*.* $k_{N,b} = 0.20$ *and* $k_{N,p} = 0.28$*. The axes show a scaled length scale as the patch stretches in the streamwise and transverse direction depending on the input for* L^* *and* B^**. The lines in the top figure are the streamlines of the flow up to the first order, the vectors in the bottom plot show the first order velocities* (u_1, v_1)*. The bottom figure clearly shows a negative lag in the free surface elevation where the water level increases before a roughness patch. This is typical for low Froude numbers.*

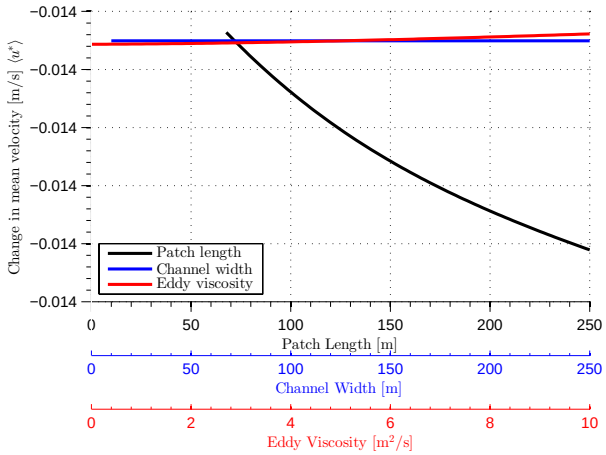

Figure 5.6: *This figure shows the effect of variations in L^*, B^* and ν_h^* on the flow velocity in the channel for serially oriented roughness. Note that the channel width has no influence on the flow velocity as expected (there are no transverse variations in roughness). The eddy viscosity has a very small and opposite effect in a streamwise roughness patch structure when compared to a transverse roughness patch structure. When the flow becomes more viscous, i.e. when more turbulence is accounted for, less resistance occurs.*

where $|D|^2 = (\alpha^2 + \mu_0^2)(9F^4\mu_0^2 - 2\alpha^2F^2 + \alpha^2F^4 + \alpha^2)$. Note that for serial patches, unlike parallel patches, reducing the eddy viscosity to zero does not cause the influence of the spatial structure of the patches given by α to become trivial. This is caused by the fact that the backwater effects as given by $F^2\zeta_1$ become dominant for serial patches and not the eddy viscosity. The backwater effects are clear visualized in figure 5.5(b).

In figure 5.5 it can be seen that the first order velocity change in the downstream direction is a direct result of the roughness description. The system accelerates over the base friction and decelerates at the roughness peaks. As there is no change in roughness along the width of the river, no change in velocity will be found in this direction (i.e. $v_1 = 0$). It can therefore be seen that the width of the river also has no influence on the spatially averaged velocity. Figure 5.6 shows this effect.

From equation (5.3) it can be seen that the spatially averaged change in the flow velocity is proportional to the Froude number of the system. This also emphasizes that the aggregate roughness is defined in its entirety by the backwater effects that arise due to the downstream roughness variations.

Figure 5.6 shows how the patch length, channel width and eddy viscosity influence the mean flow velocity. Note that the scale of the variations is particularly small. The width of the channel has no influence on the aggregate roughness and the influence of the eddy viscosity also appears to be negligible (no shearing occurs). It appears that increasing the patch length also increases the aggregate roughness. This can be explained by the fact that the backwater effects can develop more fully when the length scale is increased.

5.2.1 Summary

This section investigated patches with a streamwise structure. The most interesting findings are:

- The aggregate resistance found for patches with a streamwise structure is caused entirely by backwater effects. Equation (5.3) shows this because a rigid lid (i.e. $F^2 = 0$) results in no aggregate roughness.

- Longer patch lengths allow backwater effects to develop causing a higher aggregate resistance.

5.3 Checkerboard roughness patches

The last single mode patch pattern that is to be considered is described by $C_{11} = 1/2$ while all other possible values of $C_{mn} = 0$. This mode describes an alternating pattern of roughness in the transverse and downstream direction, which has been visualized in the top plot of figure 5.7. The spatially varying roughness is then given by:

$$\mu_1 = \frac{1}{2}\exp(i\alpha x)\cos(\beta y) = \cos(\alpha x)\cos(\beta y).$$

Of interest once again is the spatially invariant contribution to the flow in the second order. In this case all four terms contribute to the change in flow velocity in the second order; this is given by:

$$\begin{aligned}\langle u_2\rangle = -\frac{1}{16\mu_0|D|^2}\,[\,&\beta^2F^2\left(X_1+\overline{X_1}\right)+2\mu_0\left(4F^4|X_1|^2-3\beta^2F^2+\beta^4\right)\\&+\mu_0\beta^2+\left(3F^2-2\beta^2\right)\left(D+\overline{D}\right)\,]\,.\end{aligned}\tag{5.5}$$

The additional terms that contribute to the spatially averaged flow velocity are the lateral distribution of longitudinal momentum and the resistance to the flow in the transverse direction. Both terms enter the analysis as they require a transverse velocity in the first order, which only arises when the roughness varies in the streamwise and transverse direction. This can be seen directly in equation (3.10), where $V_{1,mn} \neq 0$ requires both α and β to be nontrivial.

Figure 5.7 shows various effects observed in the previous two cases combined in a single patch, which is expected considering the patch definition. The free surface elevation ζ_1 observes a similar negative lag as in the serial roughness case. The changing direction of u_1 from the serial patch pattern is combined with the transverse structure of u_1 as found for the parallel patch pattern.

New, however, is the generation of a transverse flow velocity component v_1, which leads to flow routing as visualized by the streamlines in figure 5.7(a). The combined effect of the new u_1 structure and the additional transverse velocity v_1 leads to larger scale flow redirection from rough terrain to smooth terrain.

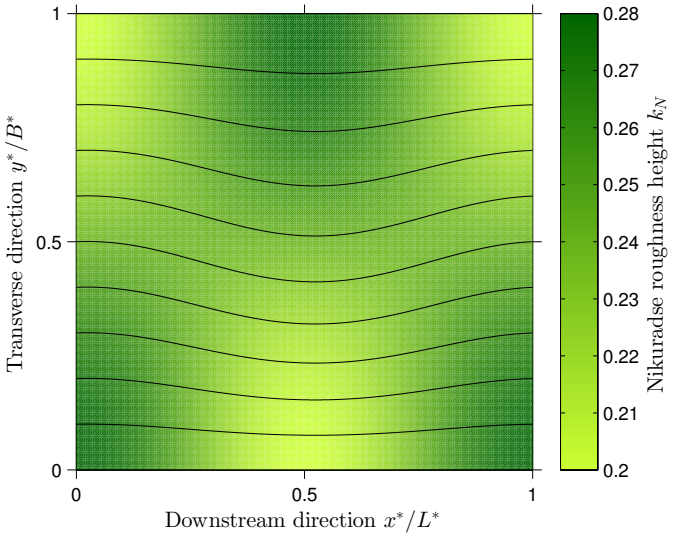

(a)

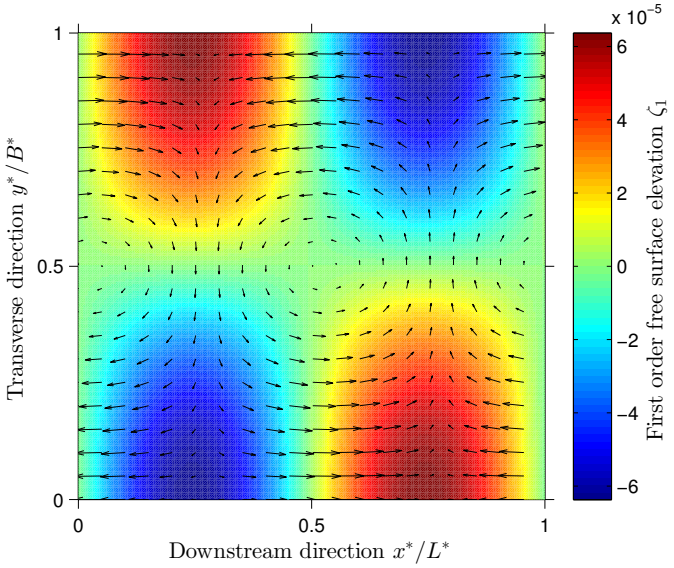

(b)

Figure 5.7: *Surface plot of the vegetation pattern* (a) *and the first order free surface elevation* (b)*. The roughness pattern is described by the mode* $C_{11} = 1/2$*.* $k_{N,b} = 0.20$ *and* $k_{N,p} = 0.28$*. The axes show a scaled length scale as the patch stretches in the streamwise and transverse direction depending on the input for* L^* *and* B^**. The lines in the top figure are slightly exaggerated streamlines of the flow up to the first order where the vertical component of the flow has been enlarged, the vectors in the bottom plot show the first order velocities* (u_1, v_1)*. The streamlines and velocity vectors show flow routing over the lowest resistance.*

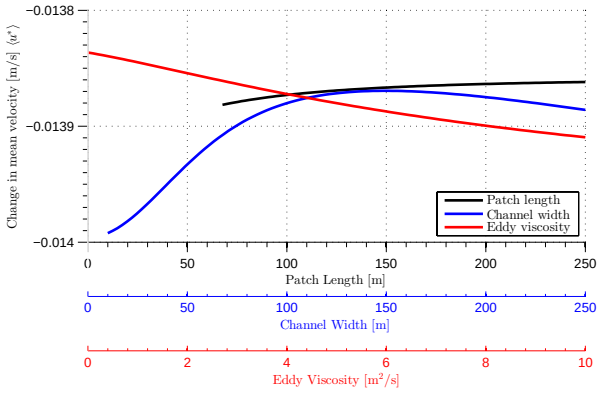

Figure 5.8: *Change in the mean velocity in the system as caused by a change in* L^*, B^* *and* ν_h^* *for the checkerboard roughness patches. The alternate patterns cause both the patch length and the channel width to influence the mean flow velocity in the channel.*

The influence of H^* and i_0 is, similarly to the previous two cases, much larger than the influence of L^*, B^* and ν_{h}^* and also shows exactly the same behaviour. Figure 5.8 shows the model results for these last three system parameters. A particularly interesting observation is that the effect of the channel width has a certain optimum for which the spatially averaged downstream flow velocity is at a minimum. Also, the patch length shows to have a much smaller influence than both the width and the eddy viscosity on calculation results.

The most interesting observation herein is the fact that there is a channel width for which the aggregate roughness is lowest. It is to be expected that this is caused by a competition between two processes: the shear effects as a result of the transverse roughness variation and the backwater effects as caused by the streamwise roughness variation. When the patches become sufficiently wide, the shearing effects are reduced as flow can adapt more easily. In effect it can 'follow' the roughness pattern easier. At a certain point however the shear effect becomes so small that the existing backwater effects start to play a more dominant role.

Figure 5.9 shows the values of the four contributing terms for different values of B^* and ν_{h}^*. Note that the additional terms that were not present in the serial and parallel cases (i.e. figure 5.9 (a) and (c)) have a much smaller contribution to the spatially averaged flow velocity in the second order. However, the behaviour shown by these two terms is significantly different. The eddy viscosity has a much smaller effect. The figure also shows that the two larger terms, shown in figure 5.9 (b) and (d), have opposing effects but show similar behaviour with respect to the two input parameters. From this figure it can be seen that the optimum channel width, where resistance is lowest, appears to be dependent upon the eddy viscosity value as the optimal point scales accordingly.

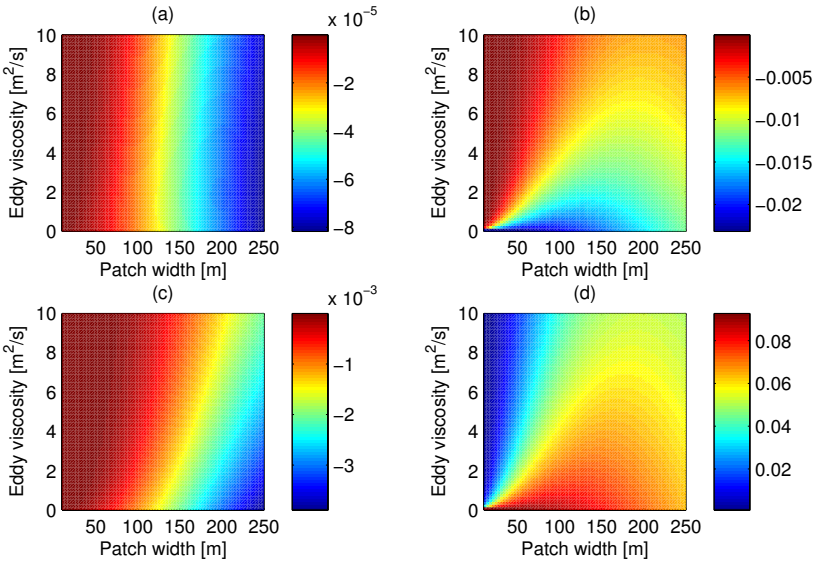

Figure 5.9: *Influence of each of the four terms in the solution given by equation* (5.5) *where* (a) *is* $v_1 \frac{\partial u_1}{\partial y}$ (b) *is* $\mu_0 \left(u_1 - F^2 \zeta_1\right)^2$ (c) *is* $\frac{1}{2}\mu_0 v_1^2$ *and* (d) *is* $\mu_1 \left(2u_1 - F^2 \zeta_1\right)$. *Note the large difference in the order of magnitude of the particular contributions to* U_{200} *and specifically that* (d) *displays opposing behaviour. It can also be seen that the optimum value for* B^* *is related to the influence of* ν_h^*.

5.3.1 Summary

In this section the checkerboard patches were analysed. Some interesting findings can be identified:

- A roughness pattern that has both streamwise and transverse roughness variations induces a transverse velocity component. This velocity component results in two additional terms that contribute to the aggregate roughness. These are the transverse redistribution of longitudinal momentum and a resistance in the transverse direction.
- The induced transverse velocity component results in flow routing effectively increasing the channel length, thus causing an increased aggregate resistance.
- An minimum roughness can be found for the checkerboard roughness layout at a certain width. It is expected that this is caused by a competition between the shear and backwater effects.

Chapter 6

Results: Complex patch patterns

The previous chapter discussed how various physical scales influenced the aggregated roughness of a patch pattern on a floodplain. Up to this points the patches discussed have been simple, consisting of only one mode in the Fourier space. This chapter discusses more complex patch patterns, and how they are influenced by the same input variables with the addition of rotation.

This chapter first explains how the complex coefficients C_{mn} are obtained for more complex patches, allowing almost any shape to be investigated. Then a similar analysis will be performed as seen in the previous chapter. The relative importance of five input variables with the addition of rotation are discussed.

6.1 Obtaining roughness patch coefficients

This section discusses the method used to find the complex coefficients C_{mn} that define the roughness patch. The two dimensional fast Fourier Transform algorithm in MATLAB is used to transform bitmap image information into Fourier coefficients. This allows the greatest freedom in defining the roughness coefficients as they can literally be drawn any shape fathomable.

6.1.1 Input image

The patterns for which the analysis is performed are shown in figure 6.1. The image shows a black background with the roughness patches added in white. These patch shapes were chosen because the elongated shape of the patch leads to the greatest differences in roughness as caused by the various input parameters. Roughness patches that had a more even aspect ratio lead to results closer to the averaged roughness value, meaning that spatial characteristics barely influenced the results. This can be observed in the results for the patch described by figure 6.1(c).

Using images as input for the roughness patches has the additional benefit that a patch can be rotated (in a counterclockwise direction) using the image processing tools in MATLAB. There is however one limitation to this method that must be considered. Not the whole input image is available for roughness

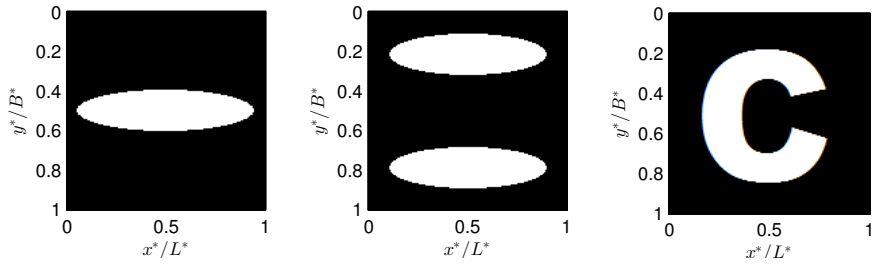

(a) (b) (c)

Figure 6.1: *The three complex patch patterns that are analyzed are shown in this section.* (a) *shows a rounded longitudinal roughness patch with a streamwise orientation at 0 degrees rotation.* (b) *two rounded rectangular roughness patches next to each other at 0 degrees rotation and* (c) *shows a patch in the shape of the letter C. In these images black represents the background vegetation and white shows the roughness patches.*

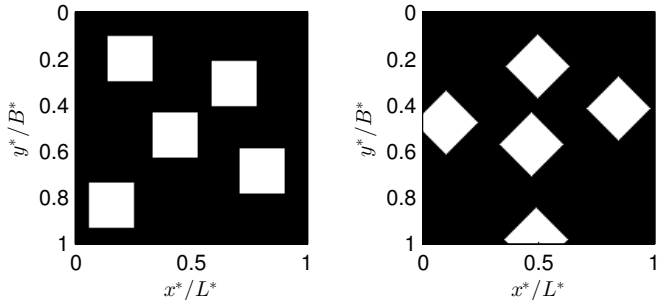

Figure 6.2: *This illustration shows that not all patch patterns can be rotated due to the fact that the image is cropped at rotation. A final patch to be considered are the random roughness patches as also modelled by van Velzen et al. (2003a) and ter Haar (2010). In this case, the testpattern shown in figure 6.1(c) has been rotated by 45 degrees, but some information is lost at the edges.*

patches as the rotation in MATLAB crops the image so that an image of the same size is returned. Figure 6.2 shows an example of a rotation that will not result in usable model results. The complex patch pattern shown in figure 6.2(a) cannot be rotated as some information is lost at the edges due to the cropping effect of the rotation function. As a result, patches may only be placed in the largest circle that fits inside the input image when the patch needs to be rotated.

6.1.2 Fast Fourier Transform

The complex coefficients C_{mn} are found using the fast Fourier transform algorithm in MATLAB. This discrete Fourier transform uses a frequency filter to identify what frequencies can be found in the patch and with what amplitudes. The coefficients describe the input image better as the number of modes considered increases. However a greater number of modes also significantly increases calculation time of the model. It was found that using 20 modes in both m and

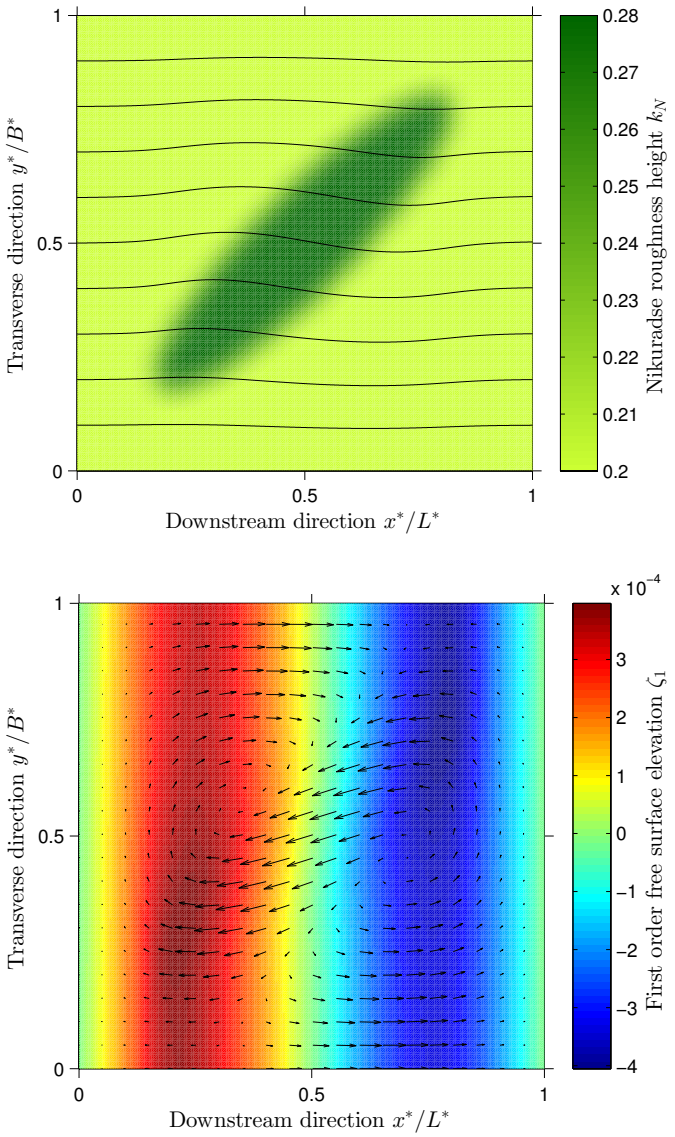

Figure 6.3: *Surface plot of the vegetation pattern* (a) *and the first order free surface elevation* (b) *for the rounded elongated roughness patch without rotation.*

n satisfactorily describes the patches.

A common problem using Fourier transformations is the Gibbs phenomenon, which occurs at discontinuous points in the input data. The Fourier transformation (over)compensates for this discontinuity through the superposition of many frequencies at the place of discontinuity. As a result the transformation overestimates the function at both sides of the discontinuity, which leads to erratic peaks in the function. For this analysis a Gaussian filter is placed over the input image in order to smooth the input patch before the Fourier transformation is performed.

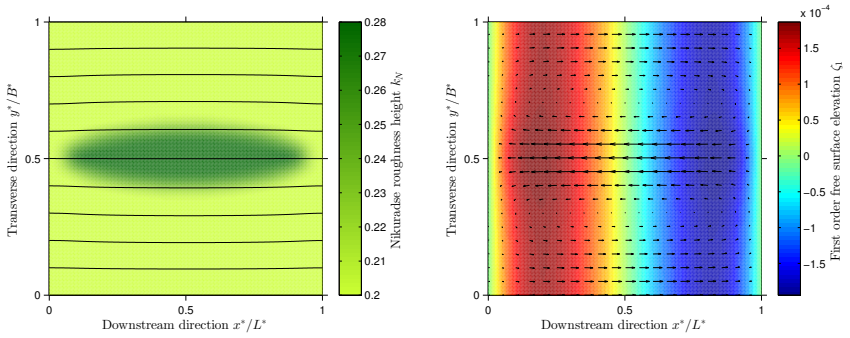

(a) (b)

Figure 6.4: *Surface plot of the vegetation pattern* (a) *and the first order free surface elevation* (b) *for the rounded elongated roughness patch without rotation.*

6.2 Input parameter values

The same input parameter values will be used as with the simple patch descriptions with the exception of the fixed water depth and the range of the patch length. These changes are caused by the limitations of the solution method. A water depth of 0.8 meters will be used and the length of the roughness patch pattern will be varied from 60 to 250. Furthermore, the rotation of patches occurs in the counter-clockwise direction and will range between $0 \leq$ rotation ≤ 180 degrees.

6.3 Influence of patch rotation

In order to investigate the relative importance of patch orientation with regards to the aggregated roughness, model calculations have been performed for two complex patches that allow rotation. The roughness patches used for this analysis are illustrated in Figure 6.1. When there is no rotation the patches are oriented in the streamwise direction. Rotating the patch by 90 degrees causes them to be perpendicular to the flow.

6.3.1 Rounded elongated patch

The first patch considered in this analysis is the patch shown in figure 6.1(a), an elongated rounded patch. The first order solution has been visualized for three points of the rotation of the rounded elongated patch. These are: 0 degrees rotation 6.4, 45 degrees rotation 6.3 and 90 degrees rotation 6.5. It can be seen that the flow travels the route of least resistance where possible, similarly to the case with the alternating roughness patch in the previous channel. The streamlines in all three cases attempt to 'evade' the roughness patch, but the flow also bends towards the shortest path over the roughness patch. This is especially clear in figure 6.3.

As expected, all three components of the solution $\phi_1 = (u_1, v_1, \zeta_1)$ are found in the complex patch pattern solution, which indicates that all four contributing terms in equation (3.16) are non-trivial. Figure 6.6 shows the results of the

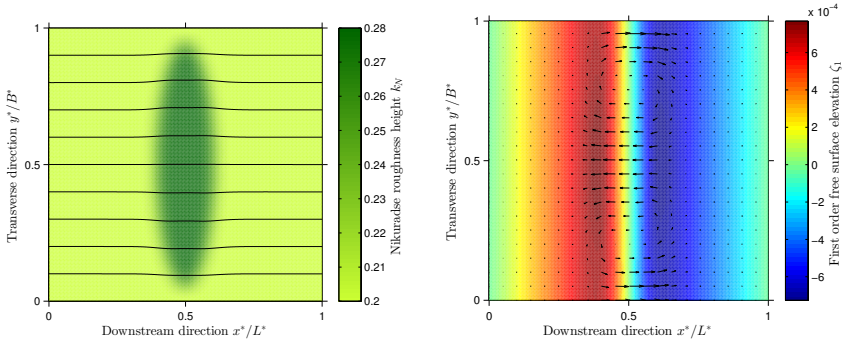

Figure 6.5: *Surface plot of the vegetation pattern* (a) *and the first order free surface elevation* (b) *for the rounded elongated roughness patch after 90 degrees rotation.*

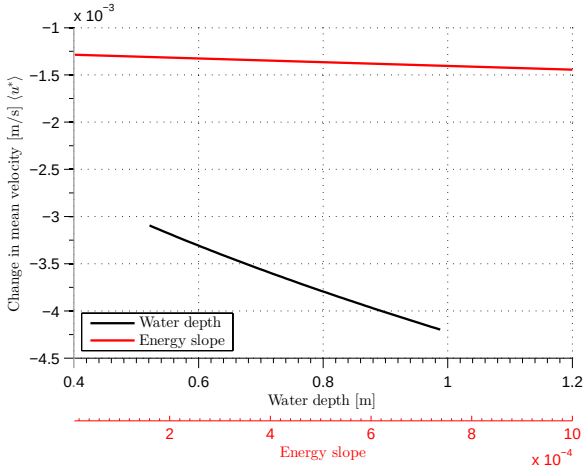

Figure 6.6: *Influence of H^* and i_0 on the change in the mean flow velocity in the river section.*

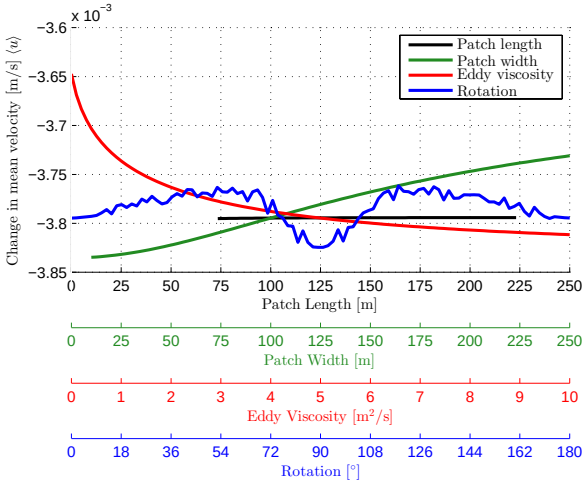

Figure 6.7: *Influence of L^*, B^*, ν_h^* and rotation on the mean flow velocity in the river section. The results clearly shows how the rotation of the elongated patch induces the most resistance when perpendicular to the flow, but not the least when oriented in the streamwise direction. The minimum resistance can be found visually around 54 degrees of rotation.*

model calculations for the water depth and the energy slope. The results are comparable to the simple patch pattern descriptions with respect to the trend observed, as well as the difference in magnitude.

Figure 6.7 shows model results for the remaining system parameters: $L^*, B^*, \nu_{\mathrm{h}}^*$ and rotation. The trends observed are very similar to those found for the simple alternating patch pattern with a few exceptions. The length of the patch appears to have negligible influence on the model output. This can be explained by the fact the model results are presented for the 0 degree rotation case, effectively describing a parallel patch pattern, which were also not influenced in the simple case. Secondly, there is no obvious optimal patch width for which the resistance is lowest.

The influence of the eddy viscosity is the same as in the previous model calculations. When the eddy viscosity of the flow increases a larger resistance is found. This is as expected because at higher eddy viscosities more energy is lost to the small scale vorticity in the flow.

Of particular interest however is the inclusion of patch rotation, which shows some interesting results. The largest resistance is observed where the patch pattern is rotated 90 degrees as expected. This describes a roughness patch perpendicular to the flow field, reducing the flow velocity along the entire width of the river. What is interesting however is that the point of least resistance is does not occur where the patch is oriented in a stream wise direction, but rather at an angle of approximately 54 degrees rotation. This will also be observed for the other rotation cased discussed hereafter.

The cause of this influence of the patch orientation is unknown and will require investigation. However, it is expected that it is caused by a competition between the backwater effects and the shear effects. From the previous chapter

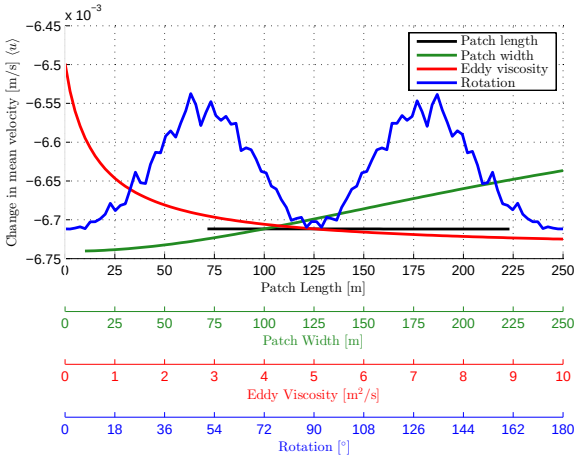

Figure 6.8: *Influence of L^*, B^*, ν_h^* and rotation on the mean flow velocity in the river section with two side by side patches. Interestingly, the change in mean velocity is almost the same when the patch pattern is placed perpendicular or streamwise to the flow. Similarly to the single patch case, the lowest amount of resistance is observed where the patch is rotated at approximately 50 degrees.*

it is known that the influence of backwater effects are larger for patches oriented perpendicular to the flow. As a result it is expected that a transverse or serial orientation of the roughness patches will cause the greatest backwater effects. Additionally it is known that a parallel patch orientation leads to shear effects that cause increased roughness.

The influence of patch orientation is therefore expected to be the result of a combined minimum contribution by both shear effects and backwater effects, which in this case is found around 54° rotation. Rotating it towards a parallel orientation will increase shear effects and decrease backwater effects but the combined effects will be larger than at the obtained 'optimum'.

6.3.2 Side by side patches

Figure 6.8 shows the results for model calculations where the patch as seen in figure 6.1(b) is considered. The model results agree with earlier calculations and show similar trends for all four model parameters considered. Of interest once again are the model results regarding the patch pattern rotation. In this case the model results show that the highest flow velocity reduction is attained when the patch is either perpendicular or streamwise to the flow. The lowest resistance is again observed at a rotation of approximately 50 degrees.

This is most likely the result of the fact that u_1 is much larger than v_1 using this solution technique. In the first order solutions it can be seen that the change in velocity in the downstream direction is much larger than in the transverse direction. A streamwise oriented patch therefore cumulatively reduces the flow velocity in the downstream direction over the entire length of the patch as almost no momentum is transferred in the transverse direction. In this case, where two patches are considered side by side the total flow velocity reduction

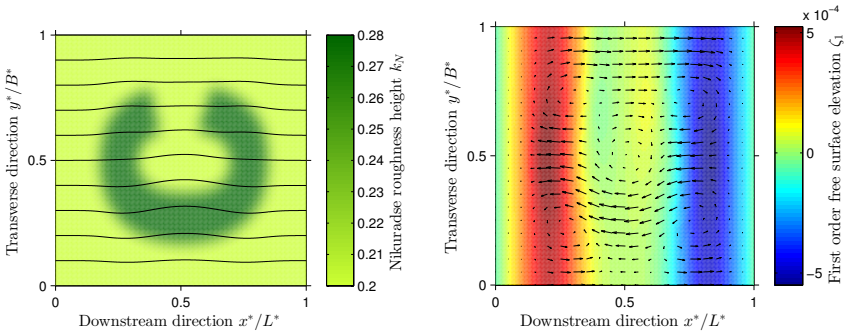

Figure 6.9: *Surface plot of the vegetation pattern* (a) *and the first order free surface elevation* (b) *for the patch with the shape of the letter C when rotated 90 degrees.*

is even larger.

Patches that are oriented at an angle to the flow have a shorter downstream travel distance over the patch, therefore leading to overall lower flow velocity reduction. It is expected that model results for larger roughness variations at smaller scales will not show this behaviour because more momentum is expected to be transferred in the transverse direction.

6.3.3 Patch pattern C

The final patch that is considered that can be rotated is shown in figure 6.1(c). The first order flow field over the patch has been visualized in figure 6.9 for the case where the patch has been rotated by 90°.

Figure 6.10 shows the results for the model calculations for L^*, B^*, ν_h^* and the patch rotation. The trends in the figure correspond to earlier trends observed for different roughness descriptions. Increased patch lengths and increased width reduce the flow velocity change as the flow can adapt more gradually. Of interest once again is the influence of the orientation on the change in velocity. In this case the influence of rotation appears to be minimal. It is expected that this is caused by the fact the the patch shape can be approached as a circle. However, what is unexpected, is the fact that the orientation of the opening of the patch description appears to have barely any influence on the change in velocity.

6.4 Random roughness patches

The last patch pattern for analysis is shown in figure 6.1 (c), which described a random distribution of five roughness patches. This analysis was chosen in order to compare model results to the results obtained by ter Haar (2010) and van Velzen et al. (2003a), who use a similar setup. The first order solution to this case is shown in figure 6.11. The velocity vectors appear where expected; at the location of the roughness patches, and the streamlines follow the path of least resistance analogously to the alternating pattern in the previous chapter. The free surface elevation appears in front of the roughness patches. It is important

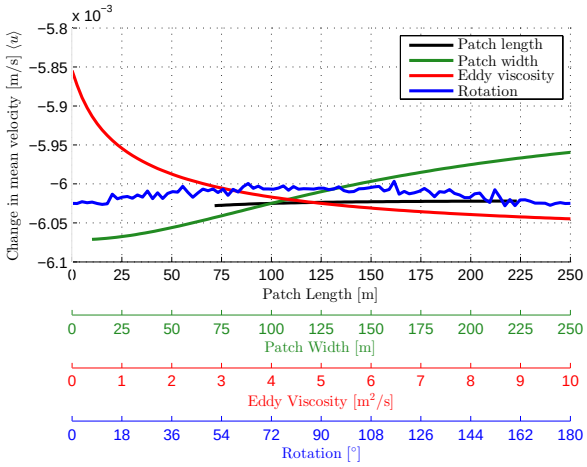

Figure 6.10: *Influence of L^*, B^*, ν_h^* and rotation on the mean flow velocity in the river section with the C shaped patch. It appears that the patch orientation has very little influence on the change in mean velocity. It is expected that this is caused by the fact that the letter C is nearly a circle. The opening appearantly has very little influence on model results.*

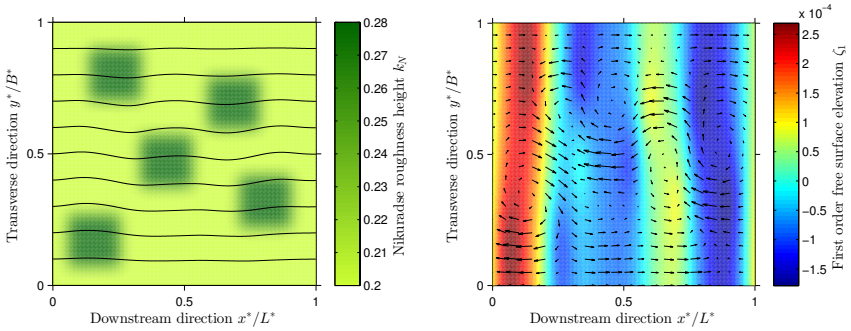

Figure 6.11: *Surface plot of the vegetation pattern* (a) *and the first order free surface elevation* (b) *for the randomly placed patches*

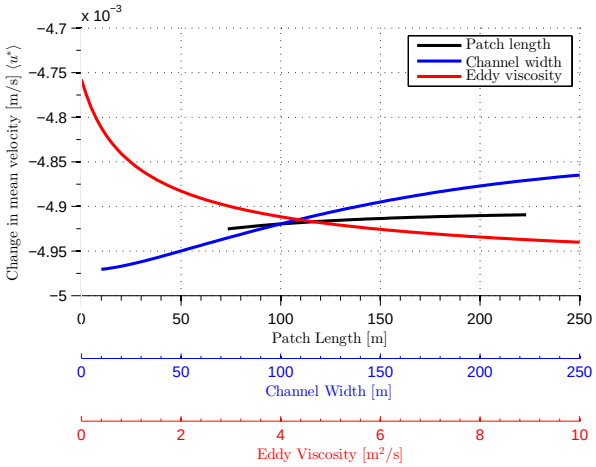

Figure 6.12: *Influence of L^*, B^* and ν_h^* on the mean flow velocity in the river section with randomly placed patches.*

to note however that the free surface elevation appears channel wide, and not localized at the roughness patches.

Figure 6.12 shows the model results for the randomly placed roughness patches. The different model parameters show comparable behaviour to the results found for the alternating simple roughness patch description. Higher values of ν_{h}^* lead to increased flow retardation while larger spatial scales reduce the flow retardation as the flow has more space to adjust.

6.5 Summary

This chapter discusses the influence of the input variables on more complex patch descriptions. Some general conclusions can be drawn from this analysis. In general, similar to the simple patches, the water depth and the energy slope contribute most towards a change in downstream velocity. Increased water depth and slope lead to greater changes in downstream velocity with respect to the undisturbed velocity scale. The cause for this can be found in the scaling itself. As the velocity scale increases, so will the deviations proportionally as these are absolute changes and not relative changes.

Secondly, it can be concluded that increasing the length scale of the system decreases the flow retardation in the river section. Longer spatial scales allow the flow to distribute the momentum redirection over longer distances, reducing the overall impact on the flow velocity. In the third place it can be said that the eddy viscosity influences the flow as expected; higher values of eddy viscosity correspond to a greater amount of energy that is dissipated in the flow itself leading to a lower aggregated downstream flow velocity.

Finally, and most interestingly, is the conclusion that the flow velocity is not reduced least while patches are streamlined with the flow field, but when they are placed at an angle of around 50 degrees, depending on the configuration of the patches used. It is expected that this is caused by a competition between

backwater and shear effects. If this is the true cause has however not been determined and more research is required to investigate this phenomenon.

Chapter 7

Discussion

The previous chapters have outlined an idealized hydrodynamic model which has been used to analyze the influence of various patch characteristics and system parameters on the change in mean flow velocity over a river segment/floodplain. This new mean velocity can then be used to determine the aggregate roughness of such a river segment using equation (2.15). This chapter discusses the model used for the analysis, and the results of the analysis performed in this report.

7.1 Regarding the model

The model shows expected behaviour, albeit at extremely small scales. The permissible ranges of input data cause the variations in the flow to be extremely small. The constraints as discussed in Chapter 4 cause the models application at small length scales to be very limited. At the shortest length scales, with the smallest difference between $k_{N,b}$ and $k_{N,p}$ only a very small range of water depths can be modelled. Similarly, in order to model very large water depths, very large length scales are required. The weakly non-linear analysis does not allow the investigation of patches similar to those researched by ter Haar (2010) or van Velzen et al. (2003a). The limits imposed by the linearization may however be different if the small parameter ϵ is scaled with respect to μ_0 as outlined in chapter 4.

The goal of developing this model was to investigate the influence of vegetative roughness patches on aggregate roughness as found in floodplains. As outlined in the introduction, integrated river management increases the ecological development of floodplains, which is expected to lead to higher water levels during flooding. The differences in roughness discussed in other studies cannot be approached using this modelling analysis due to the limitations of the linearization. Different forms of roughness, however, can be approached using this method. A good example of this would be a river section with different grainsizes and a flat bed. The model allows the identification of various physical processes, i.e. backwater effects and shear effects, that may be difficult to distinguish in more complex models.

7.2 Regarding the patch characteristics analysis

The influence of the length of a vegetation pattern and the width are predicted by the model as expected. Larger length scales cause the change in roughness to be gradual, leading to lower changes in flow velocity. An increased eddy viscosity increases the aggregate roughness as more energy is dissipated in smaller scale vortices, which are accounted for in the eddy viscosity.

Of particular interest is the influence of patch orientation on the aggregate roughness. The maximum resistance as caused by an elongated patch of roughness was found while the roughness was placed perpendicular to the flow field. The minimum resistance, however, was found at an angle of approximately 50 degrees, and not when it is streamlined with the flow. It is expected that this result is caused by the competition between backwater and shear effects around a roughness patch. Model results for the simple patch characteristics show that parallel roughness induces shear effects and serially placed roughness induces backwater effects that both affect flow resistance. The 'optimum' resistance can appearantly be found somewhere in between these two extremes. The processes are however not yet fully understood and will require further investigation.

Model results in general yielded such small values that it must be questioned whether the conclusions drawn using this solution method have any significance when regarding real vegetation patches. The model therefore can be used primarily to investigate general trends regarding the influence of input parameters on certain identifiable physical flow processes. The processes that have been identified are backwater effects, shear effects and the transverse redistribution of longitudinal momentum.

7.3 Compared to current parameterizations

In this section the model results will be compared to the current parameterizations as determined by van Velzen et al. (2003a) and ter Haar (2010). It is of interest to note that both methods distinguish, in their own way, between the patch orientation by describing a ratio between parallel and serially placed roughness.

The parameterization by van Velzen et al. (2003a) does this explicitly by determining how much of the vegetation has a serial orientation and how much has a parallel orientation. It is stated that determining if patch patterns are parallel or serial is rather subjective. The two roughnesses are then weighed using a fixed parameter, which attributes more influence to serial roughness than to parallel roughness. This is comparable to this research where the velocity was reduced more for serial roughness than for parallel roughness. However, this research shows that the serially placed roughness is much less sensitive to changes in spatial scales than parallel patches. The influence of backwater effects is larger on the aggregate resistance than the shear effects, but the shear effects are influenced more by spatial scales.

In the research by ter Haar (2010) a new parameterization was suggested that takes the complex flow processes into account. The fitted model shows the influence of average patch width and average patch length as important parameters for aggregated roughness. Additionally the mixing layers around a patch and the flow adaptation length behind a patch are considered as parameter

input. Two ratios are used in the parameterization, which are: i) the width of the mixing layer compared to the width of the patch and ii) the length of the flow adaptation compared to the length of the patch. These two ratios, in a sense, also describe whether a patch is predominantly oriented serial or parallel to the river flow.

It can be said that in previous research and in this investigation a trend can be observed where the aggregated roughness largely depends on to what extent a patch is oriented serial or parallel to the flow field. It is suggested that this balance is determined by a competition between backwater effects and shear effects. More research is required in order to fully understand the dynamics of this relationship.

Chapter 8

Conclusion

In this final chapter conclusions are drawn by answering the research questions posed in Chapter 1. The conclusions will be used, in combination with the discussion from Chapter 7 to formulate recommendations for future research.

8.1 Research questions

The goal of this research was to improve aggregate roughness parameterization by investigating the importance of various vegetative roughness characteristics. An idealized model was suggested as an alternative to the current modelling applications, which is what most similar studies rely on. The first question aims to answer what such an idealized model should encompass.

How can aggregated roughness for a floodplain section be determined using an idealized model?

The model formulated was based on the steady non-linear depth-averaged shallow water equations, which use an eddy viscosity to close the turbulence problem and allow a spatial variation in roughness. This system of equations was scaled in order to obtain dimensionless parameters that may be used to identify the relative importance of various physical processes.

The equations were solved analytically using a weakly-nonlinear analysis. A small perturbation model was used to approximate three flow properties: the downstream velocity u, the transverse velocity v and the free surface elevtaion ζ. The spatially varying roughness was formulated in terms of small deviations from a mean roughness. A Fourier transformation was performed for both the resistance description and the weakly-nonlinear problem. This allows the problem to be solved using matrix multiplication.

A first order contribution was found and used in the subsequent analysis. In the second order of the approximation, convolutions of the first order solution were found. These convolutions lead to a spatially invariant contribution to the downstream flow velocity in the second order U_{200}. This allows a new average velocity to be calculated, which can be used to determine aggregate roughness while allowing for a spatial variation in roughness.

This solution, in both the first and second order, was used to analyze various roughness patch descriptions. The new idealized modelling approach allows

a quick assessment of the influence of patchy roughness on mean river flow. Dominant mechanisms were found in case of parallel roughness variations only (lateral shear), serial variations only (backwater effects) and combined variations (lateral shear, backwater effects and lateral redistribution of longitudinal momentum).

What is the influence of various patch characteristics on the mean flow over the floodplain section?

A total of eight input parameters was found that influence model results. These were: the water depth, patch length, channel width, eddy viscosity, energy slope, patch rotation, background resistance and the roughness of the patch. First the application limitations of the model were found as caused by the linearization. It was found that the model may only be applied for very small variations in roughness but also that the water depth and patch length place additional restrictions on model applicability.

In general it was found that the water depth and energy slope have the largest influence on the aggregate roughness, as can be explained using the Chézy relationship. Furthermore, it was found that the eddy viscosity significantly influences the resistance caused by transverse variations in the downstream velocity. In general, larger eddy viscosities lead to higher aggregate resistances as more energy is lost to turbulent eddies. Also, it was found that increasing the spatial scales of the floodplain decreases the overall aggregate resistance. It is argued that flow adaptation can occur more gradually at larger spatial scales, causing a lower aggregate resistance.

The influence of patch orientation was also simulated using the idealized model and of particular interest was the result that the aggregate resistance was not lowest at a streamwise orientation, but rather when the patch was oriented diagonally to the flow field.

How can the new insights regarding the characteristics of vegetation patches be incorporated into an aggregated roughness parameterization method?

In general it is very difficult, and possibly unwise, to suggest improvements to current aggregate roughness parametrizations based on the results of this research. The solution technique used does not allow the simulation of scenarios as found on floodplains concerning vegetative roughness. The situations simulated by ter Haar (2010) and van Velzen et al. (2003a) cannot be modelled and therefore it is difficult to even verify modelling results. Similar trends were however observed. The influence of the parallel and serial structure of patches is evident in all roughness parameterizations and is also found in this research.

8.2 Recommendations

Based on this research some recommendations can be made. First and foremost it may be wise to investigate the influence of a different linearization parameter, which is scaled to with the background roughness, to see if model applicability can be increased. If the applicability boundaries are still too restrictive it is suggested to attempt a strongly nonlinear solution method. A strongly non-linear

analysis will most likely result in a semi-numerical model as the problem becomes very complicated to solve analytically. It is however suggested to maintain the idealized modelling approach as this allows the identification of important system parameters and processes.

A second recommendation that can be made is to investigate the influence of patch orientation in greater detail. The model calculations show that there is an optimal angle at which vegetation patches induce the least amount of resistance to the flow as a whole. It is suggested that this outcome is the result of a competition between backwater effects and shear effects as induced by serial and parallel roughness variations respectively. More research is, however, required to understand these dynamics fully.

A final recommendation is that this modelling structure does allow the investigation of small differences in roughness such as found for different grain sizes on a flat river bed. It may be interesting to investigate how model results compare to experiments where the influence of different grainsizes is concerned. An example of such an experiment is for example the research performed by Jesson et al. (2011).

Bibliography

Acheson, D. (1990). *Elementary Fluid Dynamics*. Oxford applied mathematics and computing science series. Oxford: Clarendon Press.

Ballesteros, J. A., Bodoque, J. M., Diez-Herrero, A., Sanchez-Silva, M., and Stoffel, M. (2011). Calibration of floodplain roughness and estimation of flood discharge based on tree-ring evidence and hydraulic modelling. *Journal of Hydrology*, 403(1-2):103–115.

Bridge, J. S. (2003). *Rivers and Floodplains - Forms, Processes and Sedimentary Record*. Blackwell Science.

Davidson, P. (2004). *Turbulence*. Oxford University Press.

EU (2010). European Commission - Environment - Nature & Biodiversity. Website, accessed on 17 January, 2012. http://ec.europa.eu/environment/nature/natura2000/index_en.htm.

Forzieri, G., Degetto, M., Righetti, M., Castelli, F., and Preti, F. (2011). Satellite multispectral data for improved floodplain roughness modelling. *Journal of Hydrology*, 407(1-4):41–57.

Fox, R. W., McDonald, A. T., and Pritchard, P. J. (2004). *Introduction to fluid mechanics*. John Wiley & Sons, Inc., sixth edition.

Huisman, P., Cramer, W., van Ee, G., Hooghart, J., Salz, H., and Zuidema, F. (1998). *Water in the Netherlands*. NHV-Special 3. Delft: Netherlands Hydrological Society (NHV).

Huthoff, F. (2007). *Modelling Hydraulic Resistance of Floodplain Vegetation*. PhD thesis, University of Twente.

Huthoff, F., Augustijn, D. C., and Hulscher, S. J. (2007). Analytical solution of the depth-averaged flow velocity in case of submerged rigid cylindrical vegetation. *Water Resources Research*, 43(6):W06413.

Ichem (1985). Nomenclature for hazard and risk assessment in the process industries. Technical report, Working party of the Engineering Practice Committee Institution of Chemical Engineers.

Jesson, M., Bridgeman, J., and Sterling, M. (2011). Open-Channel Discharge Characteristic and Secondary Flow Development Over a Biotope-Scale Heterogeneous Channel Bed. In *Recent Researches in Hydrology, Geology and Continuum Mechanics*, pages 120–125.

Makaske, B., Maas, G. J., van den Brink, C., and Wolfert, H. P. (2011). The Influence of Floodplain Vegetation Succession on Hydraulic Roughness: Is Ecosystem Rehabilitation in Dutch Embanked Floodplains Compatible with Flood Safety Standards? *AMBIO*, 40(4):370–376.

Pope, S. B. (2000). *Turbulent Flows*. Cambridge University Press.

Roos, P. C. (2011). The influence of patchy roughness on mean channel flow. Project outline, University of Twente.

RVR (2010). Hoe lossen we dit op? Website, accessed on 19 January, 2012. http://www.ruimtevoorderivier.nl/.

RWS (2006). Spatial planning key decision room for the river. Pkb, Ruimte voor de Rivier.

RWS (2007). Ecotopenkaterting rijntakken-oost 2005 - biologische monitoring zoete rijkswateren. Technical report, Ministry of Infrastructure and the Environment.

ter Haar, M. (2010). A new method to predict the aggregate roughness of vegetation patterns on floodplains. Master thesis, University of Twente.

van Velzen, E., Jesse, P., Cornelissen, P., and Coops, H. (2003a). Stromingsweerstand vegetatie in uiterwaarden: Deel 1 handboek versie 1. Guidelines, RIZA.

van Velzen, E., Jesse, P., Cornelissen, P., and Coops, H. (2003b). Stromingsweerstand vegetatie in uiterwaarden: Deel 2 achtergronddocument versie 1. Background documentation, RIZA.

van Velzen, E. and Klaassen, G. (1999). Verspreide en aaneengesloten gebieden met begroeiing. Studie naar het effect van begoeiingspatronen. Working paper 99.193x, RIZA.

Werner, M., Hunter, N., and Bates, P. (2005). Identifiability of distributed floodplain roughness values in flood extent estimation. *Journal of Hydrology*, 314(1-4):139–157.

Wesselink, A. J. (2007). Flood safety in the netherlands: The dutch response to hurricane katrina. *Technology in Society*, 29(2):239 – 247.

Appendix A

Notation

The following variables were used in this research

Roman

$\mathbf{A}$	Linear operator in the eigenfunction projection
$\mathcal{A}$	Second order forcing arising from advection
B	Dimensionless channel width
B^*	Dimensional channel width
$\boldsymbol{b}$	Forcing of the system
C_{mn}	Dimensionless complex amplitude of roughness in eigenfunction projection
C^*	Chézy coefficient
c.c.	Complex conjugate
c_{D}	Drag coefficient
c_{D0}	Reference drag coefficient
$c_{\mathrm{D,b}}$	Background drag coefficient
$c_{\mathrm{D,eff}}$	Effective drag coefficient
$c_{\mathrm{D,p}}$	Patch drag coefficient
D_{mn}	Determinant of the solution matrix
$\boldsymbol{e}_x$	Unit vector in the x direction
F	Froude number
$\mathcal{N}^*$	Additional forcing on the system
g^*	Acceleration due to gravity
H^*	Mean water depth
h^*	Water depth
i_0	Energy slope
k_{N}	Nikuradse roughness height
$k_{\mathrm{N,b}}$	Nikuradse roughness height of the background
$k_{\mathrm{N,p}}$	Nikuradse roughness height of the patch
L^*	Typical length of vegetation patch roughness
$\mathcal{L}$	Linear operator
$\mathcal{M}$	Second order forcing of the mass balance
p^*	Pressure
$\mathcal{R}$	Second order forcing arising from resistance
$\mathcal{S}$	Forcing in the eigenfunction projection

$U_{\#,mn}$	Dimensionless complex amplitude of the streamwise velocity in the eigenfunction projection
U^*	Velocity scale
$\vec{u}$	Dimensionless velocity vector of u and v
$\vec{u}^*$	Velocity vector of u^* and v^*
u	Scaled downstream velocity of the flow
u^*	Downstream velocity of the flow
$V_{\#,mn}$	Dimensionless complex amplitude of the transverse velocity in the eigenfunction projection
v	Scaled transverse velocity of the flow
v^*	Transverse velocity of the flow
$\vec{x}$	Directional vector of x and y
$\vec{x}^*$	Directional vector of x^* and y^*
x	Scaled streamwise coordinate
x^*	Streamwise coordinate
y	Scaled transverse coordinate
y^*	Transverse coordinate
$Z_{\#,mn}$	Dimensionless complex amplitude of the free surface elevation
Z^*	Elevation scale

Greek

α_m	Dimensionless streamwise wave number
β_n	Dimensionless transverse wave number
ϵ	Linearization parameter
ζ	Dimensionless free surface elevation
ζ^*	Free surface elevation
μ	Dimensionless friction parameter
μ_0	Reference value of the scaled roughness
μ_1	Spatial variation in the scaled roughness
μ_b	Scaled roughness of background vegetation
μ_p	Scaled roughness of patch vegetation
ν	Scaled dimensionless horizontal eddy viscosity
ν_h^*	Horizontal eddy viscosity
ρ^*	Density of water
τ_b^*	Bottom shear stress
$\Phi_{\#,mn}$	Complex amplitudes of the eigenfunction projection of the solution
$\phi_\#$	Symbolic representation of the solution (u, v, ζ)

Sub - / Super script

$*$	Denotes the quantity is dimensional
$\#$	The order of the affixed term
m	Streamwise mode number
n	Transverse mode number

Appendix B

Hydrodynamic modelling approaches

Some adaptations of the Navier-Stokes equations will be discussed ordered by decreasing computational cost:

Direct Numerical Simulation (DNS) consists of solving the Navier-Stokes equations for all scales of motion numerically. This method was computationally infeasible until the 1970s due to the limitations of computers at the time. It provides the most accurate results and is conceptually the easiest to understand, but the computational costs restrict the methods applicability. The computational costs increase with Reynolds number cubed[a], and thus the more turbulent a flow is, the less applicable this method becomes (Pope, 2000). This is due to the fact that increasing turbulence requires a smaller spatial and temporal scale, increasing the calculation time.

Large Eddy Simulation (LES) computes only the large-scale eddies in a flow explicitly and uses simplified turbulence models to model the smaller scale eddies. It was stated that DNS has as a primary limitation that most of the computational time is spent on the smallest turbulent effects, a scale that LES avoids. As a result LES can be applied to a larger number of situations; it is especially useful in flows over bluff bodies[b], which involve unsteady flow separation and vortex shedding. Pope (2000) describes four conceptual steps to LES:

1. A *filtering* operation is performed where the velocity is decomposed into a sum of the resolved components and the residual components. Herein the residual components are the smaller scale velocities that are not calculated explicitly. The resolved (or filtered) component is

[a]The Reynolds number Re is defined by $Re = \frac{U^* d^*}{\nu^*}$ where U^* is a compartment-averaged streamwise flow velocity, d^* is the diameter of a pipe as used by Osborne Reynolds in his experiments and ν^* is the kinematic viscosity, which is defined as μ^*/ρ^*. The Reynolds number gives an indication of the relative importance of viscous and inertial forces (Huthoff, 2007).

[b]A body having a broad flattened front, the opposite of streamlined

three-dimensional and time-dependent and represents the motion of the large eddies.

2. The filtered component of the flow is determined explicitly using the Navier-Stokes equations. The standard form of the equations is used and a residual stress tensor accounts for the influence of the smaller scale eddies.
3. The residual stress tensor is modelled, most frequently using an eddy viscosity, to obtain closure.
4. The large-scale turbulent flows are approximated by calculating the filtered velocity field numerically. This leads to only one realization of the turbulent flow, which is approximate as the direct influence of the smaller scale turbulence effects has not been accounted for explicitly.

Reynolds Averaged Navier Stokes (RANS) equations were originally introduced when Osborne Reynolds decided to decompose the velocity field into a mean flow and fluctuations from this mean. After time averaging the following Reynolds averaged Navier-Stokes relationship arose for the flow, incorporating turbulence (e.g. Pope (2000); Huthoff (2007)):

$$\frac{\partial u_i}{\partial t} + u_j \frac{\partial u_i}{\partial x_j} = -\frac{1}{\rho}\frac{\partial p}{\partial x_i} + \frac{F_i}{\rho} + \frac{\partial}{\partial x_j}\left(\nu \frac{\partial u_i}{\partial x_j} - \overline{u_i' u_j'}\right)$$

where u_i is the time averaged velocity component in direction $i = x, y$ or z, x_i is the spatial coordinate of this directions, ν is the kinematic viscosity and $\overline{u_i' u_j'}$ are Reynolds stresses. These stresses are not a stress in the conventional sense of the word but they represent momentum fluxes induced by the turbulence and are used to describe the interaction between turbulence itself and the mean flow (Davidson, 2004).

The Reynolds stresses are generally described through the relationship between statistical properties in $\boldsymbol{u}^*$, but the system is not closed. No matter how many mathematical operations are performed, no solution can be found to describe these Reynolds stresses. This is generally referred to as the closure problem of turbulence and is caused by the non-linear advective term in the Navier-Stokes equations. Therefore an assumption about the structure of turbulence is required for the system to be solved (Davidson, 2004).

A common assumption herein is that of the eddy viscosity where the Reynolds Stresses are combined with the stresses caused by the fluids kinematic viscosity. This was originally proposed by Boussinesq in the 1870s. It is important to note that the eddy viscosity is a property of the flow and not the fluid, allowing it to vary spatially and temporally. The eddy viscosity is however often regarded as constant, allowing the RANS equations to be written as:

$$\frac{\partial \vec{u}^*}{\partial t^*} + \vec{u}^* \cdot \nabla^* \vec{u}^* = -\frac{1}{\rho^*}\nabla^* p^* + \nabla^* \cdot \left(\nu^*_{\text{eddy}} \nabla^* \vec{u}^*\right) + \mathcal{F}^*$$

where ν_{eddy} is the eddy viscosity and the kinematic viscosity combined.

Two Dimensional Approaches consider only two spatial dimensions and can be classified into two distinct categories: 2D horizontal (2DH) and 2D vertical (2DV). In the first case the depth averaged flow velocity is considered eliminating the depth scale from the calculations. This can be especially useful when the vertical component of the flow is considered much smaller than the horizontal components of flow. WAQUA, as used by ter Haar (2010) is an example of a 2DH model. On the other hand, 2DV models are commonly used to describe the vertical velocity profile of a flow. Huthoff et al. (2007) uses a 2DV model to determine the depth-averaged flow over submerged vegetation.

One Dimensional Approaches consider only one spatial dimension. The Saint-Venant equations are a good example of 1D flow and are given by:

$$\frac{\partial U}{\partial t} + U\frac{\partial U}{\partial x} = -g\frac{\partial h}{\partial x} + gi_b - gS \tag{B.1}$$

where U is the depth averaged flow velocity, t is time, x is the downstream direction, i_b is the bed inclination and S is the friction slope as introduced by Saint-Venant. The modelling software SOBEK is an example of a 1D model.

0D Approach or lumped approach does not consider spatial scales and may be applied for example when flow may be considered spatially uniform.

Appendix C

Scaling operations

In this appendix the scaled form of the flow equations are derived.

C.1 Mass balance

The mass balance as given by equation (2.5) can also be written as:

$$\frac{\partial}{\partial x^*}\left[\left(H^* + \zeta^*\right) u^*\right] + \frac{\partial}{\partial y^*}\left[\left(H^* + \zeta^*\right) v^*\right] = 0$$

By substituting in the relations as defined by equation (2.9) the following is obtained:

$$\frac{1}{L^*}\frac{\partial}{\partial x}\left[\left(H^* + Z^*\zeta\right) uU^*\right] + \frac{1}{L^*}\frac{\partial}{\partial y}\left[\left(H^* + Z^*\zeta\right) vU^*\right] = 0$$

Multiplying both sides by L^* and dividing by U^* yields:

$$\frac{\partial}{\partial x}\left[\left(H^* + Z^*\zeta\right) u\right] + \frac{\partial}{\partial y}\left[\left(H^* + Z^*\zeta\right) v\right] = 0$$

Subsequently dividing both sides by H^* produces:

$$\frac{\partial}{\partial x}\left[\left(\frac{H^*}{H^*} + \frac{Z^*}{H^*}\zeta\right) u\right] + \frac{\partial}{\partial y}\left[\left(\frac{H^*}{H^*} + \frac{Z^*}{H^*}\zeta\right) v\right] = 0$$

From the typical elevation scale it is known that $Z^* = U^{*2}/g^*$ and therefore:

$$\frac{Z^*}{H^*} = \frac{U^{*2}}{g^* H^*} = F^2$$

where F is the Froude number defined as $F = U^*/\sqrt{g^* H^*}$. This then leads to:

$$\frac{\partial}{\partial x}\left[\left(1 + F^2\zeta\right) u\right] + \frac{\partial}{\partial y}\left[\left(1 + F^2\zeta\right) v\right] = 0$$

which can also be written as:

$$\boxed{\nabla \cdot \left[\left(1 + F^2\zeta\right) \vec{u}\right] = 0}$$

C.2 Momentum balance

The momentum equation as given by equation (2.4) can be written in Cartesian coordinates as:

$$u^*\frac{\partial u^*}{\partial x^*} + v^*\frac{\partial u^*}{\partial y^*} + c_{\mathrm{D}}\frac{u^*\sqrt{u^{*2}+v^{*2}}}{H^*+\zeta^*} = -g^*\frac{\partial \zeta^*}{\partial x^*} + \nu_{\mathrm{h}}^*\left(\frac{\partial^2 u^*}{\partial x^{*2}} + \frac{\partial^2 u^*}{\partial y^{*2}}\right) + g^* i_0$$

$$u^*\frac{\partial v^*}{\partial x^*} + v^*\frac{\partial v^*}{\partial y^*} + c_{\mathrm{D}}\frac{v^*\sqrt{u^{*2}+v^{*2}}}{H^*+\zeta^*} = -g^*\frac{\partial \zeta^*}{\partial y^*} + \nu_{\mathrm{h}}^*\left(\frac{\partial^2 v^*}{\partial x^{*2}} + \frac{\partial^2 v^*}{\partial y^{*2}}\right)$$

The scaling will be performed for the moment balance in the x direction. First the quantities as defined in equation (2.9) will be substituted into the problem:

$$\frac{U^{*2}}{L^*}u\frac{\partial u}{\partial x} + \frac{U^{*2}}{L^*}v\frac{\partial u}{\partial y} + U^{*2}c_{\mathrm{D}}\frac{u\sqrt{u^2+v^2}}{H^*+Z^*\zeta} = \frac{-g^*Z^*}{L^*}\frac{\partial \zeta}{\partial x} + \frac{U^*}{L^{*2}}\nu_{\mathrm{h}}^*\left(\frac{\partial^2 u}{\partial x^2} + \frac{\partial u^2}{\partial y^2}\right) + g * i_0$$

Dividing both sides by U^{*2} and multiplying by L^* produces:

$$u\frac{\partial u}{\partial x} + v\frac{\partial u}{\partial y} + L^* c_{\mathrm{D}}\frac{u\sqrt{u^2+v^2}}{H^*\left(1+\frac{Z^*}{H^*}\zeta\right)} = -\frac{g^*Z^*}{U^{*2}}\frac{\partial \zeta}{\partial x} + \frac{\nu_{\mathrm{h}}^*}{U^*L^*}\left(\frac{\partial^2 u}{\partial x^2} + \frac{\partial^2 u}{\partial y^2}\right) + g^* i_0\frac{L^*}{U^{*2}}$$

From the definition of the elevation scale it is known that $Z^* = U^{*2}/g^*$. This can be substituted into the previous equation in the term describing the pressure gradient as caused by the free surface elevation. This eliminates the coefficient of this term. Additionally the term $F^2 = Z^*/H^*$ will be substituted into the denominator of the term describing the resistance. Also, equation (2.7) can be rearranged to find that $i_0 = \frac{U^{*2}}{g^*H^*}c_{\mathrm{D0}}$, which can be substituted into the term describing the energy slope. Finally the problem is rearranged to place all terms describing resistance on the right hand side of the equation and the remaining terms on the left hand side:

$$u\frac{\partial u}{\partial x} + v\frac{\partial u}{\partial y} + \frac{\partial \zeta}{\partial x} - \frac{\nu_{\mathrm{h}}^*}{U^*L^*}\left(\frac{\partial^2 u}{\partial x^2} + \frac{\partial^2 u}{\partial y^2}\right) = \frac{c_{\mathrm{D0}}L^*}{H^*} - \frac{c_{\mathrm{D}}L^*}{H^*}\frac{u\sqrt{u^2+v^2}}{1+F^2\zeta}$$

The same operations were performed for the y direction; please note that the energy slope is absent in the transverse direction. This leads to the following:

$$u\frac{\partial v}{\partial x} + v\frac{\partial v}{\partial y} + \frac{\partial \zeta}{\partial y} - \frac{\nu_{\mathrm{h}}^*}{U^*L^*}\left(\frac{\partial^2 v}{\partial x^2} + \frac{\partial^2 v}{\partial y^2}\right) = -\frac{c_{\mathrm{D}}L^*}{H^*}\frac{v\sqrt{u^2+v^2}}{1+F^2\zeta}$$

These two equations can be rewritten in a single equation in vector form as:

$$(\vec{u}\cdot\nabla)\,\vec{u} + \nabla\zeta - \frac{\nu_{\mathrm{h}}^*}{U^*L^*}\nabla^2\vec{u} = \frac{c_{\mathrm{D0}}L^*}{H^*}\boldsymbol{e}_x - \frac{c_{\mathrm{D}}L^*}{H^*}\frac{|\vec{u}|\vec{u}}{1+F^2\zeta}$$

Introducing the dimensionless quantities:

$$\nu = \frac{\nu_{\mathrm{h}}^*}{U^*L^*}, \qquad \mu = \frac{c_{\mathrm{D}}L^*}{H^*}, \qquad \text{and} \qquad \mu_0 = \frac{c_{\mathrm{D0}}L^*}{H^*} \tag{C.1}$$

which then leads to the scaled momentum equations using these dimensionless quantities:

$$\boxed{(\vec{u}\cdot\nabla)\,\vec{u}+\nabla\zeta-\nu\nabla^2\vec{u}=\mu_0\,\boldsymbol{e}_x-\frac{\mu|\vec{u}|\vec{u}}{1+F^2\zeta}}$$

Appendix D

Determining the linear problem

The linear problem needs to be determined. This appendix shows the steps for all three flow equations as the linear problem is determined.

D.1 Mass Balance

First the mass balance will be evaluated. Recalling that:

$$\begin{aligned} 0 &= \nabla \cdot \left[\left(1 + F^2 \zeta\right) \vec{u} \right] \\ &= \frac{\partial}{\partial x} \left[\left(1 + F^2 \zeta\right) u \right] + \frac{\partial}{\partial y} \left[\left(1 + F^2 \zeta\right) v \right] \end{aligned}$$

The expansion as given by equation (3.2) is substituted into this equation and produces:

$$\begin{aligned} &\frac{\partial}{\partial x} \left\{ \left[1 + F^2 \left(\zeta_0 + \epsilon\zeta_1 + \epsilon^2\zeta_2 + \ldots\right)\right] \left(u_0 + \epsilon u_1 + \epsilon^2 u_2 + \ldots\right) \right\} + \\ &\quad \frac{\partial}{\partial y} \left\{ \left[1 + F^2 \left(\zeta_0 + \epsilon\zeta_1 + \epsilon^2\zeta_2 + \ldots\right)\right] \left(v_0 + \epsilon v_1 + \epsilon^2 v_2 + \ldots\right) \right\} = 0 \end{aligned}$$

Multiplying out the innermost brackets yields:

$$\begin{aligned} &\frac{\partial}{\partial x} \left[\left(1 + F^2\zeta_0 + F^2\epsilon\zeta_1 + F^2\epsilon^2\zeta_2 + \ldots\right) \left(u_0 + \epsilon u_1 + \epsilon^2 u_2 + \ldots\right) \right] + \\ &\quad \frac{\partial}{\partial y} \left[\left(1 + F^2\zeta_0 + F^2\epsilon\zeta_1 + F^2\epsilon^2\zeta_2 + \ldots\right) \left(v_0 + \epsilon v_1 + \epsilon^2 v_2 + \ldots\right) \right] = 0 \end{aligned}$$

The multiplication of the next brackets is limited only to the lower orders of ϵ as all higher orders will be eliminated in the next step:

$$\begin{aligned} &\frac{\partial}{\partial x} \left(u_0 + \epsilon u_1 + \epsilon^2 u_2 + F^2\zeta_0 u_0 + F^2\zeta_0\epsilon u_1 + F^2\epsilon\zeta_1 u_0 + F^2\epsilon^2\zeta_1 u_1 + \ldots\right) + \\ &\quad \frac{\partial}{\partial y} \left(v_0 + \epsilon v_1 + \epsilon^2 v_2 + F^2\zeta_0 v_0 + F^2\zeta_0\epsilon v_1 + F^2\epsilon\zeta_1 v_0 + F^2\epsilon^2\zeta_1 v_1 + \ldots\right) = 0 \end{aligned}$$

Recalling that the lowest order solution showed that $u_0 = 1, v_0 = 0$ and $\zeta_0 = 0$ the following simplification can be made:

$$\frac{\partial}{\partial x}\left(1 + \epsilon u_1 + \epsilon^2 u_2 + F^2\epsilon\zeta_1 + F^2\epsilon^2\zeta_1 u_1 + \ldots\right) + \frac{\partial}{\partial y}\left(\epsilon v_1 + \epsilon^2 v_2 + F^2\epsilon^2\zeta_1 v_1 + \ldots\right) = 0$$

Taking the derivative with respect to ϵ and subsequently evaluating the result for $\epsilon = 0$ produces:

$$\left.\frac{\partial}{\partial\epsilon}\right|_{\epsilon=0} \Rightarrow \qquad \frac{\partial}{\partial x}\left(u_1 + F^2\zeta_1\right) + \frac{\partial}{\partial y}\left(v_1\right) = 0$$

which can be written in vector form as:

$$\boxed{\left(\frac{\partial}{\partial x} \quad , \quad \frac{\partial}{\partial y} \quad , \quad F^2\frac{\partial}{\partial x}\right)\cdot\phi_1 = 0} \tag{D.1}$$

D.2 Momentum in the streamwise direction

The moment balance in both the x and y direction will be treated in a similar fashion. First the expansion is substituted into the equation. Subsequently the derivative with respect to ϵ will be taken after which it is evaluated for $\epsilon = 0$. Recalling that the momentum balance in the x direction is given by:

$$u\frac{\partial u}{\partial x} + v\frac{\partial u}{\partial y} + \frac{\partial\zeta}{\partial x} - \nu\nabla^2 u = \mu_\mathrm{b} - \frac{\mu u\sqrt{u^2+v^2}}{1+F^2}$$

Due to the fact that applying these steps to the entire problem at once is not very clear, each term will be evaluated independently.

Advection: First the expansion is substituted into the advection term:

$$\phi \rightarrow \quad u\frac{\partial u}{\partial x} + v\frac{\partial u}{\partial y} \Rightarrow$$
$$(u_0 + \epsilon u_1 + \ldots)\frac{\partial}{\partial x}(u_0 + \epsilon u_1 + \ldots) + (v_0 + \epsilon v_1 + \ldots)\frac{\partial}{\partial x}(u_0 + \epsilon u_1 + \ldots)$$

recalling that $u_0 = 1$ and $v_0 = 0$, and multiplying the brackets out leads to:

$$\frac{\partial u_0}{\partial x} + \epsilon\frac{\partial u_1}{\partial x} + \epsilon u_1\frac{\partial u_0}{\partial x} + \epsilon^2 u_1\frac{\partial u_1}{\partial x} + \epsilon v_1\frac{\partial u_0}{\partial y} + \epsilon^2 v_1\frac{\partial u_1}{\partial y} + \ldots$$

Recognizing that $\frac{\partial u_0}{\partial x} = \frac{\partial u_0}{\partial y} = 0$ this simplifies into:

$$\epsilon\frac{\partial u_1}{\partial x} + \epsilon^2 u_1\frac{\partial u_1}{\partial x} + \epsilon^2 v_1\frac{\partial u_1}{\partial y} + \ldots$$

Subsequently taking the derivate with respect to ϵ and then evaluating the expression for $\epsilon = 0$ yields:

$$\left.\frac{\partial}{\partial\epsilon}\right|_{\epsilon=0} \Rightarrow \qquad \frac{\partial}{\partial x}u_1 \tag{D.2}$$

Free surface elevation: For the free surface elevation the same steps are performed. This leads to the following:

$$\phi \rightarrow \quad \frac{\partial \zeta}{\partial x} \quad \Rightarrow \qquad \frac{\partial}{\partial x}(\zeta_0 + \epsilon\zeta_1 + \epsilon^2\zeta_2 + \dots)$$

Taking the derivative with respect to ϵ and evaluating for $\epsilon = 0$ while keeping in mind that $\zeta_0 = 0$ yields:

$$\left.\frac{\partial}{\partial \epsilon}\right|_{\epsilon=0} \Rightarrow \qquad \frac{\partial}{\partial x}\zeta_1 \tag{D.3}$$

Viscous effects: Analogously:

$$\begin{aligned}\phi \rightarrow \quad & -\nu\left(\frac{\partial^2 u}{\partial x^2} + \frac{\partial^2 u}{\partial y^2}\right) \Rightarrow \\ & -\nu\left[\frac{\partial^2}{\partial x^2}(u_0 + \epsilon u_1 + \dots) + \frac{\partial^2}{\partial y^2}(u_0 + \epsilon u_1 + \dots)\right] \\ & -\nu\left(\frac{\partial u_0}{\partial x^2} + \epsilon\frac{\partial^2 u_1}{\partial x^2} + \frac{\partial u_0}{\partial y^2} + \epsilon\frac{\partial^2 u_1}{\partial y^2} + \dots\right)\end{aligned}$$

Noting that $\frac{\partial^2 u_0}{\partial x^2} = \frac{\partial^2 u_0}{\partial y^2} = 0$ and taking the derivative with respect to ϵ and evaluating for $\epsilon = 0$ leads to:

$$\left.\frac{\partial}{\partial \epsilon}\right|_{\epsilon=0} \Rightarrow \qquad -\nu\left(\frac{\partial^2 u_1}{\partial x^2} + \frac{\partial^2 u_1}{\partial y^2}\right) = -\nu\nabla^2 u_1 \tag{D.4}$$

Energy Slope No substitution of ϕ is possible into the term describing the energy slope. This is logical as the energy slope is not affected by the spatially varying roughness and therefore it only influences the flow in the lowest order.

Spatially varying roughness: The final term in the momentum balance in the downstream direction is the spatially varying roughness term. Here both equations (3.1) and (3.2) are substituted into the term. This leads to:

$$\begin{aligned}\mu \text{ and } \phi \rightarrow \quad & -\frac{\mu u\sqrt{u^2+v^2}}{1+F^2\zeta} \Rightarrow \\ & -\frac{[\mu_0 + \mu_1(x,y)]\,(u_0 + \epsilon u_1 + \dots)\sqrt{(u_0 + \epsilon u_1 + \dots)^2 + (v_0 + \epsilon v_1 + \dots)^2}}{1 + F^2\,(\zeta_0 + \epsilon\zeta_1 + \dots)}\end{aligned}$$

Solving this on paper proved to be cumbersome due to the vast amount of terms. Therefore Maple was used to solve this and lead to:

$$\left.\frac{\partial}{\partial \epsilon}\right|_{\epsilon=0} \Rightarrow \qquad -\mu_1(x,y) - 2\mu_0 u_1 + \mu_0 F^2\zeta_1 \tag{D.5}$$

Combining subsolutions (D.2), (D.3), (D.4) and (D.5) produces:

$$\boxed{\frac{\partial}{\partial x}u_1 + \frac{\partial}{\partial x}\zeta_1 - \nu\nabla^2 u_1 + 2\mu_0 u_1 - \mu_0 F^2\zeta_1 = -\mu_1(x,y)}$$

where the roughness has been moved to one side of the equation and the other terms have been moved to the left hand side of the equation. This can be rewritten in vector form as:

$$\boxed{\left(\frac{\partial}{\partial x} - \nu\nabla^2 + 2\mu_0 \quad , \quad 0 \quad , \quad \frac{\partial}{\partial x} - \mu_0 F^2\right) \cdot \phi_1 = -\mu_1} \tag{D.6}$$

D.3 Momentum in the transverse direction

The y direction is treated in the same way as the x direction where only the starting equation is the other momentum equation. As a result only the solutions are shown here. The result of substitution, derivation with respect to ϵ and subsequent evaluation for $\epsilon = 0$ produces the following results:

$$\boxed{\frac{\partial}{\partial x} v_1 + \frac{\partial}{\partial y}\zeta_1 - \nu\nabla^2 v_1 + \mu_0 v_1 = 0}$$

This can be rewritten in vector form as:

$$\boxed{\left(0 \quad , \quad \frac{\partial}{\partial x} - \nu\nabla^2 + \mu_0 \quad , \quad \frac{\partial}{\partial y}\right) \cdot \phi_1 = 0} \tag{D.7}$$

The solutions as found for the momentum equations in x and y (equations (D.6) and (D.7)) and for the mass balance (equation (D.1)) can be combined in a single linear problem as defined by equation (3.3). Now that the Linear operator $\mathcal{L}$ and the source term $\boldsymbol{b}_1$ are found the problem is given by:

$$\mathcal{L} \cdot \phi_1 = \boldsymbol{b}_1$$

$$\Downarrow$$

$$\begin{pmatrix} \frac{\partial}{\partial x} - \nu\nabla^2 + 2\mu_0 & 0 & \frac{\partial}{\partial x} - \mu_0 F^2 \\ 0 & \frac{\partial}{\partial x} - \nu\nabla^2 + \mu_0 & \frac{\partial}{\partial y} \\ \frac{\partial}{\partial x} & \frac{\partial}{\partial y} & F^2\frac{\partial}{\partial x} \end{pmatrix} \cdot \begin{pmatrix} u_1 \\ v_1 \\ \zeta_1 \end{pmatrix} = \begin{pmatrix} -\mu_1 \\ 0 \\ 0 \end{pmatrix}$$

Appendix E

Fourier series representation

In this appendix the problem as defined by equation (3.3) is rewritten in terms of Fourier coefficients. All three equations of the first order linear problem are derived individually.

E.1 Mass Balance

Recalling that the first order linear problem derived from the mass balance is given by:

$$\frac{\partial}{\partial x}\left(u_1 + F^2\zeta_1\right) + \frac{\partial}{\partial y}\left(v_1\right) = 0$$

In which ϕ can be substituted for the assumed form (3.6) giving:

$$\begin{aligned}
\frac{\partial u_1}{\partial x} &= \sum_{m,n} i\alpha_m \cdot U_{1mn} \cos\beta_n y \exp(i\alpha_m x) + \text{c.c.} \\
F^2\frac{\partial \zeta_1}{\partial x} &= \sum_{m,n} F^2 i\alpha_m \cdot Z_{1mn} \cos\beta_n y \exp(i\alpha_m x) + \text{c.c.} \\
\frac{\partial v_1}{\partial y} &= \sum_{m,n} \beta_n \cdot V_{1mn} \cos\beta_n y \exp(i\alpha_m x) + \text{c.c.}
\end{aligned}$$

which leads to:

$$0 = \sum_{m,n}\left(i\alpha_m U_{1mn} + i\alpha_m F^2 Z_{1mn} + \beta_n V_{1mn}\right)\cos\beta_n y \exp(i\alpha_m x) + \text{c.c.}$$

Due to the fact that $\cos\beta_n y \exp(i\alpha_m x)$ will not always equal zero it can be stated that:

$$i\alpha_m U_{1mn} + i\alpha_m F^2 Z_{1mn} + \beta_n V_{1mn} = 0$$

$$\boxed{\begin{pmatrix} i\alpha_m & , & \beta_n & , & i\alpha_m F^2 \end{pmatrix} \cdot \Phi_{1mn} = 0} \tag{E.1}$$

E.2 Momentum in the streamwise direction

Recalling that the first order linear problem derived from the momentum equation in x is given by:

$$\frac{\partial}{\partial x}u_1 + \frac{\partial}{\partial x}\zeta_1 - \nu\nabla^2 u_1 + 2\mu_0 u_1 - \mu_0 F^2 \zeta_1 = -\mu_1(x,y)$$

The assumed solution (3.6) and the roughness as given by (3.5) can be used to rewrite each term as:

$$\begin{aligned}
\frac{\partial u_1}{\partial x} &= \sum_{m,n} i\alpha_m \cdot U_{1mn} \cos\beta_n y \exp(i\alpha_m x) + \text{c.c.} \\
\frac{\partial \zeta_1}{\partial x} &= \sum_{m,n} i\alpha_m \cdot Z_{1mn} \cos\beta_n y \exp(i\alpha_m x) + \text{c.c.} \\
-\nu\nabla^2 u_1 &= -\nu\left(\frac{\partial^2 u_1}{\partial x^2} + \frac{\partial^2 u_1}{\partial y^2}\right) \\
&= \sum_{m,n} -\nu\left[i^2\alpha_m^2 U_{1mn}\cos\beta_n y\exp(i\alpha_m x) + \ldots\right. \\
&\qquad\qquad \left.\ldots\,(-)\beta_n^2 U_{1mn}\cos\beta_n y\exp(i\alpha_m x)\right] + \text{c.c.} \\
&= \sum_{m,n} -\nu\left(-\alpha_m^2 - \beta_n^2\right) U_{1mn}\cos\beta_n y\exp(i\alpha_m x) + \text{c.c.} \\
&= \sum_{m,n} \nu\left(\alpha_m^2 + \beta_n^2\right) U_{1mn}\cos\beta_n y\exp(i\alpha_m x) + \text{c.c.} \\
2\mu_0 u_1 &= \sum_{m,n} 2\mu_0 U_{1mn}\cos\beta_n y\exp(i\alpha_m x) + \text{c.c.} \\
-\mu_0 F^2\zeta_1 &= \sum_{m,n} -\mu_0 F^2 Z_{1mn}\cos\beta_n y\exp(i\alpha_m x) + \text{c.c.}
\end{aligned}$$

When recombined this leads to:

$$\begin{aligned}
\sum_{m,n}\big[&i\alpha_m U_{1mn} + i\alpha_m Z_{1mn} + \nu\left(\alpha_m^2+\beta_n^2\right)U_{1mn} + \ldots \\
&\ldots 2\mu_0 U_{1mn} - \mu_0 F^2 Z_{1mn}\big]\cos\beta_n y\exp(i\alpha_m x) + \text{c.c.} \\
&= -C_{mn}\cos\beta_n y\exp(i\alpha_m x) + \text{c.c.}
\end{aligned}$$

Similarly to the mass-balance it can then be concluded that:

$$\left[i\alpha_m U_{1mn} + i\alpha_m Z_{1mn} + \nu\left(\alpha_m^2+\beta_n^2\right)U_{1mn} + 2\mu_0 U_{1mn} - \mu_0 F^2 Z_{1mn}\right] = -C_{mn}$$

Which can also be written as:

$$\boxed{\left(i\alpha_m + \nu\left(\alpha_m^2+\beta_n^2\right) + 2\mu_0 \quad , \quad 0 \quad , \quad i\alpha_m - \mu_0 F^2\right)\cdot \Phi_{1mn} = -C_{mn}} \tag{E.2}$$

E.3 Momentum in the transverse direction

The first order linear problem derived from the momentum equation in the y direction is treated in the same way. Substitution of equation (3.6) into (D.7)

leads to the following terms:

$$\begin{aligned}
\frac{\partial v_1}{\partial x} &= \sum_{m,n} i\alpha_m \cdot V_{1mn} \sin\beta_n y \exp(i\alpha_m x) + \text{c.c.} \\
\frac{\partial \zeta_1}{\partial y} &= \sum_{m,n} -\beta_n \cdot Z_{1mn} \sin\beta_n y \exp(i\alpha_m x) + \text{c.c.} \\
-\nu\nabla^2 v_1 &= \sum_{m,n} \nu(\alpha_m^2 + \beta_n^2) \cdot V_{1mn} \sin\beta_n y \exp(i\alpha_m x) + \text{c.c.} \\
\mu_0 v_1 &= \sum_{m,n} \mu_0 V_{1mn} \sin\beta_n y \exp(i\alpha_m x) + \text{c.c.}
\end{aligned}$$

When recombined into the momentum equation this gives:

$$\begin{aligned}
\sum_{m,n} [i\alpha_m V_{1mn} - \beta_n Z_{1mn} + \nu(\alpha_m^2 + \beta_n^2) V_{1mn} \\
+\mu_0 V_{1mn}] \sin\beta_n y \exp(i\alpha_m x) + \text{c.c.} = 0
\end{aligned}$$

Noting that $\sin\beta_n y \exp(i\alpha_m x)$ cannot always be zero it may be stated that:

$$\left[i\alpha_m V_{1mn} - \beta_n Z_{1mn} + \nu(\alpha_m^2 + \beta_n^2) V_{1mn} + \mu_0 V_{1mn}\right] = 0$$

$$\boxed{\begin{pmatrix} 0 & , & i\alpha_m + \nu(\alpha_m^2 + \beta_n^2) + \mu_0 & , & -\beta_n \end{pmatrix} \cdot \Phi_{1mn} = 0} \qquad \text{(E.3)}$$

The linear problem posed by (3.3) then reduces to the following system for the m, n^{th} mode using equations (E.1), (E.2) and (E.3):

$$\mathbf{A}_{mn} \cdot \Phi_{1mn} = \mathcal{S}_{1mn}$$

where $\mathbf{A}_{mn}$ is the linear operator for the m, n^{th} mode and $\mathcal{S}_{1mn}$ is the first order source term for that mode; and are given by:

$$\mathbf{A}_{mn} = \begin{pmatrix} X_2 & 0 & i\alpha_m - \mu_0 F^2 \\ 0 & X_1 & -\beta_n \\ i\alpha_m & \beta_n & i\alpha_m F^2 \end{pmatrix} \qquad \text{and} \qquad \mathcal{S}_{1mn} = \begin{pmatrix} -C_{mn} \\ 0 \\ 0 \end{pmatrix}$$

where $X_p = i\alpha_m + \nu(\alpha_m^2 + \beta_n^2) + p\mu_0$ for $p = 1, 2, 3$.

Appendix F

Matrix Inverse

In this appendix it is shown how the inverse of the matrix $\mathbf{A}_{mn}$ is found.

F.1 Matrix of Minors

The first step in calculating the inverse of $\mathbf{A}_{mn}$ is to create a matrix of minors. This is done by going through each element of the matrix and replacing it by the determinant of the remaining 2 x 2 matrix that results from deleting the elements row and column. For the first element this will result in:

$$m_{11} = \det \begin{vmatrix} a_{22} & a_{23} \\ a_{32} & a_{33} \end{vmatrix} = a_{22}a_{33} - a_{23}a_{32}$$

where a refers to an element in the original matrix, m refers to an element in the matrix of minors and the subscript denotes its respective row and column position. For $\mathbf{A}_{mn}$ the first element of the matrix of minors is given by:

$$\det \begin{vmatrix} X_1 & -\beta_n \\ \beta_n & i\alpha_m F^2 \end{vmatrix} = X_1 i\alpha_m F^2 + \beta_n^2$$

and the second element is given by:

$$\det \begin{vmatrix} 0 & -\beta_n \\ i\alpha_m & i\alpha_m F^2 \end{vmatrix} = \beta_n i\alpha_m$$

All other elements have been determined analogously leading to the matrix of minors:

$$\begin{pmatrix} X_1 i\alpha_m F^2 + \beta_n^2 & \beta_n i\alpha_m & -X_1 i\alpha_m \\ -\beta_n i\alpha_m + \beta_n \mu_0 F^2 & X_2 i\alpha_m F^2 + \alpha_m^2 + \mu_0 F^2 i\alpha_m & X_2\beta_n \\ -X_1 i\alpha_m + X_1 \mu_0 F^2 & -X_2\beta_n & X_2 X_1 \end{pmatrix}$$

F.2 Matrix of Cofactors

The next step is to determine the matrix of cofactors by multiplying the elements in the matrix of minors by the following: $\begin{matrix} + & - & + \\ - & + & - \\ + & - & + \end{matrix}$ which then leads to the

following matrix of cofactors:

$$\begin{pmatrix} X_1 i\alpha_m F^2 + \beta_n^2 & -\beta_n i\alpha_m & -X_1 i\alpha_m \\ -\beta_n \left[\mu_0 F^2 - i\alpha_m\right] & i\alpha_m \left[X_2 F^2 - i\alpha_m + \mu_0 F^2\right] & -X_2\beta_n \\ X_1 \left[\mu_0 F^2 - i\alpha_m\right] & X_2\beta_n & X_2 X_1 \end{pmatrix}$$

F.3 Determinant

The determinant of the matrix is then determined by multiplying all elements in single a row or column of the matrix of cofactors with their corresponding elements in the original matrix. It should not matter which row or column is selected. In this case the determinant D is thus given by:

$$\begin{aligned} D_{mn} &= X_2 \left(X_1 i\alpha_m F^2 + \beta_n^2\right) + 0\left(-\beta_n i\alpha_m\right) - X_1 i\alpha_m \left(i\alpha_m - \mu_0 F^2\right) \\ &= X_2 X_1 i\alpha_m F^2 + X_2\beta_n^2 + X_1\alpha_m^2 + X_1 i\alpha_m \mu_0 F^2 \\ &= X_1\alpha_m^2 + X_2\beta_n^2 + X_1 i\alpha_m F^2 \left(X_2 + \mu_0\right) \\ &= X_1\alpha_m^2 + X_2\beta_n^2 + X_1 X_3 i\alpha_m F^2 \end{aligned}$$

F.4 The resulting inverse of the matrix

The inverse of the matrix is then determined by multiplying the reciprocal of the determinant with the transpose of the matrix of cofactors. This leads to the following inverse of $\mathbf{A}_{mn}$:

$$\mathbf{A}_{mn}^{-1} = \frac{1}{D_{mn}} \begin{pmatrix} X_1 i\alpha_m F^2 + \beta_n^2 & -\beta_n \left[\mu_0 F^2 - i\alpha_m\right] & X_1 \left[\mu_0 F^2 - i\alpha_m\right] \\ -\beta_n i\alpha_m & i\alpha_m \left[F^2 \left(X_2 + \mu_0\right) - i\alpha_m\right] & X_2\beta_n \\ -X_1 i\alpha_m & -X_2\beta_n & X_2 X_1 \end{pmatrix}$$

Appendix G

Forcing in the second order

This appendix shows how the second order problem is defined. This leads to the same linear operator $\mathcal{L}$ as in the first order, but the forcing of the system, given by $\boldsymbol{b}_2$ significantly differs from the first order as it contains convolutions of solutions in the first order.

G.1 Defining the second order problem

The second order problem must first be defined before the same eigenvalue solution method can be applied.

G.1.1 Mass Balance

The mass balance in the second order is found as:

$$\begin{aligned}\left(\frac{\partial}{\partial x} \quad , \quad \frac{\partial}{\partial y} \quad , \quad F^2\frac{\partial}{\partial x}\right)\cdot\phi_2 &= -F^2\frac{\partial}{\partial x}\zeta_1 u_1 - F^2\frac{\partial}{\partial y}\zeta_1 v_1 \\ &= -F^2\nabla\cdot(\zeta_1\vec{u}_1) \end{aligned} \tag{G.1}$$

Where the contribution of the first order in the second order will be written as:

$$\mathcal{M} = F^2\nabla\cdot(\zeta_1\vec{u}_1)$$

G.1.2 Momentum in the streamwise direction

The momentum equations in x has two contributions from the first order as forcing in the second order. These originate from the non-linear terms in the momentum equations; namely the advection and the bottom friction formulation:

$$\begin{aligned}\left(\frac{\partial}{\partial x} - \nu\nabla^2 + 2\mu_0 \quad , \quad 0 \quad , \quad \frac{\partial}{\partial x} - \mu_0 F^2\right)\phi_2 = &-\left(u_1\frac{\partial u_1}{\partial x} + v_1\frac{\partial u_1}{\partial y}\right)\ldots \\ &-\left(2\mu_1 u_1 - \mu_1 F^2\zeta_1 + \mu_0 u_1^2 - 2\mu_0 F^2 u_1\zeta_1 + \frac{1}{2}\mu_0 v_1^2 + \mu_0 F^4\zeta_1^2\right)\end{aligned}$$

Here two terms will be defined for ease of notation which are:

$$\mathcal{A}_x = u_1 \frac{\partial u_1}{\partial x} + v_1 \frac{\partial u_1}{\partial y}$$
$$\mathcal{R}_x = \mu_0 \left(u_1 - F^2\zeta_1\right)^2 + \mu_0 \frac{1}{2} v_1^2 + \mu_1 \left(2u_1 - F^2\zeta_1\right)$$

where $\mathcal{A}_x$ is the second order forcing as caused by advection in the momentum equations and $\mathcal{R}_x$ is the second order forcing as caused by the bottom friction.

G.1.3 Momentum in the transverse direction

Similarly, the momentum equation in the y direction can be found, which is given by:

$$\left(0 \quad , \quad \frac{\partial}{\partial x} \; -\nu\nabla^2 + \mu_0 \quad , \quad \frac{\partial}{\partial y}\right) \phi_2 = -\left(u_1 \frac{\partial v_1}{\partial x} + v_1 \frac{\partial v_1}{\partial y}\right) \ldots$$
$$- \left(\mu_1 v_1 + \mu_0 v_1 u_1 - \mu_0 v_1 F^2 \zeta_1\right)$$

Note that the linear operator is still the same and that also for the cross stream direction only the forcing has changed. Two terms will be introduced for ease of notation:

$$\mathcal{A}_y = u_1 \frac{\partial v_1}{\partial x} + v_1 \frac{\partial v_1}{\partial y}$$
$$\mathcal{R}_y = \mu_0 v_1 \left(u_1 - F^2\zeta_1\right) + \mu_1 v_1$$

G.2 Eigenfunction projections of the second order forcing

In this section the source term $\boldsymbol{b}_2$ will be rewritten using the eigenfunctions to eventually determine the effect of the spatially varying resistance on the mean flow in the channel. The result of this is substituted into the forcing term to evaluate the second order flow change in $U_{2,00}$; its spatial average gives a base contribution to the downstream flow in the second order that is spatially independent. During the spatial averaging, all other combinations of modes yield exactly zero contribution to the mean flow found in U_{200}.

As an example the first term in $\mathcal{A}_x$ will be determined step by step in this section; this term is given by $u_1 \frac{\partial u_1}{\partial x}$. Recalling from equation (3.6) that the downstream flow velocity in the first order can be written as:

$$u_1 = \sum_{m,n} \left[U_{1,mn} \cos\beta_n y \exp(i\alpha_m x) + \overline{U_{1,mn}} \cos\beta_n y \exp(-i\alpha_m x)\right]$$

When the derivative of this function is taken with respect to x this leads to:

$$\frac{\partial u_1}{\partial x} = \sum_{m,n} \left[i\alpha_m U_{1,mn} \cos\beta_n y \exp(i\alpha_m x) - i\alpha_m \overline{U_{1,mn}} \cos\beta_n y \exp(-i\alpha_m x)\right]$$

The two terms are recombined and are spatially averaged. The spatially averaging is performed so that only pairs of modes remain as a contribution. Before the

spatial averaging, each term in the summation must be multiplied by each term in the summation of the second part. These combinations, outside of similar pairs when indexes are considered, lead to trivial contributions.

$$\begin{aligned}\left\langle u_1 \frac{\partial u_1}{\partial x} \right\rangle = \sum_{m,n} \big[& i\alpha_m U_{1,mn}^2 \cos^2 \beta_n y \exp(2i\alpha_m x) \\ & - i\alpha_m U_{1,mn} \overline{U_{1,mn}} \cos^2 \beta_n y \\ & + i\alpha_m \overline{U_{1,mn}} U_{1,mn} \cos^2 \beta_n y \\ & - i\alpha_m \overline{U_{1,mn}}^2 \cos^2 \beta_n y \exp(-2i\alpha_m x) \big]\end{aligned}$$

After simplification this leads to:

$$\left\langle u_1 \frac{\partial u_1}{\partial x} \right\rangle = \sum_{m,n} \alpha_m \cos^2 \beta_n y \left[i U_{1,mn}^2 \exp(2i\alpha_m x) + \text{c.c.} \right]$$

Analogously, all other expressions in the source term $\boldsymbol{b}_2$ have been rewritten in a similar fashion. This leads to the following contributions:

Forcing of the second order as caused by advection in the downstream direction $\mathcal{A}_x$

$$\left\langle u_1 \frac{\partial u_1}{\partial x} \right\rangle = \sum_{m,n} \alpha_m \cos^2 \beta_n y \left[i U_{1,mn}^2 \exp(2i\alpha_m x) + \text{c.c.} \right]$$

$$\left\langle v_1 \frac{\partial u_1}{\partial y} \right\rangle = \sum_{m,n} -\beta_n \sin^2 \beta_n y \left[V_{1,mn} \left(U_{1,mn} \exp(2i\alpha_m x) + \overline{U_{1,mn}} \right) + \text{c.c.} \right]$$

Forcing of the second order as caused by advection in the transverse direction $\mathcal{A}_y$

$$\left\langle u_1 \frac{\partial v_1}{\partial x} \right\rangle = \sum_{m,n} \frac{\alpha_m}{2} \sin(2\beta_n y) \left[i V_{1,mn} \left(U_{1,mn} \exp(2i\alpha_m x) + \overline{U_{1,mn}} \right) + \text{c.c.} \right]$$

$$\left\langle v_1 \frac{\partial v_1}{\partial y} \right\rangle = \sum_{m,n} \frac{\beta_n}{2} \sin(2\beta_n y) \left[V_{1,mn}^2 \exp(2i\alpha_m x) + |V_{1,mn}|^2 + \text{c.c.} \right]$$

Forcing of the second order as caused by flow resistance in the downstream direction $\mathcal{R}_x$

$$\begin{aligned}\left\langle \mu_0 \left(u_1 - F^2 \zeta_1 \right)^2 \right\rangle = \sum_{m,n} \mu_0 \cos^2 \beta_n y \Big[& \left(U_{1,mn} - F^2 Z_{1,mn} \right)^2 \exp(2i\alpha_m x) \\ & + \left| U_{1,mn} - F^2 Z_{1,mn} \right|^2 + \text{c.c.} \Big]\end{aligned}$$

$$\left\langle \frac{1}{2} \mu_0 v_1^2 \right\rangle = \sum_{m,n} \frac{1}{2} \mu_0 \sin^2 \beta_n y \left[V_{1,mn}^2 \exp(2i\alpha_m x) + |V_{1,mn}|^2 + \text{c.c.} \right]$$

$$\begin{aligned}\left\langle \mu_1 \left(2u_1 - F^2 \zeta_1 \right) \right\rangle = \sum_{m,n} & \cos^2 \beta_n y \\ & \left[\left(2U_{1,mn} - F^2 Z_{1,mn} \right) \left(C_{mn} \exp(2i\alpha_m x) + \overline{C_{mn}} \right) + \text{c.c} \right]\end{aligned}$$

Forcing of the second order as caused by the flow resistance in the transverse direction $\mathcal{R}_y$

$$\left\langle \mu_0 v_1 \left(u_1 - F^2 \zeta_1 \right) \right\rangle = \sum_{m,n} \frac{\mu_0}{2} \sin(2\beta_n y) \left[\left(U_{1,mn} - F^2 Z_{1,mn} \right) \left(V_{1,mn} \exp(2i\alpha_m x) + \overline{V_{1,mn}} \right) + \text{c.c.} \right]$$

$$\langle \mu_1 v_1 \rangle = \sum_{m,n} \frac{1}{2} \sin(2\beta_n y) \left[V_{1,mn} \left(C_{mn} \exp(2i\alpha_m x) + \overline{C_{mn}} \right) + \text{c.c.} \right]$$

Forcing of the second order as caused by non-linearities in the continuity equation $\mathcal{M}$

$$\left\langle F^2 \frac{\partial(\zeta_1 u_1)}{\partial x} \right\rangle = \sum_{m,n} 2\alpha_m F^2 \cos^2 \beta_n y \left[i Z_{1,mn} U_{1,mn} \exp(2i\alpha_m x) + \text{c.c.} \right]$$

$$\left\langle F^2 \frac{\partial(\zeta_1 u_1)}{\partial y} \right\rangle = \sum_{m,n} F^2 \cos(2\beta_n y) \left[Z_{1,mn} \left(V_{1,mn} \exp(2i\alpha_m x) + \overline{V_{1,mn}} \right) + \text{c.c.} \right]$$

Appendix H

Spatial averaging contributing terms

In this appendix the spatial average is determined of the four terms that contribute to the mean downstream flow velocity in the second order. Recalling from the first order solution that:

$$U_{1,mn} = \frac{-C_{mn}}{D_{mn}}\left(X_1 i\alpha_m F^2 + \beta_n^2\right) \quad \text{and} \quad \overline{U_{1,mn}} = \frac{\overline{-C_{mn}}}{\overline{D_{mn}}}\left(-\overline{X_1} i\alpha_m F^2 + \beta_n^2\right) \tag{H.1}$$

$$V_{1,mn} = \frac{-C_{mn}}{D_{mn}}\left(-\beta_n i\alpha_m\right) \qquad \text{and} \qquad \overline{V_{1,mn}} = \frac{\overline{-C_{mn}}}{\overline{D_{mn}}}\left(\beta_n i\alpha_m\right) \tag{H.2}$$

$$Z_{1,mn} = \frac{-C_{mn}}{D_{mn}}\left(-X_1 i\alpha_m\right) \qquad \text{and} \qquad \overline{Z_{1,mn}} = \frac{-\overline{C_{mn}}}{\overline{D_{mn}}}\left(\overline{X_1} i\alpha_m\right) \tag{H.3}$$

For ease of notation the mode indices m and n will be dropped in the following analysis, as will the summation over all of the modes. This may be done as we are purely interested in the spatially invariant contribution, which may be seen as a superposition of individual contributions from each mode. All other combinations of mode are trivial.

Advection

First the advection term will be analysed:

$$\left\langle v_1 \frac{\partial u_1}{\partial y} \right\rangle = -\beta \frac{1}{2}\left[V_1 \overline{U_1} + \overline{V_1} U_1\right]$$

Substitution of equations (H.1) and (H.2) leads to:

$$\begin{aligned} V_1\overline{U_1} &= \left(\frac{C\beta i\alpha}{D}\right)\left(\frac{\overline{CX_1}\alpha iF^2 - \overline{C}\beta^2}{\overline{D}}\right) \\ &= \frac{-C\overline{CX_1}\beta\alpha^2F^2 - C\overline{C}\beta^3 i\alpha}{D\overline{D}} \\ \overline{V_1}U_1 &= \left(\frac{-\overline{C}\beta i\alpha}{\overline{D}}\right)\left(\frac{-CX_1\alpha iF^2 - C\beta^2}{D}\right) \\ &= \frac{-C\overline{C}X_1\alpha^2\beta F^2 + C\overline{C}\beta^3 i\alpha}{D\overline{D}} \end{aligned}$$

Leading to:

$$\begin{aligned} \left\langle v_1\frac{\partial u_1}{\partial y}\right\rangle &= -\beta\frac{1}{2}\frac{-|C|^2\overline{X_1}\alpha^2\beta F^2 - |C|^2 X_1\alpha^2\beta F^2}{|D|^2} \\ &= \frac{1}{2}\frac{|C|^2\alpha^2\beta^2F^2\left(X_1+\overline{X_1}\right)}{|D|^2} \end{aligned} \tag{H.4}$$

Term 2

$$\begin{aligned} \left\langle \mu_0\left(u_1 - F^2\zeta_1\right)^2\right\rangle &= \mu_0\frac{1}{2}\left[2\left|U_1 - F^2Z_1\right|^2\right] \\ &= \mu_0\left[\left(U_1 - F^2Z_1\right)\left(\overline{U_1} - F^2\overline{Z_1}\right)\right] \\ &= \mu_0\left[U_1\overline{U_1} - F^2\left(Z_1\overline{U_1} + \overline{Z_1}U_1\right) + F^4Z_1\overline{Z_1}\right] \end{aligned}$$

Each of these terms will be substituted individually; first $U_1\overline{U_1}$ is considered:

$$\begin{aligned} U_1\overline{U_1} &= \left(\frac{-CX_1\alpha iF^2 - C\beta^2}{D}\right)\left(\frac{\overline{CX_1}\alpha iF^2 - \overline{C}\beta^2}{\overline{D}}\right) \\ &= \frac{|C|^2|X_1|^2\alpha^2F^4 + |C|^2\beta^4 + |C|^2\alpha\beta^2X_1iF^2 - |C|^2\alpha\beta^2\overline{X_1}iF^2}{|D|^2} \\ &= \frac{|C|^2|X_1|^2\alpha^2F^4 - |C|^2\alpha^2\beta^2F^2 + |C|^2\beta^4}{|D|^2} \end{aligned}$$

Second the term $F^2(Z_1\overline{U_1} + \overline{Z_1}U_1)$ is expanded:

$$
\begin{aligned}
-F^2\left(Z_1\overline{U_1} + \overline{Z_1}U_1\right) \rightarrow \\
Z_1\overline{U_1} &= \left(\frac{CX_1 i\alpha}{D}\right)\left(\frac{\overline{CX_1}i\alpha F^2 - \overline{C}\beta^2}{\overline{D}}\right) \\
&= \frac{-|C|^2|X_1|^2\alpha^2F^2 - |C|^2X_1 i\alpha\beta^2}{|D|^2} \\
\overline{Z_1}U_1 &= \left(\frac{-\overline{CX_1}i\alpha}{\overline{D}}\right)\left(\frac{-CX_1 i\alpha F^2 - C\beta^2}{D}\right) \\
&= \frac{-|C|^2|X_1|^2\alpha^2F^2 + |C|^2\overline{X_1}i\alpha\beta^2}{|D|^2} \\
-F^2\left(Z_1\overline{U_1} + \overline{Z_1}U_1\right) &= -F^2\left(\frac{-2|C|^2|X_1|^2\alpha^2F^2 + |C|^2\overline{X_1}i\alpha\beta^2 - |C|^2X_1 i\alpha\beta^2}{|D|^2}\right) \\
&= -F^2\left(\frac{-2|C|^2|X_1|^2\alpha^2F^2 + 2|C|^2\alpha^2\beta^2}{|D|^2}\right) \\
&= \frac{2|C|^2|X_1|^2\alpha^2F^4 - 2|C|^2\alpha^2\beta^2F^2}{|D|^2}
\end{aligned}
$$

Finally the last term is combined and is represented by:

$$
\begin{aligned}
F^4 Z_1\overline{Z_1} &= F^4\left(\frac{CX_1 i\alpha}{D}\right)\left(\frac{-\overline{CX_1}i\alpha}{\overline{D}}\right) \\
&= \frac{F^4|C|^2|X_1|^2\alpha^2}{|D|^2}
\end{aligned}
$$

When all previous terms are combined the spatially averaged result is given by:

$$
\left\langle \mu_0\left(u_1 - F^2\zeta_1\right)^2\right\rangle = \frac{\mu_0|C|^2\left(4\alpha^2F^4|X_1|^2 - 3\alpha^2\beta^2F^2 + \beta^4\right)}{|D|^2} \tag{H.5}
$$

Term 3

$$
\begin{aligned}
\left\langle \frac{1}{2}\mu_0 v_1^2\right\rangle &= \frac{1}{2}\mu_0\left[V_1\overline{V_1}\right] \\
&= \frac{1}{2}\mu_0\left(\frac{Ci\alpha\beta}{D}\right)\left(\frac{-\overline{C}i\beta\alpha}{\overline{D}}\right) \\
&= \frac{1}{2}\frac{\mu_0\alpha^2\beta^2|C|^2}{|D|^2}
\end{aligned} \tag{H.6}
$$

Term 4

$$\begin{aligned}
\left\langle \mu_1(2u_1 - F^2\zeta_1)\right\rangle &= \frac{1}{2}\left[\overline{C}\left(2U_1 - F^2 Z_1\right) + C\left(2\overline{U_1} - F^2\overline{Z_1}\right)\right] \\
&= \frac{1}{2}\left[\frac{-3|C|^2 X_1 \alpha i F^2 - 2|C|^2\beta^2}{D} + \frac{3|C|^2\overline{X_1}\alpha i F^2 - 2|C|^2\beta^2}{\overline{D}}\right] \\
&= \frac{|C|^2}{2}\left[\frac{-3X_1\alpha i F^2 - 2\beta^2}{D} + \frac{3\overline{X_1}\alpha i F^2 - 2\beta^2}{\overline{D}}\right] \\
&= \frac{|C|^2}{2}\left[\frac{-3X_1\alpha i F^2\overline{D} - 2\beta^2\overline{D} + 3\overline{X_1}\alpha i F^2 D - 2\beta^2 D}{|D|^2}\right] \\
&= \frac{|C|^2}{2}\left[\frac{3\alpha^2 F^2\overline{D} - 2\beta^2\overline{D} + 3\alpha^2 F^2 D - 2\beta^2 D}{|D|^2}\right] \\
&= \frac{|C|^2}{2}\frac{|\left(3\alpha^2F^2 - 2\beta^2\right)\left(D + \overline{D}\right)}{|D|^2} \qquad \text{(H.7)}
\end{aligned}$$

These four terms combined can be used to determine $U_{2,00}$ as given by equation (3.14):

$$\begin{aligned}
U_{2,00} &= -\frac{\langle \mathcal{A}_x + \mathcal{R}_x\rangle}{2\mu_0} \\
&= -\frac{1}{2\mu_0}\left\langle v_1\frac{\partial u_1}{\partial y} + \mu 0\left(u_1 - F^2\zeta_1\right)^2 + \frac{1}{2}\mu_0 v_1^2 + \mu_1\left(2u_1 - F^2\zeta_1\right)\right\rangle
\end{aligned}$$

Substitution of equations (H.4), (H.5), (H.6) and (H.7) leads to the following general formulation of the second order spatially invariant contribution to the downstream flow as caused by the roughness patch:

$$\begin{aligned}
U_{2,00} = -\frac{|C|^2}{4\mu_0|D|^2}[\ &\overbrace{\alpha^2\beta^2F^2\left(X_1 + \overline{X_1}\right)}^{v_1\frac{\partial u_1}{\partial y}} + \overbrace{2\mu_0\left(4\alpha^2F^4|X_1|^2 - 3\alpha^2\beta^2F^2 + \beta^4\right)}^{\mu_0(u_1 - F^2\zeta_1)^2}\ldots \\
&+ \underbrace{\mu_0\alpha^2\beta^2}_{\frac{1}{2}\mu_0 v_1^2} + \underbrace{\left(3\alpha^2F^2 - 2\beta^2\right)\left(D + \overline{D}\right)}_{\mu_1(2u_1 - F^2\zeta_1)}\ ]
\end{aligned}$$

Appendix I

Restrictive minimum value tables

This appendix contains the tables that show the feasibility of combining certain roughness types in model calculations. Both the minimum values for L^* and H^* are shown for the each combination of vegetation for feasible and useful combinations. Three colors are used to mark the usefulness. Green represents that a combination is useful ($0 \leq H^* \leq 5$ and $0 \leq L^* \leq 250$), yellow shows that the usefulness is marginal as patch lengths and water depths are already too high for the analysis of roughness patches on a small scales while the values are still realistic ($5 < H^* \leq 10$ and $250 < L^* \leq 500$) and red marks all values out of these two ranges, which thus carry no significance for the analysis. The patches used in this model consist of only one mode and are thus determined using equation (4.3). When patches become more complex, different limits apply, which have been automatically built into the model.

E = 0.05	Back-ground	Sand		Ditch		Field		Pioneer Vegeta-tion		Natural grass-lands		Wet brush-wood		Sedge Marsch		Dry brush-wood		Dewberry brush-wood		Reed grass		Reed brush-wood		Reed		Softwood Alluvial Forest	
	k	0.10		0.15		0.20		0.28		0.39		0.47		0.73		1.45		1.58		2.23		11.4		12.4		12.9	
Patch	k	H	L	H	L	H	L	H	L	H	L	H	L	H	L	H	L	H	L	H	L	H	L	H	L	H	L
Sand	0.10	0	0																								
Nevengeul	0.15	34	####	0	0																						
Field	0.20			4.5	931	0	0																				
Pioneer Vegetation	0.28					16	####	0	0																		
Natural grasslands	0.39							21	####	0	0																
Wet brushwood	0.47									1.5	128	0	0														
Sedge Marsch	0.73											324	####	0.1	0												
Dry brushwood	1.45															0.1	####										
Dewberry brushwood	1.58															0.7	13	0.1	####								
Reed grass	2.23															817	####	153	####	0.2	0						
Reed brushwood	11.4																					1	####				
Reed	12.4																					5.3	93	1	####		
Softwood Alluvial Forest	12.9																					12	454	2.3	9	1.1	####

Figure I.1: *This table shows for what combinations of roughness types the model is applicable while also showing the minimum required values for L^* and H^* at $\epsilon_{max} = 0.05$*

E = 0.10	Back-ground	Sand		Ditch		Field		Pioneer Vegeta-tion		Natural grass-lands		Wet brush-wood		Sedge Marsch		Dry brush-wood		Dewberry brush-wood		Reed grass		Reed brush-wood		Reed		Softwood Alluvial Forest	
	k	0.10		0.15		0.20		0.28		0.39		0.47		0.73		1.45		1.58		2.23		11.4		12.4		12.9	
Patch	k	H	L	H	L	H	L	H	L	H	L	H	L	H	L	H	L	H	L	H	L	H	L	H	L	H	L
Sand	0.10	0	0																								
Nevengeul	0.15	0.6	59	0	0																						
Field	0.20	12	####	0.3	13	0	0																				
Pioneer Vegetation	0.28	403	####	8.6	####	0.6	39	0	0																		
Natural grasslands	0.39			278	####	18	####	0.8	51	0	0																
Wet brushwood	0.47					128	####	5.3	870	0.2	4.9	0	0														
Sedge Marsch	0.73							534	####	23	####	3.9	469	0.1	0												
Dry brushwood	1.45													81	####	0.1	####										
Dewberry brushwood	1.58													198	####	0.3	1.4	0.1	####								
Reed grass	2.23															11	####	4.9	355	0.2	0						
Reed brushwood	11.4																					1	####				
Reed	12.4																					2.3	10	1	####		
Softwood Alluvial Forest	12.9																					3.5	33	1.6	1.5	1.1	####

Figure I.2: *This table shows for what combinations of roughness types the model is applicable while also showing the minimum required values for L^* and H^* at $\epsilon_{max} = 0.10$*

E = 0.15	Back-ground	Sand		Ditch		Field		Pioneer Vegeta-tion		Natural grass-lands		Wet brush-wood		Sedge Marsch		Dry brush-wood		Dewberry brush-wood		Reed grass		Reed brush-wood		Reed		Softwood Alluvial Forest	
	k	0.10		0.15		0.20		0.28		0.39		0.47		0.73		1.45		1.58		2.23		11.4		12.4		12.9	
Patch	k	H	L	H	L	H	L	H	L	H	L	H	L	H	L	H	L	H	L	H	L	H	L	H	L	H	L
Sand	0.10	0	0																								
Nevengeul	0.15	0.2	6.6	0	0																						
Field	0.20	1.2	149	0.1	2.2	0	0																				
Pioneer Vegetation	0.28	13	####	1.1	111	0.2	5.6	0	0																		
Natural grasslands	0.39	136	####	11	####	1.9	232	0.2	7.4	0	0																
Wet brushwood	0.47	515	####	43	####	7.4	####	0.9	67	0.1	1.2	0	0														
Sedge Marsch	0.73			991	####	170	####	22	####	2.8	298	0.9	47	0.1	0												
Dry brushwood	1.45									378	####	120	####	8.1	####	0.1	####										
Dewberry brushwood	1.58									697	####	222	####	15	####	0.2	0.4	0.1	####								
Reed grass	2.23													174	####	2.6	130	1.5	49	0.2	0						
Reed brushwood	11.4																					1	####				
Reed	12.4																					1.7	3.3	1	####		
Softwood Alluvial Forest	12.9																					2.3	9.5	1.4	0.6	1.1	####

Figure I.3: *This table shows for what combinations of roughness types the model is applicable while also showing the minimum required values for L^* and H^* at $\epsilon_{max} = 0.15$*

E = 0.20	Back-ground	Sand		Ditch		Field		Pioneer Vegeta-tion		Natural grass-lands		Wet brush-wood		Sedge Marsch		Dry brush-wood		Dewberry brush-wood		Reed grass		Reed brush-wood		Reed		Softwood Alluvial Forest	
	k	0.10		0.15		0.20		0.28		0.39		0.47		0.73		1.45		1.58		2.23		11.4		12.4		12.9	
Patch	k	H	L	H	L	H	L	H	L	H	L	H	L	H	L	H	L	H	L	H	L	H	L	H	L	H	L
Sand	0.10	0	0																								
Nevengeul	0.15	0.1	1.9	0	0																						
Field	0.20	0.4	26	0.1	0.7	0	0																				
Pioneer Vegetation	0.28	2.3	350	0.4	22	0.1	1.8	0	0																		
Natural grasslands	0.39	14	####	2.3	303	0.6	42	0.1	2.3	0	0																
Wet brushwood	0.47	38	####	6.3	####	1.8	187	0.4	16	0.1	0.5	0	0														
Sedge Marsch	0.73	422	####	69	####	19	####	4.3	578	1	58	0.4	12	0.1	0												
Dry brushwood	1.45					813	####	182	####	42	####	18	####	2.6	178	0.1	####										
Dewberry brushwood	1.58							291	####	67	####	29	####	4.1	358	0.2	0.2	0.1	####								
Reed grass	2.23									435	####	190	####	27	####	1.3	35	0.9	15	0.2	0						
Reed brushwood	11.4																					1	####				
Reed	12.4																					1.5	1.6	1	####		
Softwood Alluvial Forest	12.9																					1.9	4.3	1.3	0.3	1.1	####

Figure I.4: *This table shows for what combinations of roughness types the model is applicable while also showing the minimum required values for L^* and H^* at $\epsilon_{max} = 0.20$*